DOE/ER/14596--T1

Sedimentological and Geophysical Studies of Clastic Reservoir Analogs: Methods, Applications and Developments of Ground-Penetrating Radar for Determination of Reservoir Geometries in Near-Surface Settings

Final Report

Work Performed Under Contract No. DE-FG03-96ER14596

Prepared for

U.S. Department of Energy

George A. McMechan, Principal Investigator
Phone: (972) 883-2424
Fax: (972) 883-2829
e-mail: mcmec@utdallas.edu

Kristian Soegaard, Co. PI
Phone: (972) 883-2415
Fax: (972) 883-2537
e-mail: soegaard@utdallas.edu

The University of Texas at Dallas
P.O. Box 830688 (FA31)
Richardson, TX 75083-0688

May 25, 1998

DISCLAIMER

Sedimentological and Geophysical Studies of Clastic Reservoir Analogs: Methods, Applications and Developments of Ground-Penetrating Radar for Determination of Reservoir Geometries in Near-Surface Settings

EXECUTIVE SUMMARY

An integrated sedimentologic and GPR investigation has been carried out on a fluvial channel sandstone in the mid-Cretaceous Ferron Sandstone at Coyote Basin along the southwestern flank of the San Rafael Uplift in east-central Utah. This near-surface study, which covers a area of 40 x 16.5 meters to a depth of 15 meters, integrates detailed stratigraphic data from outcrop sections and facies maps with multi-frequency 3-D GPR surveys. The objectives of this investigation are two-fold, (1) to develop new ground-penetrating radar (GPR) technology for imaging shallow subsurface sandstone bodies, and (2) to construct an empirical three-dimensional sandstone reservoir model suitable for hydrocarbon flow-simulation by imaging near-surface sandstone reservoir analogs with the use of GPR.

The sedimentological data base consists of a geologic map of the survey area and a detailed facies map of the cliff face immediately adjacent to the survey area. Five vertical sections were measured along the cliff face adjacent to the survey area. In addition, four wells were cored within the survey area from which logs were recorded. In the sections and well logs primary sedimentary structures were documented along with textural information and permeability data. Gamma-ray profiles were also obtained for all sections and core logs. The sedimentologic and stratigraphic information serves as the basis from which much of the processing and interpretation of the GPR data was made.

Three 3-D GPR data sets were collected over the survey area at frequencies of 50 MHz, 100 MHz, and 200 MHz. The 3-D surveys each consisted of 34 lines with 80 traces with a line spacing of 0.5m, yielding a total of 2720 traces for each data volume. Down-hole GPR and cross-hole tomography were performed within three of the four wells drilled in the survey for the purpose of modeling electrical properties of the fluvial sandstone under investigation. In addition, three 2-D GPR lines were acquired between the three wells in which the down-hole and cross-hole GPR were performed.

Laboratory measurements were performed on 33 coreplugs from the four wells and provided a direct measure of electrical properties at the selected sites. Electrical properties in conjunction with permeability, porosity, compositional data and clay content of the 33 coreplug samples were used for constraining electrical wave velocity and attenuation within the survey cube.

Processing of GPR data was carried out on each of the 3-D data sets and included, 1) initial data preparation, 2) preliminary processing, 3) 3-D depth migration, and 4) display. The depth migration, which was based on velocities from borehole GPR and electrical measurements, allowed the reflection GPR data to be compared directly with the geological information collected at the outcrop.

The three 3-D GPR data sets were loaded onto a GeoQuest workstation at ARCO Oil and Gas Company for interpretation. Simplified geologic models of the core logs were constructed from sand/clay content, permeability and GPR velocity. Synthetic radargrams were generated for these models to assure correct ties between GPR reflectors and corresponding geologic features.

A hierarchy of bounding surfaces are recognized within the fluvial sandstone at Coyote Basin. The highest order bounding surfaces define major architectural elements within the sandstone complex and are identified as surface A, B, C, D, and E. These bounding surfaces are outlined by discontinuous mudstones which constitute the principal flow barriers within the fluvial reservoir analog. All five surfaces are clearly identified within the 100 MHz data set and mapped throughout the survey volume. Smaller-scale, lower-order sedimentary features such as trough cross beds, mudstone intraclast conglomerates and mudstone layers are also mapped in 3-D within parts of the survey volume using both the 100 MHz and 200 MHz datasets.

An auxillary project was to develop the permeability structure and to perform flow simulation on the survey volume at Coyote Basin. This auxillary project was funded by a consortium of petroleum companies, including ARCO, Mobil, Union Pacific and Unocal and represents part of the technology transfer of the integrated GPR and sedimentology-stratigraphy study at Coyote Basin. In addition to presentations and reports submitted to consortium members technology transfer has included presentations at two nanional meetings (AAPG) and publication of one paper. Finally, four manuscripts are in the final stages of preparation and represent additional technology transfer.

TABLE OF CONTENTS

ACKNOWLEDGMENTS

Craig Forster and Steve Snelgrove at the University of Utah are acknowledged for obtaining drilling permits at Coyote Basin and assisting in laying out the strategy for collecting data in the field. Steve Snelgrove, Ari Menitove and Craig Forster managed the drilling project as well as extracting coreplugs from the cliff face. All permeability data were obtained in the lab at the University of Utah under the direction of Craig Forster.

The consortium of petroleum companies including ARCO, Mobil, Union Pacific and Unocal are thanked for sponsoring the permeability study and for payment of electrical lab measurements performed at Georgia Tech University in Atlanta, Georgia. The consortium also contributed toward funding of the petrographic study carried out by Karen Roche under the direction of Laura Crossey at The University of New Mexico at Albuquerque.

The University of Texas at Dallas GPR Consortium is acknowledged for direct funding of drilling and coring costs of the four wells at the Coyote Basin site.

Finally, a special thanks is extended to Gerard (Neil) Gaynor who initially proposed the idea of using GPR for reservoir charaterization in the Ferron Sandstone. He proposed the project back in 1991 and persued the feasibility of the idea through several pilot projects.

LIST OF TABLES

LIST OF FIGURES

INTRODUCTION

Kristian Soegaard and George McMechan

A geostatistically and geometrically realistic description of clastic reservoir flow units and permeability barriers within reservoir units is vital to planning of field exploitation and improved hydrocarbon recoveries. Accurate reservoir models, based on outcrop data, are being used to better predict reservoir geometries and distributions of reservoir properties for use in simulation and locating production and injection wells (Flint and Bryant, 1993). However, these models are generally two-dimensional and generalization to the third dimension is necessary. For example, Henriquez et al. (1990) demonstrate the interconnectedness and orientation of fluvial channels in simulation design in this type of reservoir system. At present these factors can only be estimated from stochastic models (Damsleth and Holden, 1994) or through process-oriented stratigraphic models (Mackey and Bridge, 1995). New technologies and techniques for three-dimensional reservoir characterization are necessary to improve the methodology.

An exciting new technology for characterizing reservoir heterogeneity is now emerging through the use of ground-penetrating radar (GPR) to create the first true empirical 3-D analogs of reservoir heterogeneity (Baker, 1991; Gawthorpe et al., 1993). Unlike high frequency seismic data which typically has vertical and horizontal resolution of >5m and >25m, respectively, which is not sufficient for characterizing hydrocarbon reservoirs, GPR data are able to resolve features at a decimeter scale (Fig. 1). Until the present study, almost all GPR surveys have been performed on unconsolidated, recent sediment rather than on consolidated sedimentary sequences in which hydrocarbon accumulations occur (e.g. Bridge et al., 1995). Moreover, GPR studies are usually two dimensional (Alexander et al., 1994), or consist of pseudo 3-D studies consisting of widely spaced intersecting 2-D lines (e.g. Bristow, 1995). Notable exceptions are 3-D GPR surveys on recent delta gravels in Switzerland (Beres et al., 1995) and Cretaceous shoreface sandstone bodies (McMechan et al., 1997) and fluvial channels (Thurmond et al., 1997) in Utah.

Most GPR studies for high resolution subsurface analysis of unconsolidated sediment include interpretation of the data in their raw state, without processing. However, the kinematic aspects of GPR data may be treated similar to those of seismic reflection data (Fisher et al., 1992a and b). This implies that many of the processing techniques developed for contemporary seismic data, and interpretation facilities, may also be used in GPR investigations.

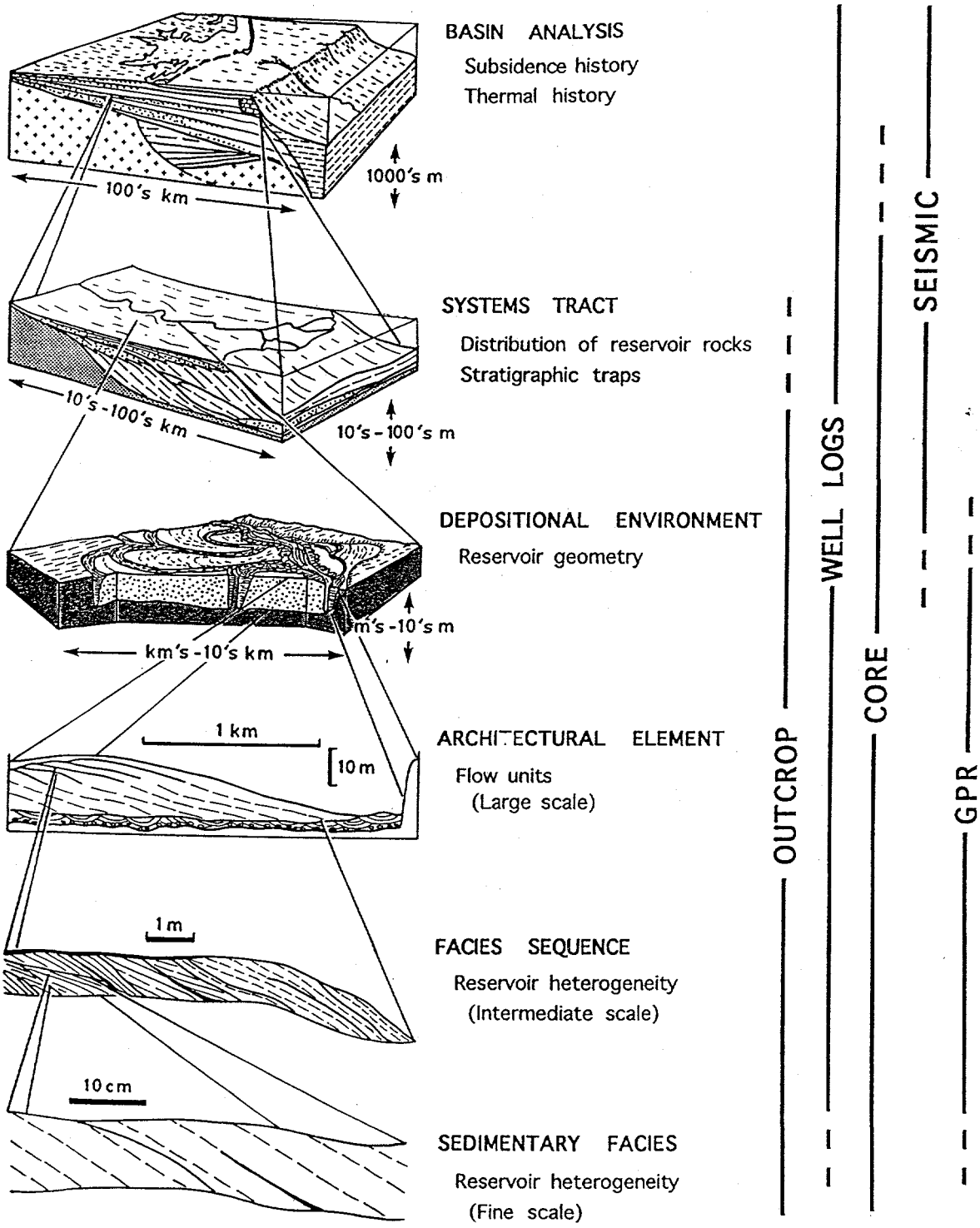

Figure 1: Hierarchy of scales of sedimentary features. Considerations for petropleum reservoirs are generally at the level of depositional environments and smaller scales. The range of scales of various geological and geophysical data are illustrated. Note that ground penetrating radar (GPR) is the only 3-D tool capable of imaging sedimentary rocks at the reservoir scale.

The objectives of this investigation are two-fold:

(1). To develop new ground-penetrating radar (GPR) technology for imaging shallow subsurface sandstone bodies, and

(2). To construct an empirical three-dimensional sandstone reservoir model suitable for hydrocarbon flow-simulation by imaging near-surface sandstone reservoir analogs with the use of GPR.

To meet these objectives, a survey site in fluvial-deltaic deposits of the Cretaceous Ferron Sandstone in east-central Utah was selected for investigation. The scale and depositional setting of the Ferron Sandstone is considered to be an analog for many oil fields and consequently, exposures of the Ferron Sandstone have been the focus of intensive analysis by petroleum reservoir geologists and engineers. The Ferron Sandstone is also chosen because of the excellent stratigraphic control, outstanding exposure along flat topped mesas (which are ideal for performing GPR surveys) and the large data base from reservoir studies carried out in the past that may complement the present study. Potential reservoir rocks in the Ferron Sandstone are generally subdivided on the basis of depositional setting and relative position of the shoreline.

The project was divided into five tasks:

(1). Collection of detailed sedimentary and stratigraphic data in the survey area, including a surface geology map, facies maps constructed from photo-mosaics of cliff faces along mesas in the Ferron Sandstone, measured sections, core data from wells drilled in the survey area, and gamma-ray data collected at the outcrop.

(2). Acquisition of GPR data within the survey area on the mesa top immediately adjacent to the cliff face where photo-mosaic facies maps were constructed. The GPR data include three 3-D surveys collected at frequencies of 50, 100 and 200 MHz in addition to several 2-D lines collected at 100 and 200 MHz. Down-hole GPR data were obtained within the wells for the purpose of developing a velocity model for depth-migration of the 3-D GPR data and for conducting cross-hole tomography.

(3). 3-D GPR data were processed, depth migrated and numerically synthesized.

(4). Interpretation of the 3-D GPR data was performed on a GeoQuest workstation. Ties were made between synthetic GPR traces computed from stratigraphic logs in the wells, and

GPR measurements. Interpretation of the GPR data was related directly to the sedimentological and stratigraphic data.

(5). Obtaining permeability data from coreplugs extracted from the outcrop and from cores. Data from the four wells were used for defining flow units within the survey cube. Empirical relationships between sediment composition, clay content, grain size, porosity, permeability, water saturation, and dielectric permittivity were established for the purpose of providing a data base for interpretation of the GPR data in terms of the petrographic, sedimentologic, and petrophysical variability.

This report is organized into five sections, including the Introduction, Regional Stratigraphy, Description of the Coyote Basin Site, GPR Acquisition and Processing, and Interpretation of GPR Data. Finally, an outline for Technology Transfer is presented.

REGIONAL STRATIGRAPHIC SETTING

Kristian Soegaard and George McMechan

The mid-Cretaceous Ferron Sandstone Member of the Mancos Shale consists of two fluvio-deltaic complexes. The lower part of the Ferron Sandstone is the middle to upper Turonian Vernal delta with a depocenter in northeastern Utah and progradation toward the east (Gardner, 1995). The upper Ferron Sandstone is informally referred to as the Last Chance delta which was situated in south-central Utah with progradation toward the northeast. Presently the lower Ferron Vernal delta complex is exposed in the northern San Rafael Swell in east-central Utah whereas the Last Chance Delta outcrops along a series of sandstone cliffs before dipping into the subsurface along the western flank of the San Rafael Swell (Fig. 2). The present study is carried out in the Last Chance Delta exclusively and will be referred to as the Ferron Sandstone throughout this report. This younger delta complex originally covered an area of more than 8,000 km^2.

Stratigraphic architecture and depositional characteristics of the Ferron Sandstone are outlined by Ryer (1981), Gardner (1995), Garrison et al. (1997) and Chidsey (1997). The Ferron Sandstone is subdivided into seven units by Ryer (1981) (or parasequence sets using terminology of Van Wagoner et al., 1988 and 1990), with units being referred to as SC1 through SC7 (Fig. 3). Similarly, Gardner (1995) subdivides the Ferron into 7 units termed SC1 through SC7, whereas Ryer et al. (in Chidsey, 1997) recognize a parasequence set below SC1 (their Kf-Last Chance unit) and tentatively one above SC7 (their Kf-8?). The entire upper Ferron Sandstone has been interpreted as progradational (SC1, SC2, SC3), in which sea level

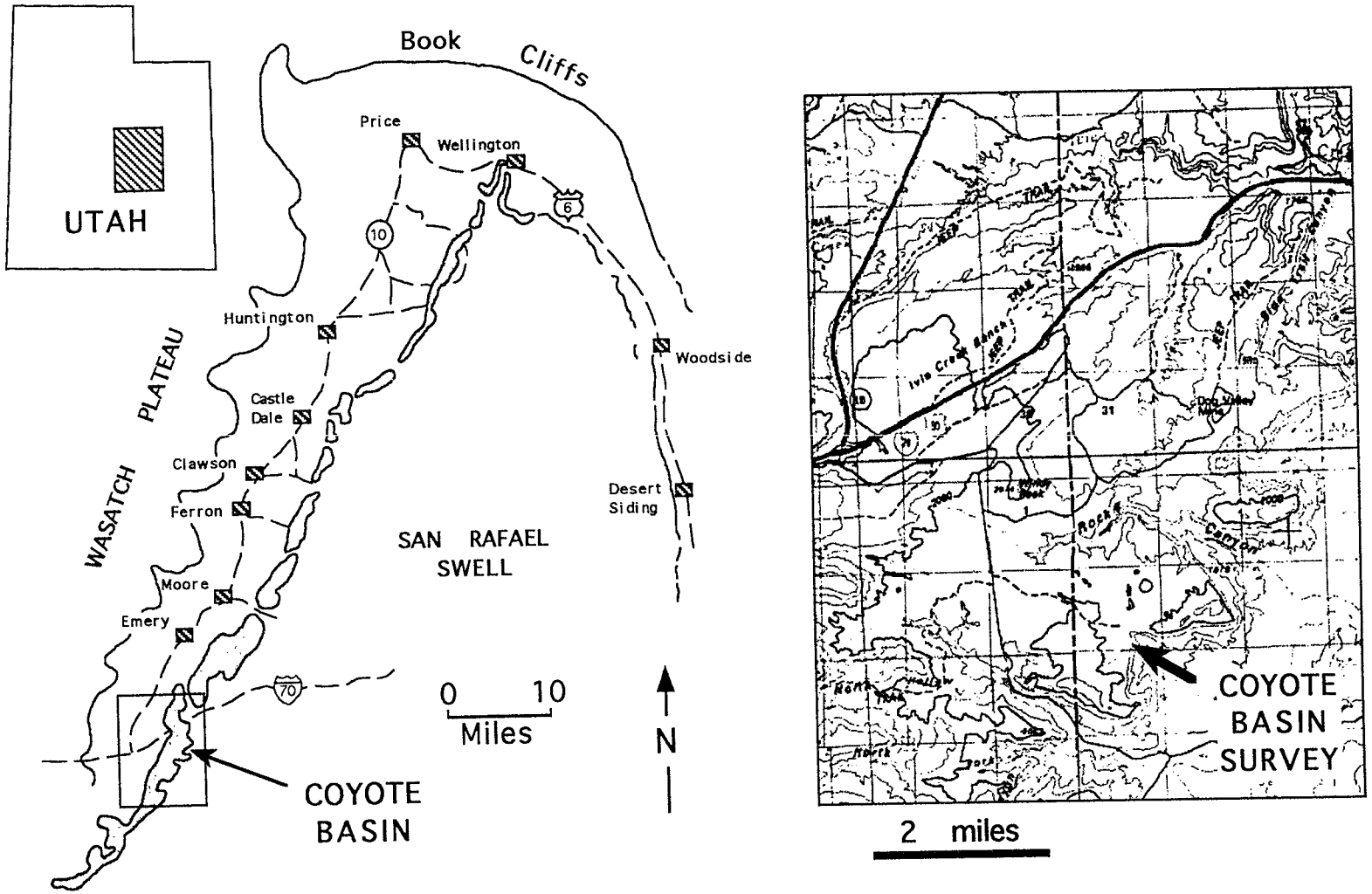

Figure 2: Location map of Coyote Basin GPR survey site in Ferron Sandstone along the southwestern flank of the San Rafael Swell in east-central Utah. Location of topographic map inset is shown by box.

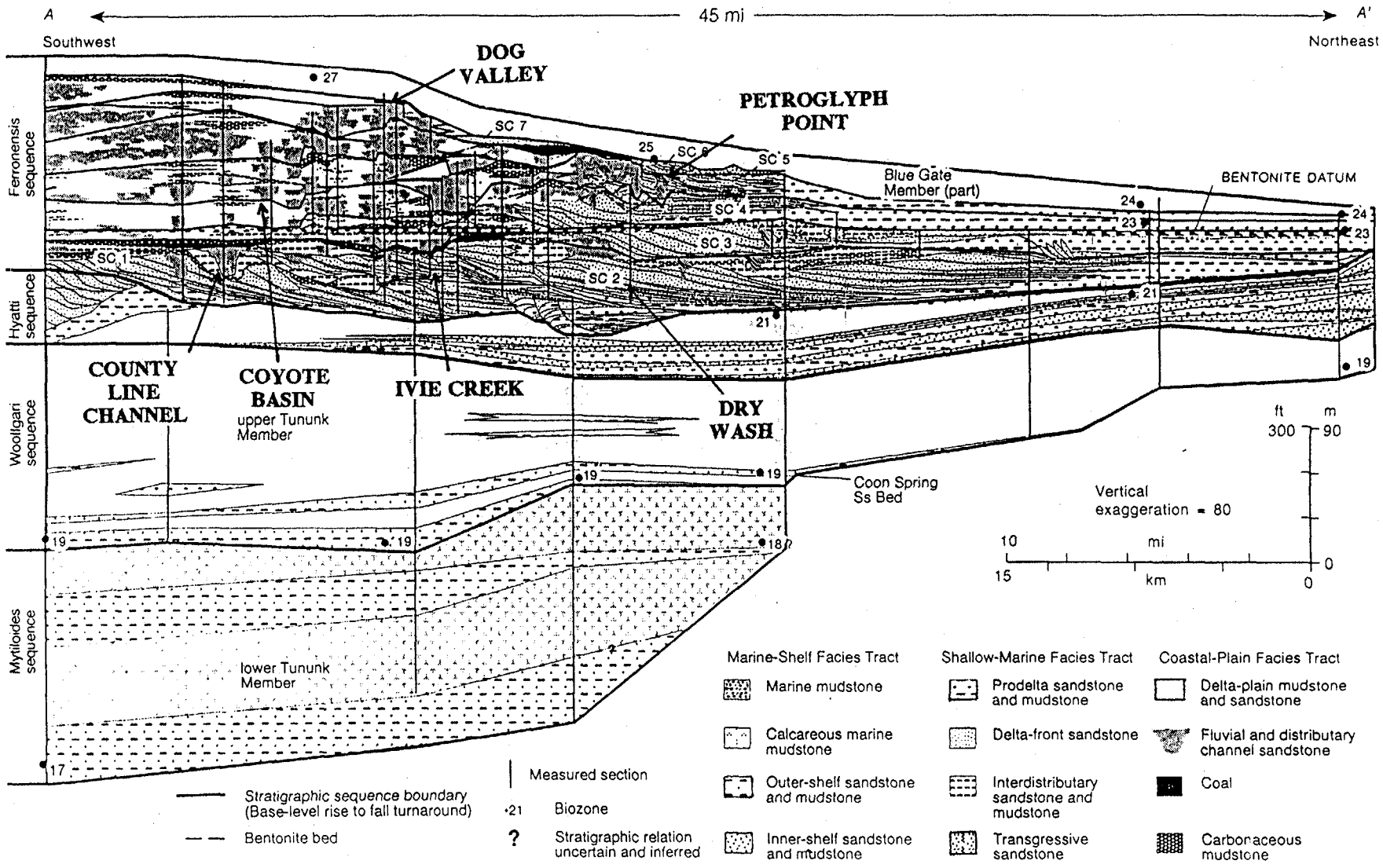

Figure 3: Geologic cross section of Ferron Sandstone along west flank of San Rafael Swell in east-central Utah (after Gardner, 1995). Location of Coyote Basin and proposed Dog Valley GPR site for the continuation project are illustrated. The Coyote Basin site is located in the fluvial portion of Ferron Sandstone at top of SC3 whereas the proposed new site is in parasequence set SC7. Also shown are reservoir characterization sites in marine sandstone at Petroglyph Point in SC6 (UT Dallas GPR investigation; McMechan et al., 1997) and at Ivie Creek in SC2 (Craig Forster, University of Utah; reservoir and flow simulation study).

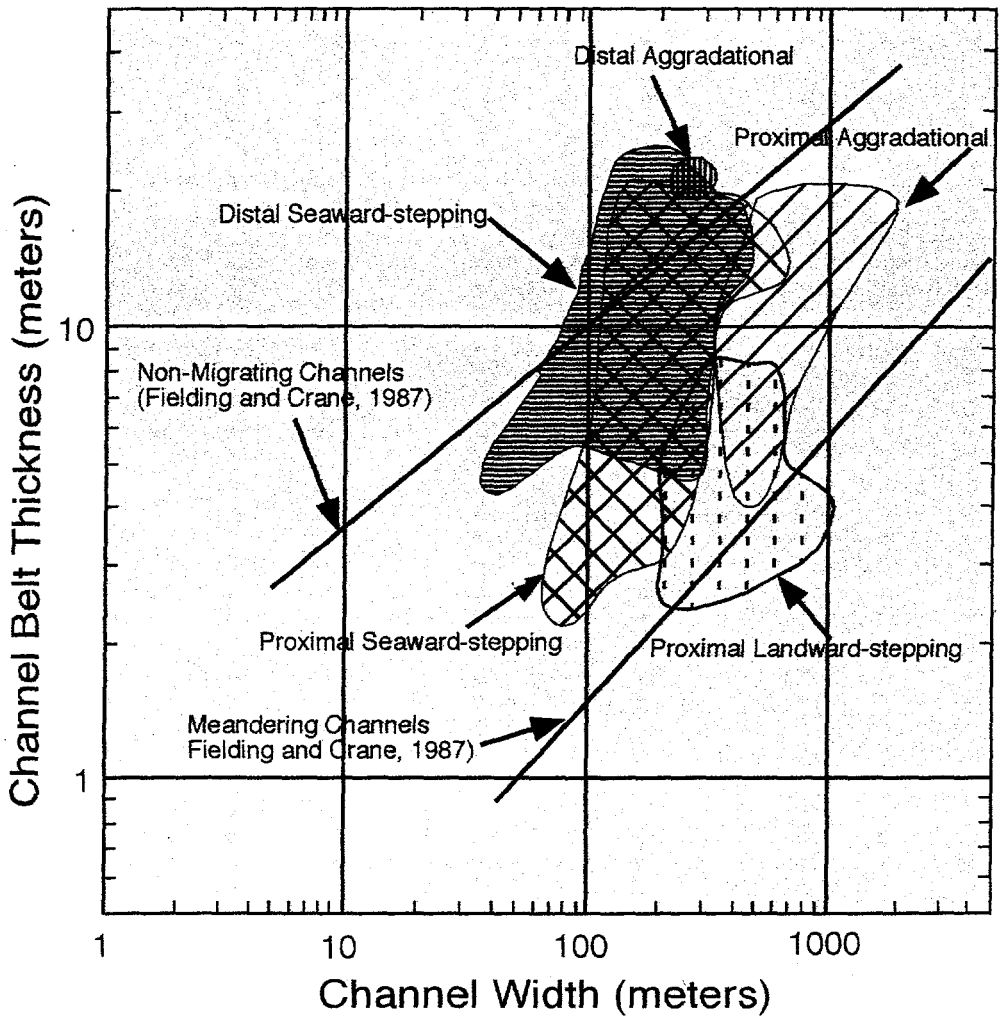

Figure 4: Plot of thickness versus width for the channel belts within the Ferron seaward-stepping, aggradational, and landward-stepping parasequence sets. Trend lines for channel thickness versus width distributions from Fielding and Crane (1987) are shown for comparison (after van den Bergh and Garrison, 1996).

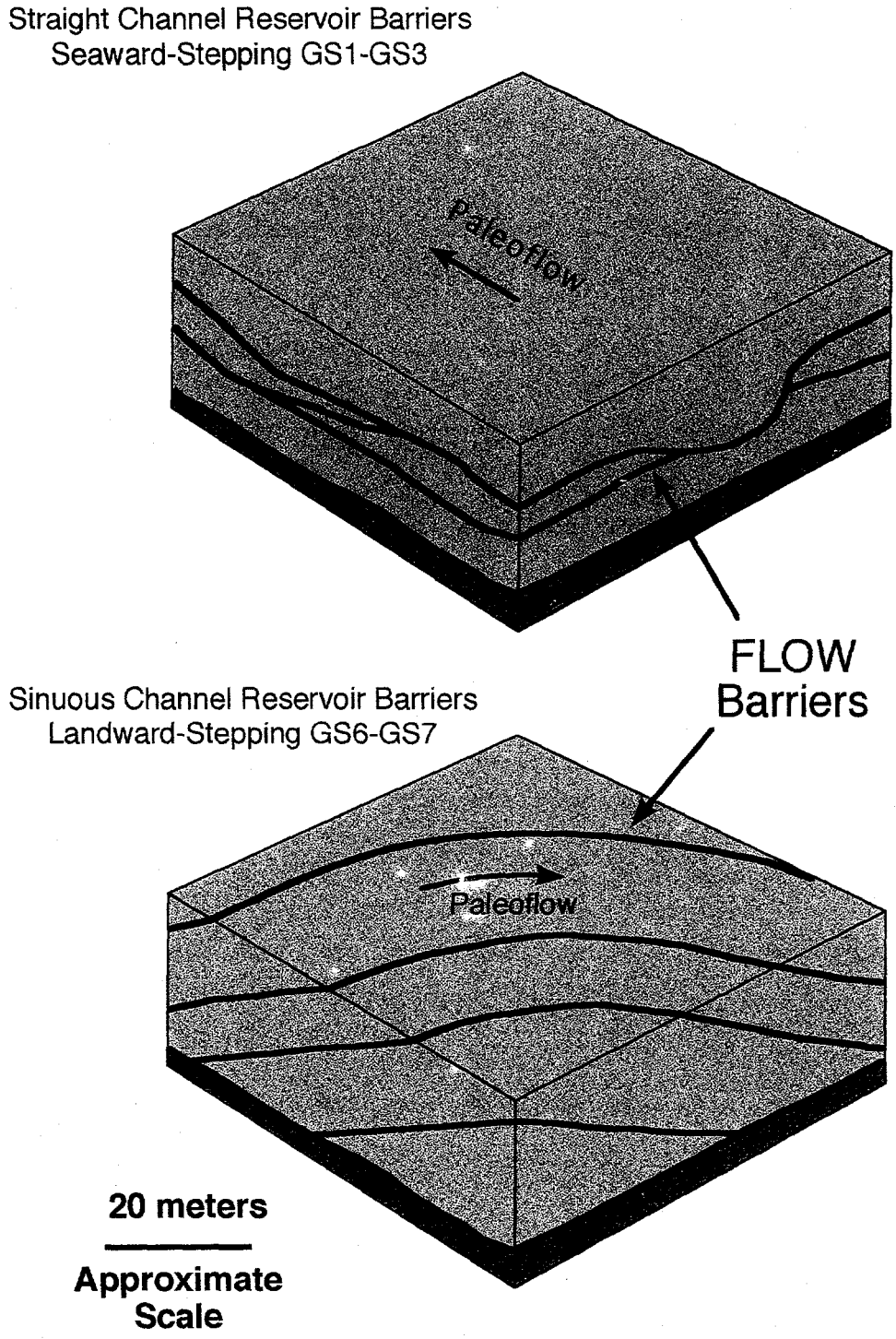

Figure 5: Schematic diagrams illustrating difference in distribution of barriers and baffles between straight fluvial channel at Coyote Basin and proposed site of meandering fluvial channel at Corbula Gulch.

SITE DESCRIPTION

Kristian Soegaard, George McMechan and John B. Thurmond

In the summer of 1996, field work was carried out in the Ferron Sandstone at Coyote Basin (Fig. 2). The site is located at the top of the upper Turonian SC3 unit of the Ferron Sandstone (according to terminology of Gardner, 1995; Fig. 3). In the context of local coal stratigraphy outlined by Garrison et al. (1997), the sandstone at the Coyote Basin survey site is situated immediately below the C4 coal horizon. Apart from SC1, units SC2 through SC7 of the Ferron Sandstone in this southwestern part of the San Rafael Swell are composed exclusively of alluvial deposits (Fig. 3).

The upper ~12 meters of the site consist of a fluvial sandstone complex which scours into underlying floodplain mudstone and coal. This sandstone forms a resistant caprock which defines a mesa top upon which the GPR survey was performed. The regional dip in the area is 3° to the northwest. Approximately 80% of the survey surface area consists of exposed sandstone outcrop with a thin veneer of sandy soil covering the remainder of the site (Fig. 6). A conjugate set of vertical fractures cross cuts the survey area, with the dominant set extending east-northeast and a subordinate set oriented south-southeast. Along the eastern margin of the GPR survey is a vertical cliff face which affords a cross sectional view of the channel sandstone body (Figs. 6 and 7).

A wide spectrum of surface and subsurface sedimentologic and stratigraphic data have been acquired at Coyote Basin. These data include: (1) A surface geology map of the GPR survey site in which features such as cross beds, fractures and soil cover are illustrated (Fig. 6); (2) Photomosaics and a facies map of the vertical cliff face immediately adjacent to the GPR data cube, which reveals the geometry of various hierarchies of sedimentologic and stratigraphic elements (Fig. 7); (3) Five stratigraphic sections along the 40 meter cliff face covered by the facies map, providing additional sedimentologic information, such as textural variation and permeability distribution within the survey area (Fig. 8; Appendix A); (4) Gamma-ray data obtained at 25 cm intervals along the stratigraphic sections (Fig. 8); (5) Four 15 meter-long 2 1/2-inch cores obtained from wells drilled in the survey area (Fig. 6) from which core logs were obtained (Appendix A); (6) Paleocurrent orientations from 81 trough cross beds within the GPR survey site and flow direction of an additional 130 trough cross beds adjacent to the survey area yielding information about depositional trends in the Ferron Sandstone at the stratigraphic level of the GPR survey (Fig. 9). (7) 485 core plugs were extracted from the cliff face at 10 cm intervals along the stratigraphic sections and an additional 200 core plugs were retrieved from other parts of the facies map for the purpose of obtaining petrophysical properties in the lab.

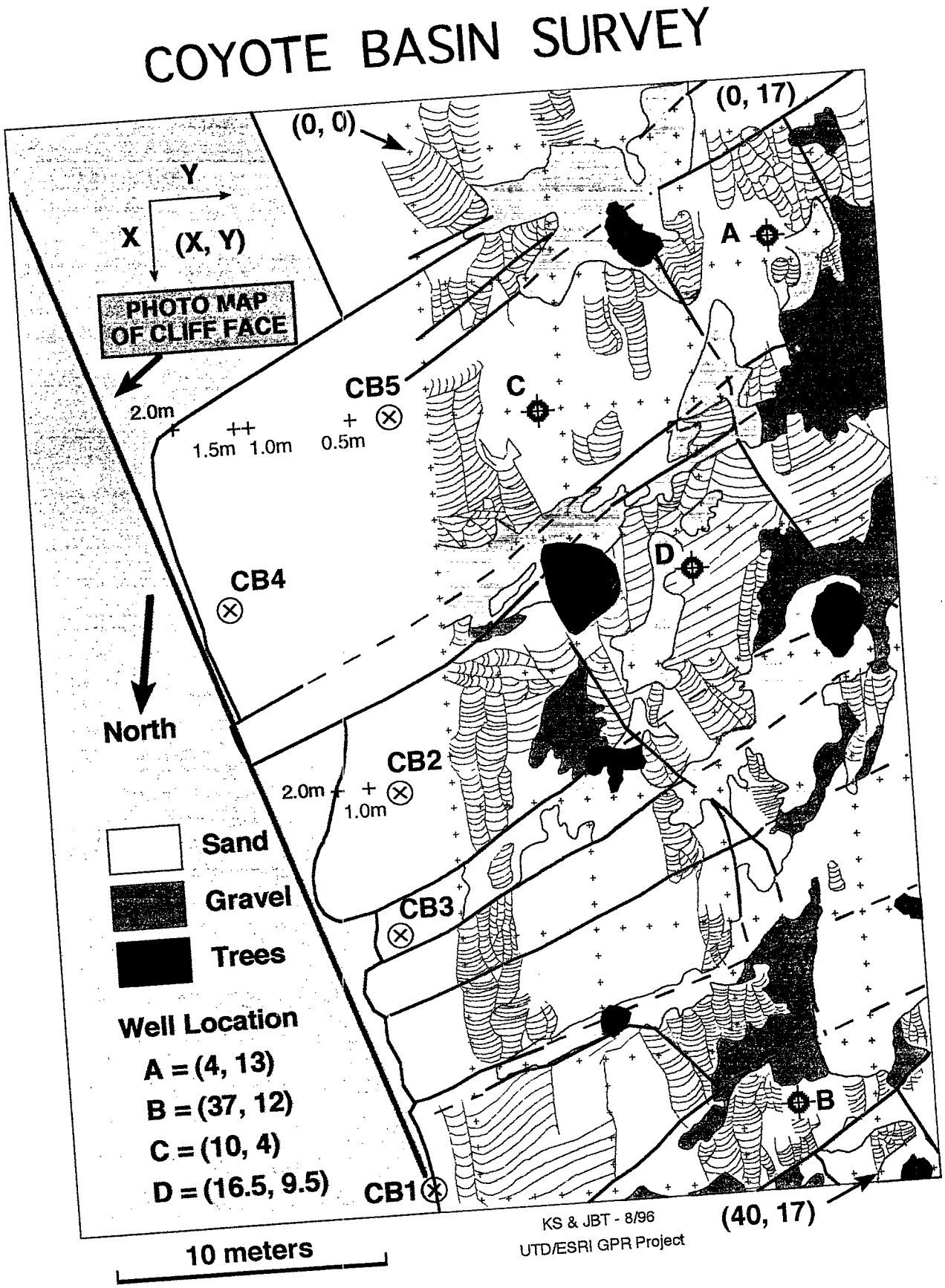

Figure 6: Surface geology map of GPR survey site at Coyote Basin. The surface geology consists exclusively of trough cross beds indicating paleoflow toward the southeast. CB1 through CB5 represent locatio of measured stratigraphic sections and "A" through "D" are borehole locations from which cores we extracted. All data collected at the site follow the X-Y Cartesian coordinate system with unit of measure being meters.

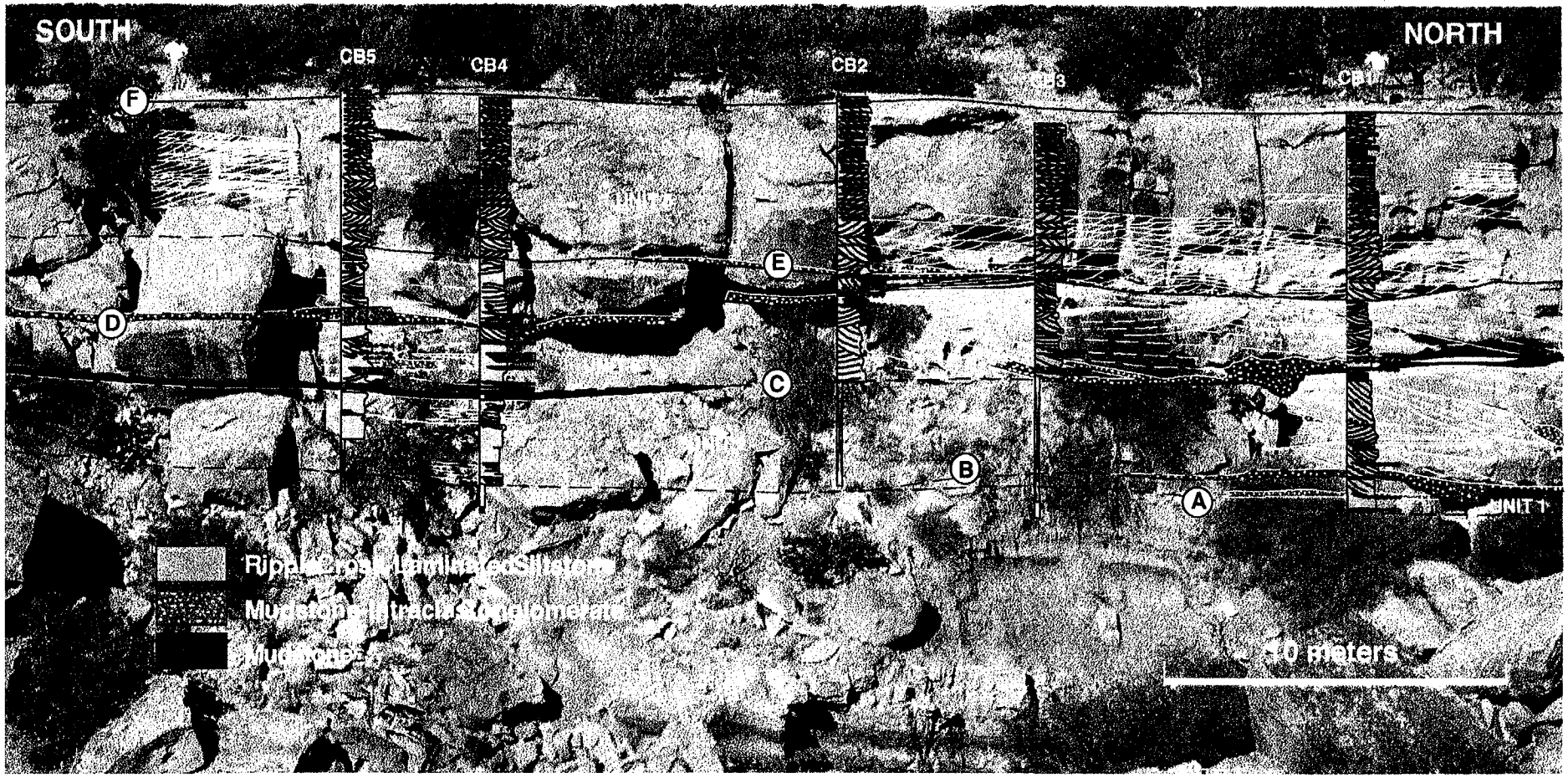

Figure 7a: Sedimentary facies map of the cliff face at Coyote Basin. Higher-order bounding surfaces (A through E), shown in red, outline major architectural elements termed Unit 1 through 5. Less-significant, lower-order bounding surfaces are illustrated in white. Exposed surfaces shown as solid lines; dashed lines are inferred where outcrop is covered. Also shown are five stratigraphic sections or "pseudo wells" in which primary sedimentary structures, textural information, permeability, and gamma-ray data are measured (Figure 7b and Appendix A).

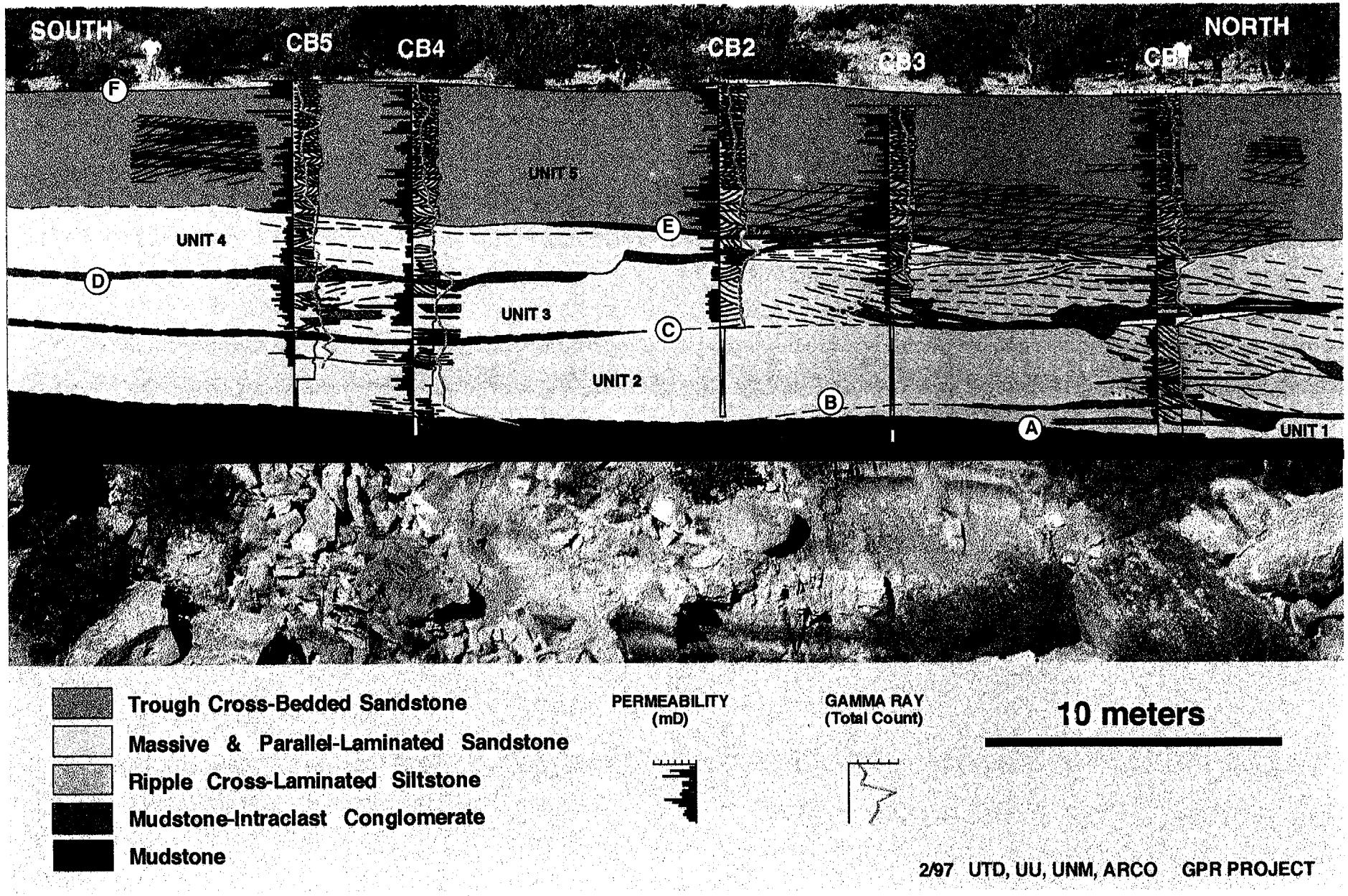

Figure 7b: Sedimentary facies map of the cliff face at Coyote Basin. Higher-order bounding surfaces (A through E), shown in red, outline major architectural elements termed Unit 1 through 5. Less-significant, lower-order bounding surfaces are illustrated in black. Exposed surfaces shown as solid lines; dashed lines are inferred where outcrop is covered. Also shown are five stratigraphic sections or "pseudo wells" in which primary sedimentary structures, textural information, permeability, and gamma-ray data are measured.

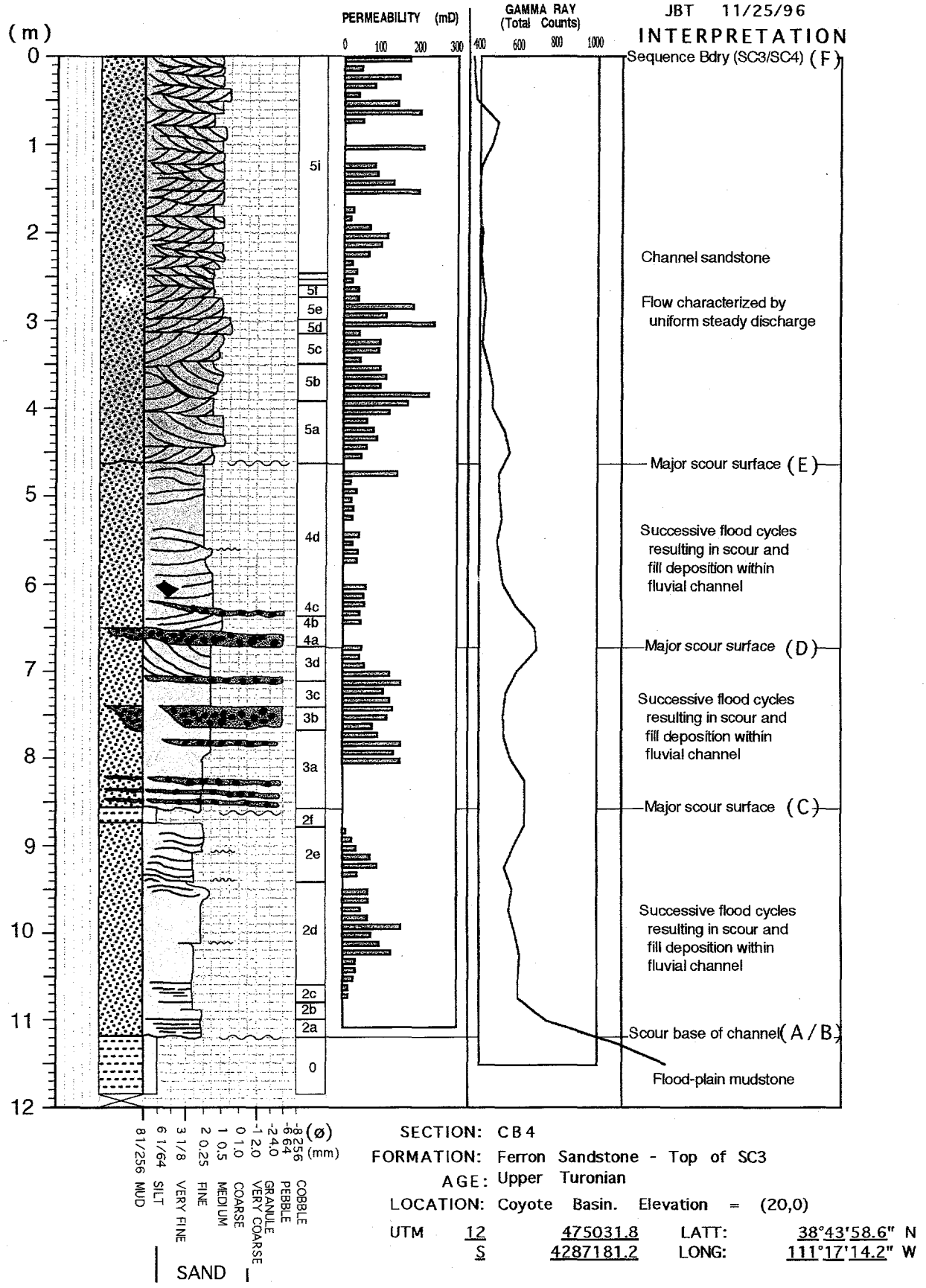

Figure 8: Example of a stratigraphic section measured at the cliff-face. The example is section CB4 in Figure 7. Location of significant bounding surfaces "A" through "F" are shown. Also illustrated are permeability values determined from coreplugs spaced at 10 cm intervals. Gamma-ray profile is obtained with hand-held scintillometer at 25 cm intervals through the section.

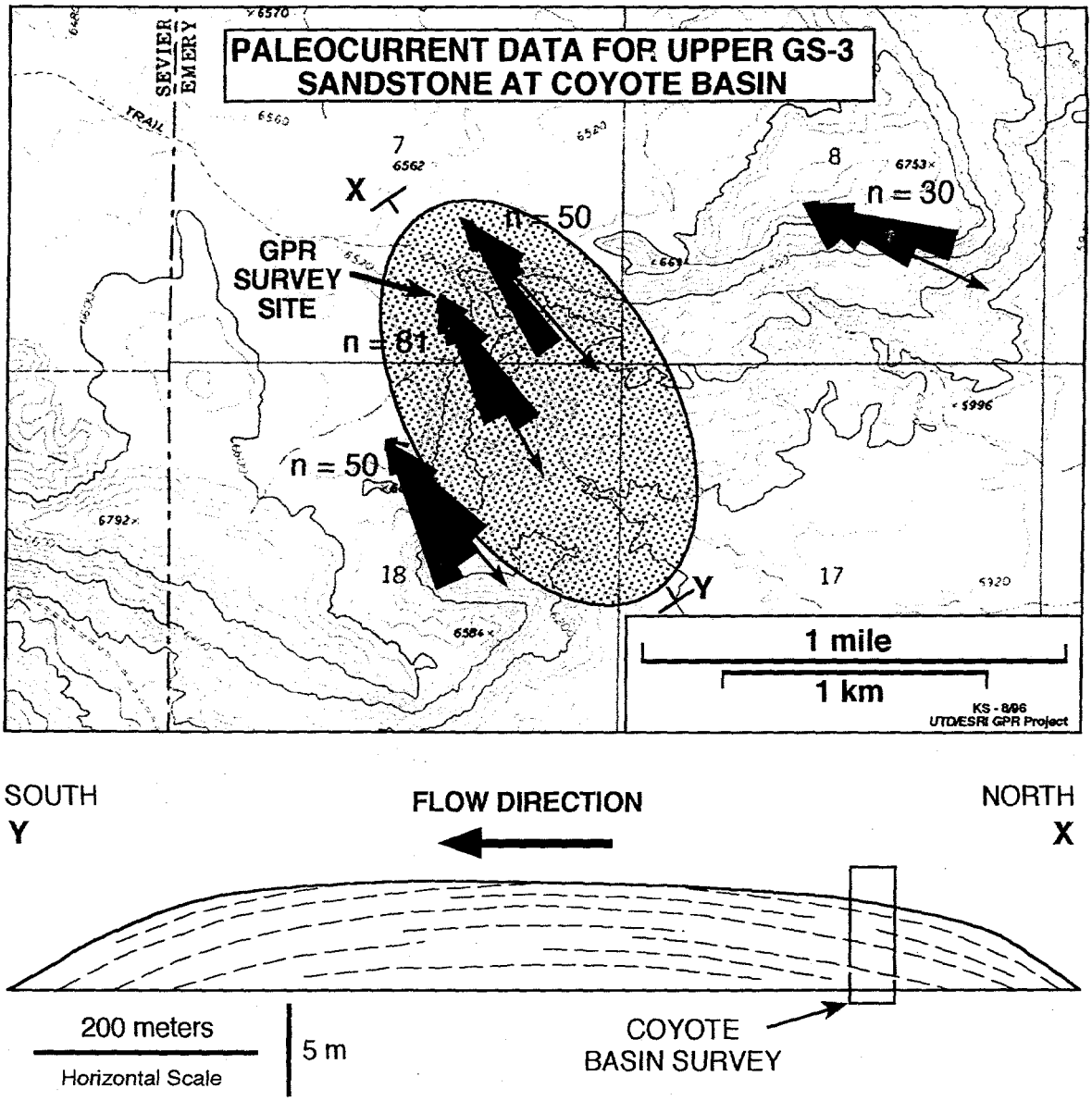

Figure 9: Paleocurrent map for upper surface of the fluvial sandstone under investigation. The paleocurrent rose diagrams are exclusively for the upper Unit 5 in the facies map (Fig. 7) and represent flow from medium-sized trough cross beds. The trough cross-bedded sandstone in unit 5 is interpreted as a channel barform in which the GPR site at Coyote Basin is located in an up-current direction. The approximate areal extent (stippled region in map) and the cross sectional geometry and internal reflectors (cross-bed cosets), illustrated below, are based on outcrop facies maps.

GPR DATA ACQUISITION AND PROCESSING

Robert B. Szerbiak, Deming Wang, George McMechan and John B. Thurmond

Data Acquisition

A rectangular 3-D GPR survey grid was laid out on top of the mesa to extend geologic control from the exposed cliff face westward into the interior of the reservoir analog (Fig. 6). Dimensions of the grid are 40m x 16.5m with a 0.5 m grid spacing. The data volume consists of 34 N-S in-lines each of 80 traces giving a total of 2720 traces for the data volume. The GPR equipment used was a PulseEKKO IV system with a transmitter voltage of 1000 V. Three 3-D data sets were recorded at frequencies of 50 MHz, 100 MHz and 200 MHz. These frequencies provided corresponding depth resolutions of about 1 m, 0.5 m and 0.25 m. Dipole antennas were oriented parallel to each other and perpendicular to the in-line direction, providing a polarization plane parallel with the ground surface. Maximum depths of usable data were approximately 25 m, 15 m and 8 m, respectively. Both high resolution sedimentary structures and lower-resolution, large-scale sedimentary architectural elements were recorded. A single common midpoint (CMP), covering an offset range of 26 m, was recorded for each data set. The CMP's provided initial velocity control and helped optimize the source-receiver offset. The offsets used for the 3-D common-offset data were 3 meters for the 50 MHz and 100 MHz data and 2 meters for the 200 MHz data. Acquisition parameters are summarized in Table 2.

A leveling survey was done to provide accurate topographic corrections and to provide a reference datum. The leveling survey was conducted on a 1m x 1m grid with 2 m extensions on all survey boundaries to account for the antenna offset in the GPR survey. Figure 10 shows the variation of topography at the site.

Following the 3-D GPR acquisition, four boreholes were drilled to a depth of 15 m (see Fig. 6). In addition to lithology, the cores from the boreholes were used for obtaining gamma ray logs, continuous permeability sampling, selective porosity sampling and dielectric permittivity sampling. Down-hole GPR was performed in the wells. The borehole GPR data consist of single-hole and cross-hole data recorded at 100 MHz between boreholes "A", "C" and "D" (borehole "B" was not used since the hole was obstructed). Interval velocity profiles were computed from the single-hole data at a depth interval of 25 cm. In addition to the 3-D multi-frequency surveys, three 2-D surface 100 MHz GPR lines were recorded between borehole locations, "A", "C", and "D" (Fig. 6). The lines were recorded with a station spacing of 10 cm and were used for correlating sedimentary surfaces between boreholes and monitoring velocity control in the boreholes. CMP gathers were recorded at 100 MHz and 200

Table 2. 3-D GPR acquisition parameters.

	OFFSET (m)	Δt (ps)	TIME (ns)	DEPTH (m)	λ (m)
50 MHz	3.0	800	800	25.0	1.00
100 MHz	3.0	800	800	15.0	0.50
200 MHz	2.0	800	300	8.0	0.25

Table 3. 2-D GPR acquisition parameters.

	OFFSET (m)	Δt (ps)	TIME (ns)	RANGE (m)
Line AD	3.0	800	600	0.0-12.9
Line CA	3.0	800	600	0.0-10.8
Line DC	3.0	800	600	0.0- 8.6

Table 4. Filter and AGC parameters used in plotting 3-D GPR volumes.

	FILTER CORNERS Wavelength (m)	AGC WINDOW (samples)
50 MHz	0.40-0.65-1.50- 2.00	25
100 MHz	0.50-1.00-3.00-10.00	50
200 MHz	0.50-1.00-3.00-10.00	25

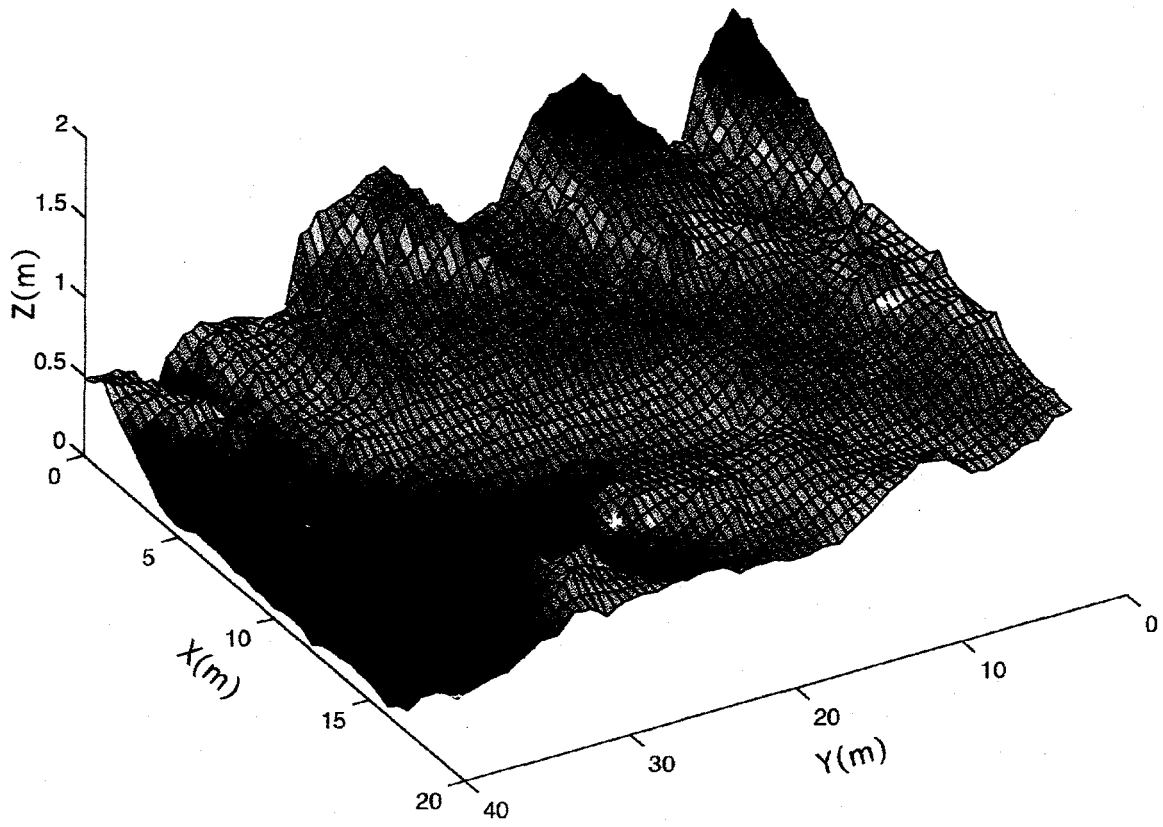

Figure 10. Surface topography obtained by leveling at the primary Coyote Basin site. X-Y coordinate system is the same as that illustrated for the geologic map in Figure 5 (Cliff edge is just off the far side of this plot). Topographic fluctuations are a result of preferential erosion of fractures.

MHz for velocity analysis as a validity check with the borehole velocity computations. Table 3 summarizes acquisition parameters for the 2-D lines.

GPR Data Processing

Data processing consisted of 1) data preparation, 2) preliminary processing, 3) 3-D depth migration and 4) display. Data preparation consisted of trace editing, time-zero and debias corrections and insertion of elevation data into the trace headers. Preliminary processing consisted of static time corrections, band-pass filter analysis, gain analysis, predictive deconvolution and velocity model building.

Data were not gained prior to depth migration. The 3-D depth migration consisted of migration aperture tests, migration velocity tests and Kirchhoff depth migration. Velocities were optimized when GPR reflections correlated with the borehole depth control. The initial velocity model was obtained from the smoothed average of the interval velocity computations from the three boreholes and was scaled to match the depth control at the boreholes for each frequency. Using this velocity, apertures were tested to collapse diffractions and enhance geologic continuity. Migration of the 3-D volumes for all three frequencies required approximately 100 hours of INTEL/860 CPU time using 8 processors.

Display consisted of black and white in-line and cross-line "wiggle-trace" profiles from the 3-D volumes. Trace mixing, band-pass filtering and AGC scaling are applied in the displays. Table 4 summarizes the filter and AGC parameters.

Figure 11 shows the representative time section of in-line 9, which passes through borehole D, for all three frequencies. Large-scale architectural elements are evident in the 50 MHz and 100 MHz data while complex sedimentary structures become evident in the 200 MHz data.

Before making a direct comparison between geologic data in the depth domain and radar data in the time domain, the radar data must be depth migrated. Developing a velocity model for the rock volume in the survey area is the *single most important* step in obtaining an accurate depth migration. At the onset of this project the degree of variability of velocity over this limited geographical area was underestimated. Only a few CMP gathers were obtained for velocity analysis. Velocity estimates were obtained in four ways:

1) using travel-time moveout analysis borrowed from seismic processing,
2) from in-situ measurements from vertical GPR profiles and cross-borehole profiles,
3) from lab measurements of dielectric permittivity, and
4) via iterative modeling of the traces at each borehole, constrained by the known depths to each main interface in the hole.

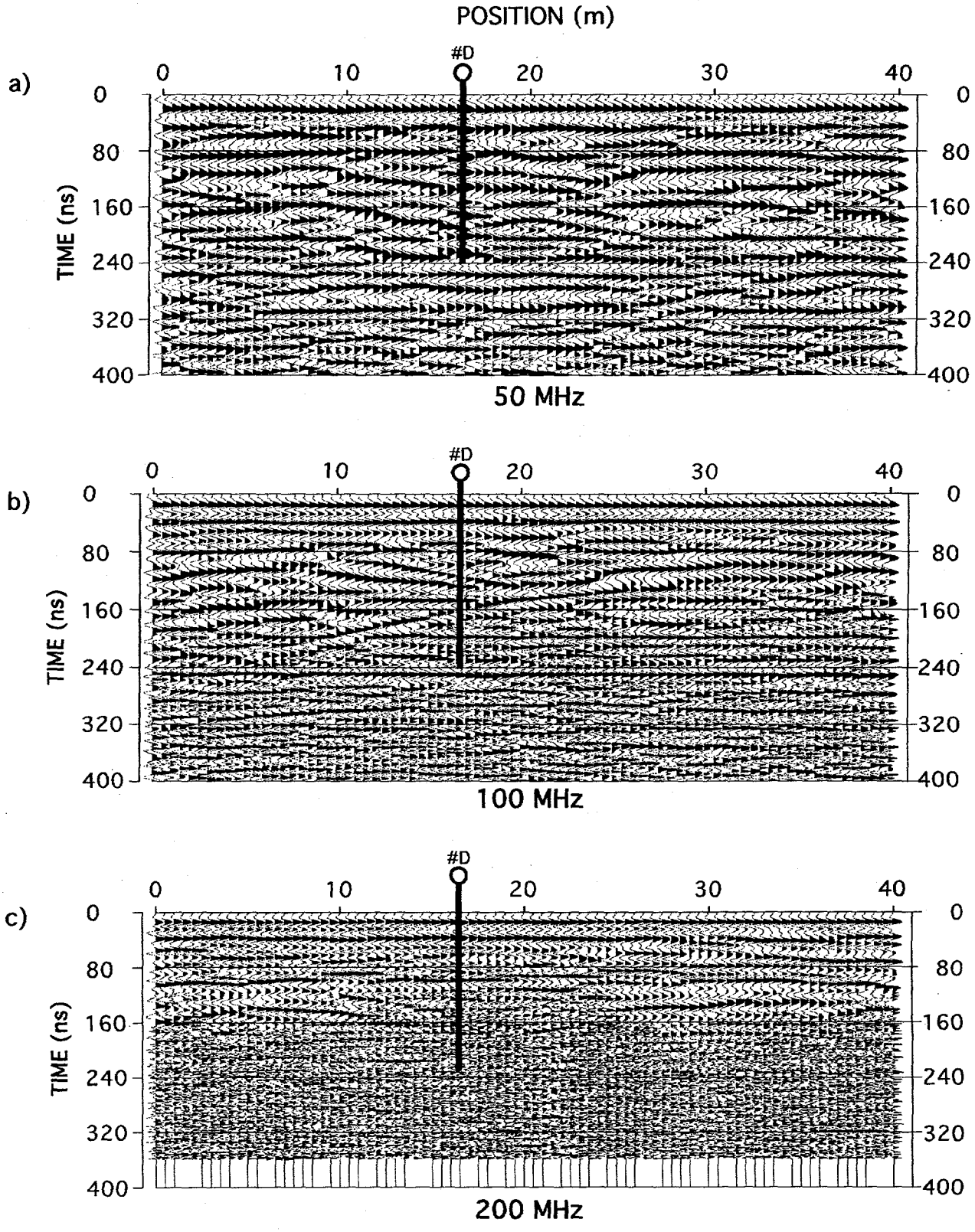

Figure 11. Time data before migration for inline 9 which is through well D (see fig. 6 for location). Data for three frequencies are shown. The corresponding slices, after 3-D migration, are shown in Fig. 12.

These provide estimates of velocity as a function of depth and position, which can then be input to 3-D migration.

Figure 12 shows the data for in-line 9 at the three frequencies, after 3-D Kirchhoff depth migration. Spatial continuity is greatly improved and sedimentary architectures are evident. The 3-D data volumes were loaded onto a GeoQuest interpretation workstation at ARCO. The workstation gives us the ability to rapidly scroll through the data volume in any direction, to enhance the data by color coding, to select trace attributes to pick horizons, and to perform a consistent 3-D interpretation with contoured outputs. Figure 13 shows a 3-D data cube of the migrated 100 MHz data. In-line 9 is shown on the cube face and the horizontal top slice is at a depth of 3 m. This figure shows the variability of architectures in 3-D and the limited spatial extent of the sedimentary structures. This figure represents the initial pass at depth imaging.

We are attempting to obtain improved velocity estimates, and thereby to improve the quality of the migrated images, from sand/clay estimates, permeability and inferred water content. There are indications of velocity variability away from the boreholes which may be largely controlled by the fracture zones. GPR velocities are dependent on lithology architectures, but more subtly on sedimentary structures which control permeability and water content. Extending the velocity model into three dimensions requires input from the interpretation and a means for obtaining spatial correlation of lithology.

LAB MEASUREMENTS OF PETROPHYSICAL AND ELECTRICAL PROPERTIES

Robert B. Szerbiak

The objective of the lab measurements is to obtain quantitative information on petrophysical and electrical properties of plug samples obtained from the cores from boreholes A, B, C, and D. Lab measurements of petrophysical and electrical properties were performed on borehole plug samples. Petrographic analysis provided quantitative mineralogy information for dielectric constant modeling, parameters for ground-penetrating radar (GPR) modeling, and porosity, and sand/clay data for the reservoir analog. Analysis of the electrical properties provided constraints for GPR velocity control, and information on fluid saturation, electrical conductivity and GPR velocity dispersion.

A set of 33 one inch diameter cylindrical plugs were drilled orthogonal to the borehole axes (see Figure 14). Plugs were taken from all four boreholes; sample locations are designated by the borehole name and depth. The sampling strategy was to obtain the full range of lithologic variation and to obtain detailed information adjacent to the bounding surfaces. Craig Forster and Steve Snelgrove (from the University of Utah) and the TerraTek Lab (Salt Lake City, Utah) provided bulk porosity and minipermeameter data from the plugs. Thin

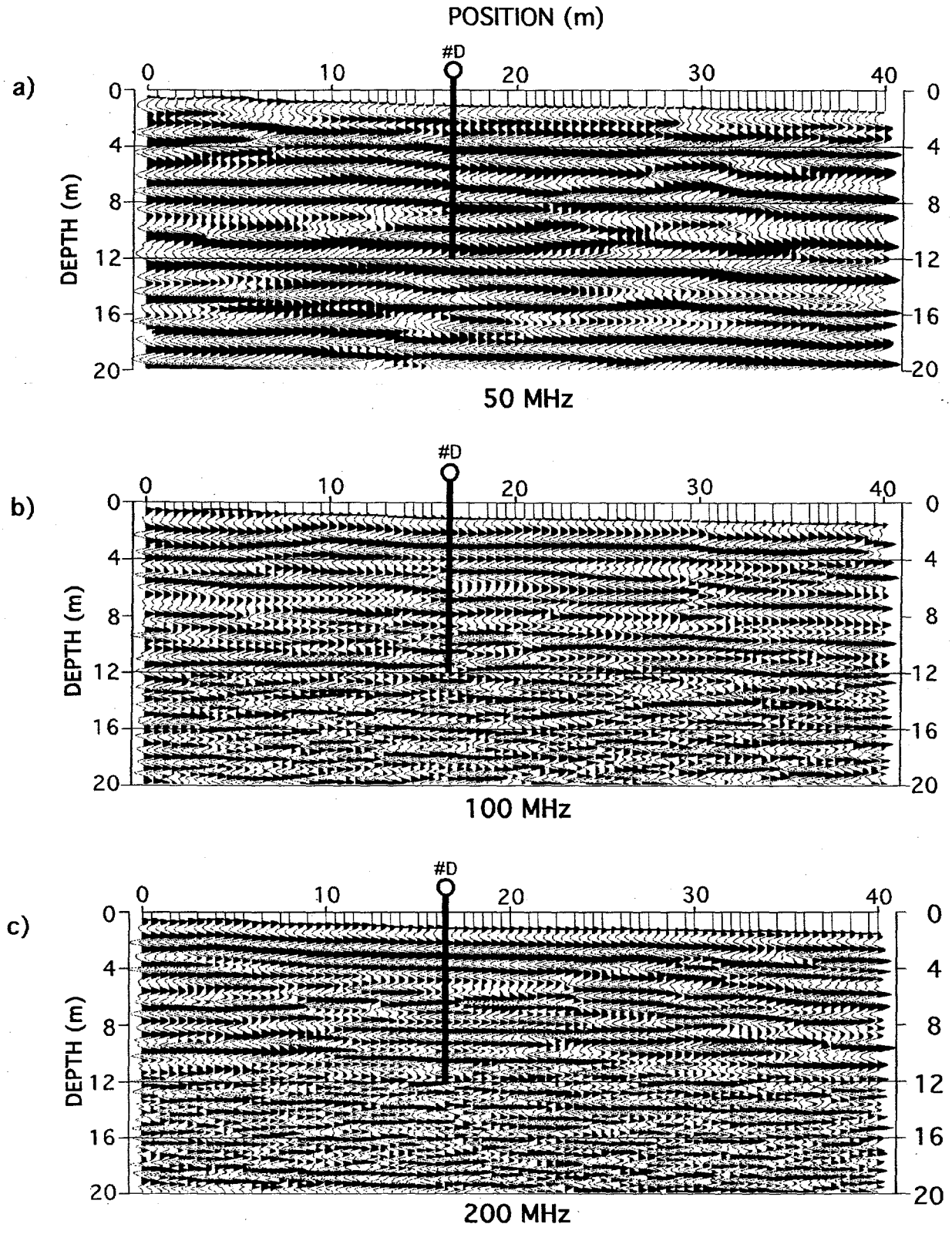

Figure 12. Same data as in Fig. 11, after depth migration. Data for three frequencies as shown.

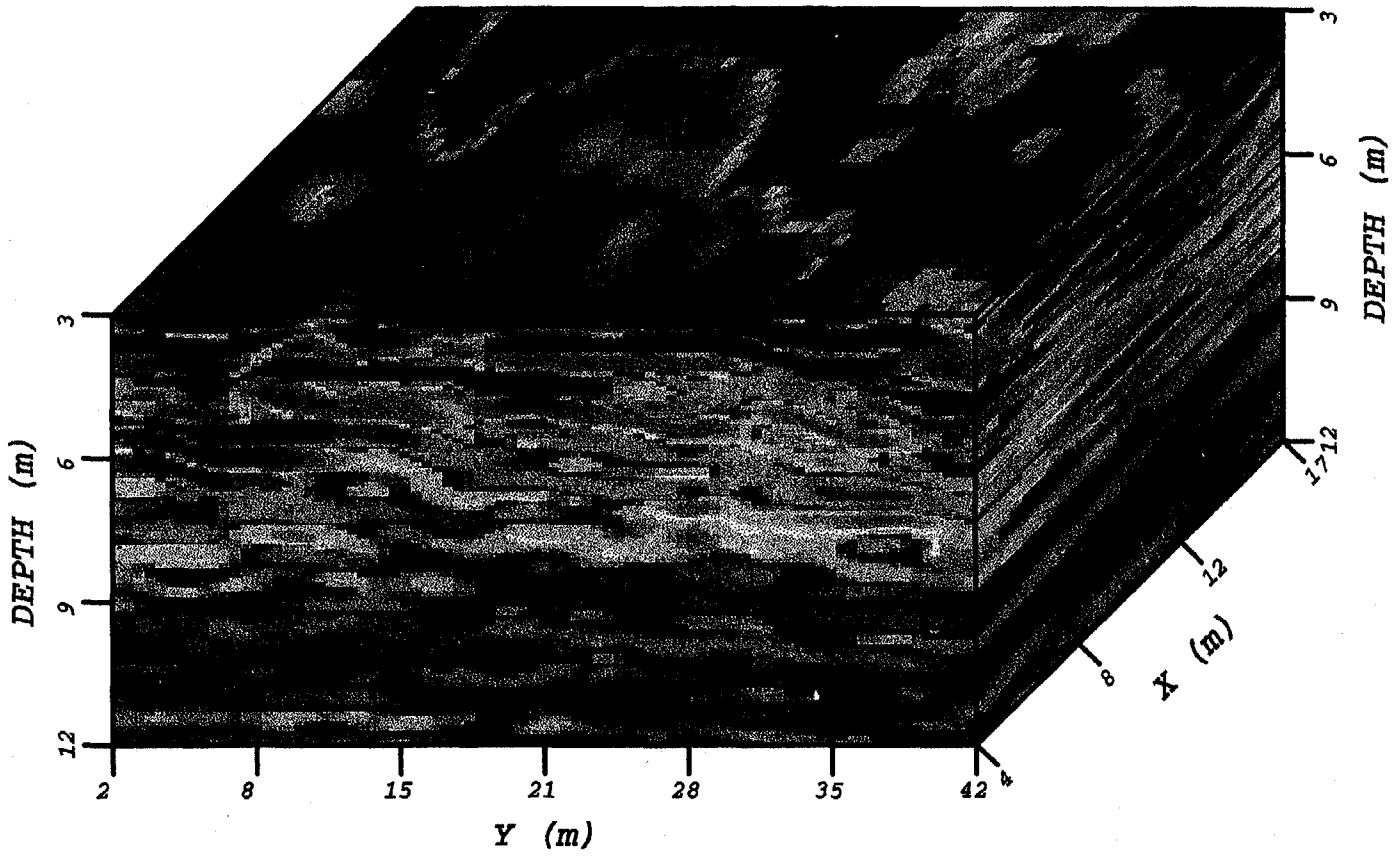

Figure 13. 3-D GPR data volume at 100 MHz. Note continuity in the cross-line (x) direction as well as in the in-line (y) direction. Colors indicate only relative amplitudes. X-Y coordinate system is the same as that illustrated for the geologic map in Figure 5.

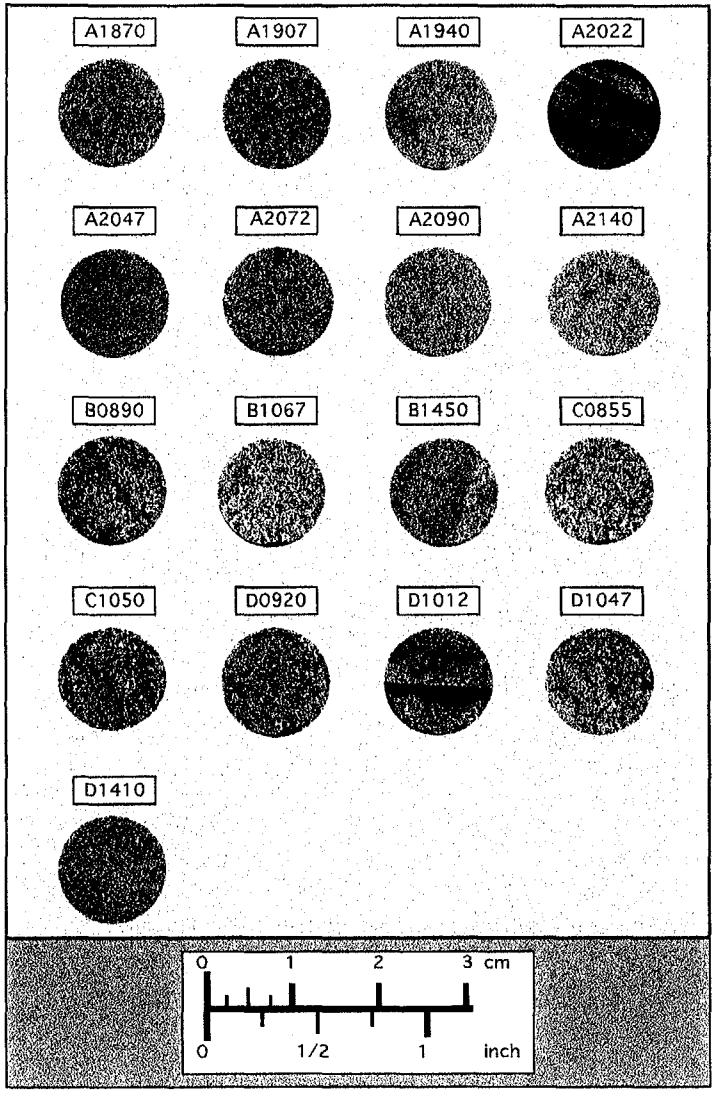

a)

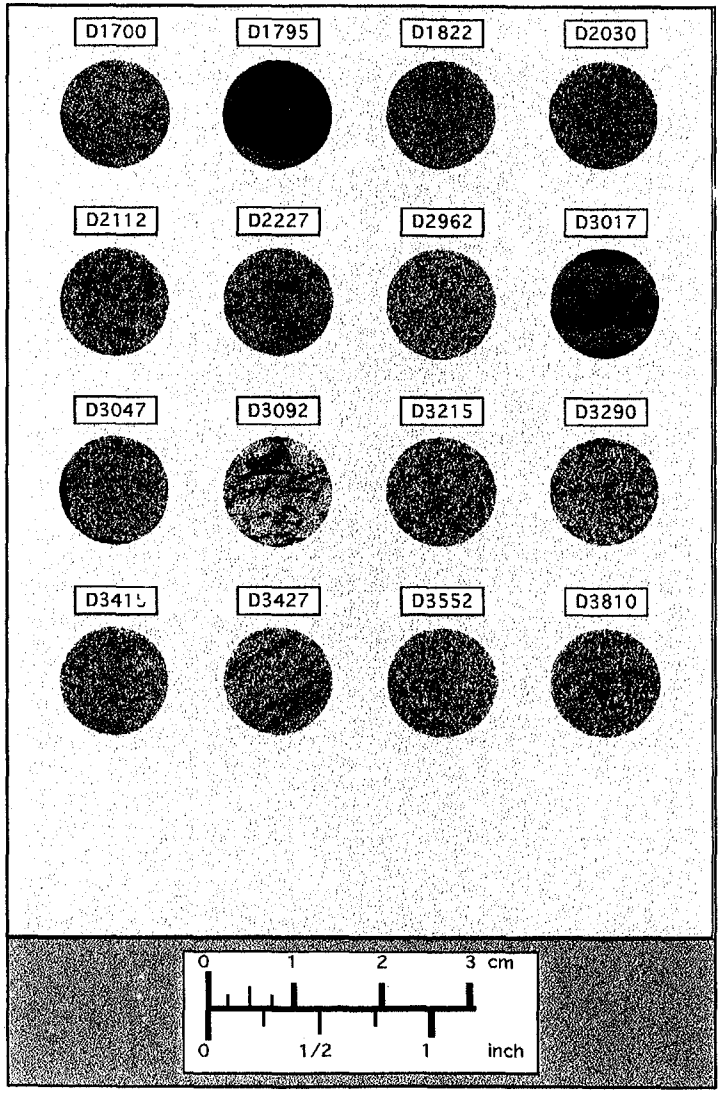

b)

Figure 14. Plug samples from boreholes "A", "B", "C", and "D".

section petrography analyses were done on the plugs by Laura Crossey and Karen Roche (from the University of New Mexico). Only summaries of these lab measurements are presented here as they were funded independently by an industry consortium, not the DOE, but all data will be fully integrated into the final model. In addition, electrical properties analyses (dielectric permittivity and electrical conductivity) were performed on the samples by Carlos Santamarina and Katherine Klein (from the Georgia Institute of Technology). Depth models were constructed at each borehole (by Rucsandra Corbeanu, UTD) from the sedimentological core logs and the petrography analysis. Electrical properties were assigned to the models based on electrical properties modeling.

Petrography Analysis

The plug samples are predominantly sandstone with four siltstone samples (A2022, D1795, D3017, and D3092; see Figs. 14a and 14b). The dominant lithologies are cross-bedded sandstone (in the upper 5 m only), intraclast conglomerates (associated with bounding surfaces), massive sandstones, siltstone and mudstone. Mudstone was not sampled since the units were not competent enough to recover a plug. Thin sections were prepared for each sample and a microscopic count analysis was done on each thin section. Counts were done for quartz, feldspar, lithics, calcite cement, opaques, total clay, and macroporosity (*porM*) as a percentage of rock volume. Table 5 presents a summary of these data in addition to the bulk porosity (*porB*), permeability, computed microporosity (*pormc*), and the dielectric constant at 100 MHz

where,

$$pormc = porB\text{-}porM.$$

Microporosity is that part of the bulk porosity which is associated with clay minerals and is not available for hydraulic conductivity. This porosity can be considered equivalent to the threshold porosity discussed by Mavko and Nur (1997). The measured macroporosity (*porM*) is generally the interconnected porosity and is available for hydraulic conduction. The rock matrix is a composite of quartz, feldspar and lithics. The clay is composed of kaolinite, chlorite, illite and an unidentified clay. These clays have comparable characteristics with respect to water affinity and dielectric response. A further analysis of the clay will require x-ray diffraction analysis. In the siltstone samples there is approximately 50% more clay than in sandstone samples, macroporosities are 90% lower, and permeabilities are less than 1% lower whereas their microporosities and matrix content are nearly equal.

Table 5 Average values from petrography analysis.

	SANDSTONE AVERAGE	SILTSTONE AVERAGE
Rock Matrix	71.8%	72.9%
Quartz	55.9%	53.9%
Feldspar	11.4	14.5%
Lithics	4.4%	4.6%
Clay	14.0%	22.7%
Opaques	1.3%	2.4%
Bulk Porosity	18.6%	11.75%
Macro Porosity	7.5%	0.75%
Micro Porosity	11.1%	11.0%
Calcite Cement	5.3%	1.4%
Permeability	33.9 md	0.2 md
Dielectric Constant	4.1	5.9

Macroporosity is approximately 50% of bulk porosity in the sandstone whereas it is approximately 5% of bulk porosity in the siltstone samples. These data show that a relatively small increase in clay content can cause a large reduction in macroporosity and permeability.

Calcite cement is insignificant in the siltstone samples and opaque minerals are insignificant in all samples. The siltstone samples show approximately 50% higher dielectric constant than the sandstone samples. This result is expected since the more permeable and porous sandstone samples have a much smaller ability to retain water than the siltstone samples. This analysis will be used for predicting water content and electric properties of the samples.

Figures 15a-15h show distribution densities of quartz, feldspar, lithics, calcite cement, clay, dielectric constant, macroporosity and permeability. Those quantities which have one-sided distributions (calcite, clay and permeability) have a dominant influence on the electrical properties of the samples. These figures indicate a large number of samples for clay <15%, calcite <6%, permeability <20 md and dielectric constant <4.5.

Figure 16a is a crossplot of (smoothed) rock matrix, clay and calcite cement with dielectric constant (at 100 MHz) and Figure 16b is a crossplot of permeability and macroporosity with dielectric constant. Macroporosity, permeability, and clay content. controls water content in the rocks which directly influences the dielectric constant. Figure 16c contains smoothed crossplots of macroporosity and permeability with clay content. These figures show the dependence of macroporosity and permeability on clay content and the relative insensitivity to rock matrix content. Macroporosity and permeability decrease with increasing clay content. Figure 16d shows the (smoothed) correlation between macroporosity and permeability. A non-linear trend is evident as predicted by the Kozeny-Carman equation (Kozeny, 1927; Carman, 1937; Fig. 17).

A function is needed to relate macroporosity to permeability for the entire range of data from the boreholes. The Kozeny-Carman relation:

$$\kappa = B\phi^3 d^2/(1-\phi)^2, \qquad (1)$$

is commonly used for this purpose, where κ is permeability, ϕ is porosity, d is grain diameter (measured in μ) and B is a geometrical factor. This equation has been modified from the original Kozeny-Carman relation to incorporate a well-sorted packing of spherical grains. This model is referred to here as the Kozeny-Carman$_1$ model, where, $B = 3$ and $d = 100\mu$. Figure 17a shows this model (dashed line) plotted with bulk porosity and permeability data from core plug samples. The data fit is poor at low porosities. The misfit is due to the bulk porosity not being the effective porosity. The threshold porosity, ϕ_T, is the minimum porosity necessary before pore spaces become connected for hydraulic conductivity. The Kozeny-Carman

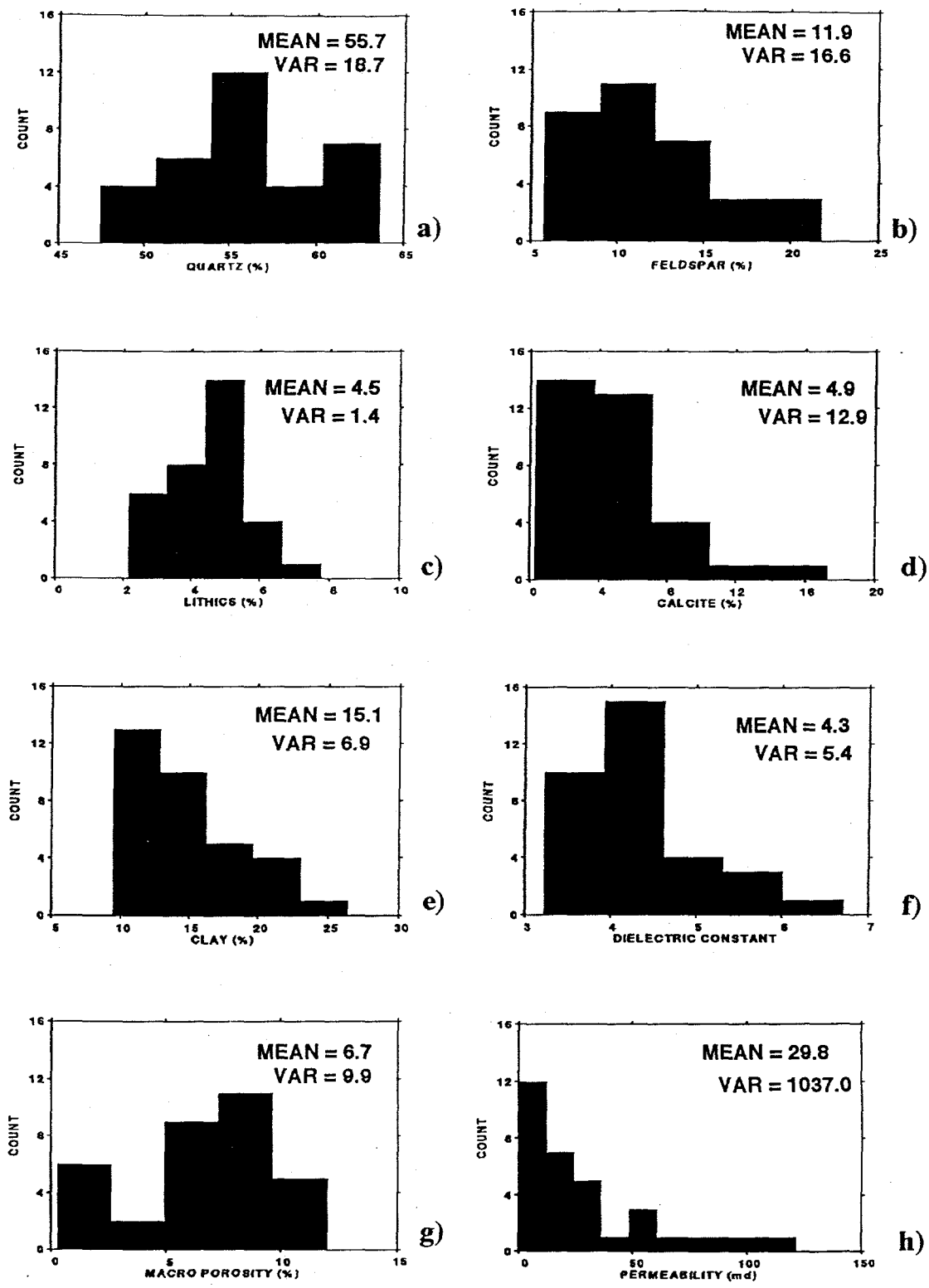

Figure 15. Sample distribution densities. a) quartz, b) feldspar, c) lithics, d) calcite cement, e) clay, f) dielectric constant, g) macro porosity, and h) permeability.

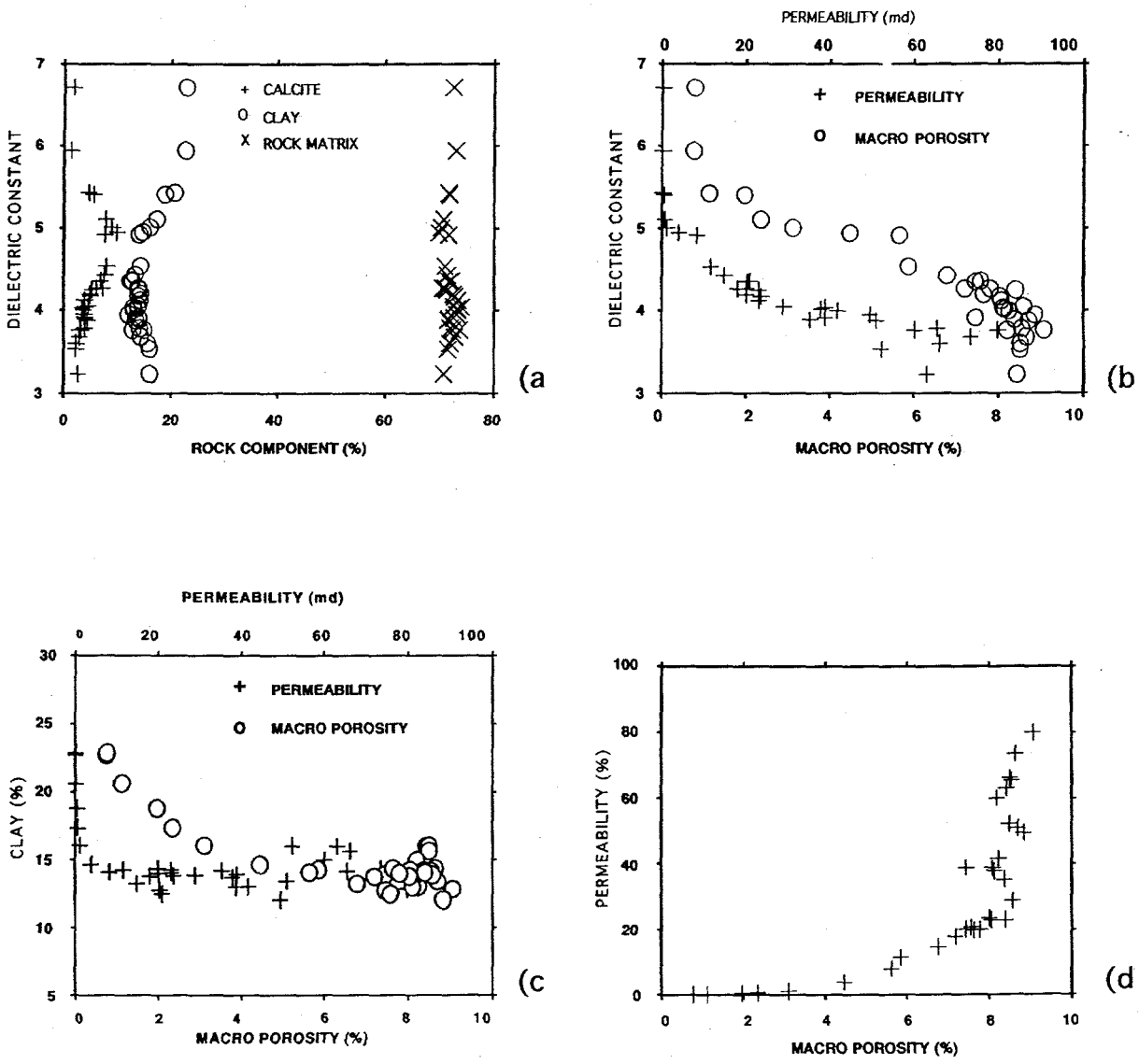

Figure 16. Cross plots of sample properties.

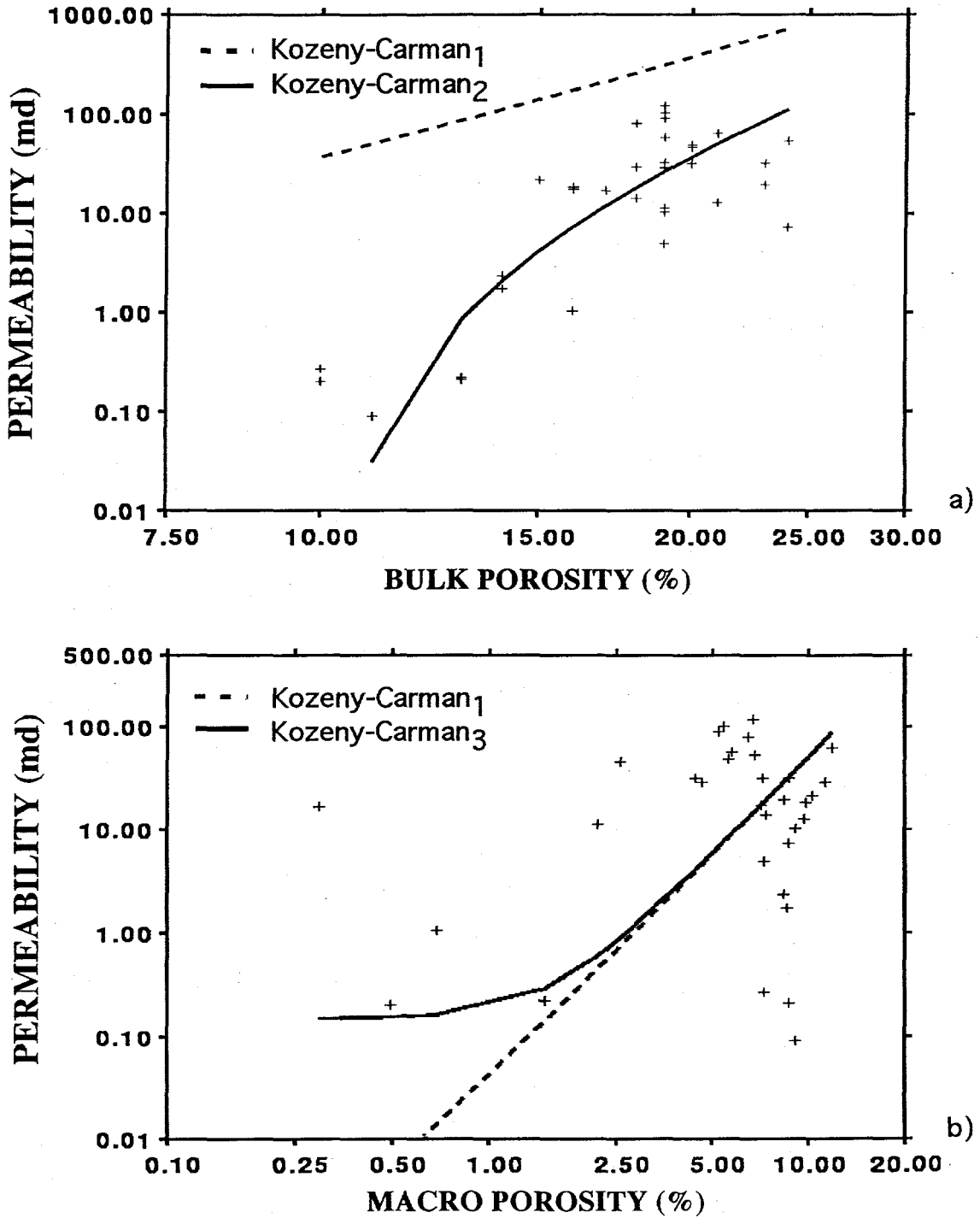

Figure 17. Kozeny-Carman fit to plug sample data. a) bulk porosity measurements and b) macro porosity measurements.

equation has been modified by removing threshold porosity from bulk porosity (Mavko and Nur, 1997), to give

$$\kappa = B(\phi - \phi_T)^3 d^2/(1+\phi_T-\phi)^2. \quad (2)$$

This second model is referred to as the Kozeny-Carman$_2$ model, where $\phi_T = 10\%$. ϕ_T was approximated from the average micro porosity. Figure 17a shows the improved fit of this model (solid line) to the core plug sample data. The two models converge at high porosity values and the modified model becomes nearly linear at porosities <13% (log-log plot). Rather than using bulk porosity data, macroporosity data measured from the thin sections can be used to more closely approximate effective porosity. Figure 17b (dashed line) shows the Kozeny-Carman$_1$ model plotted against macroporosity data, where $B = 4$. The macroporosity is all < 13% and has a linear relationship with permeability (log-log plot). The fit is good except for the four siltstone samples which have the lowest porosities. There appears to be a lower limit for the permeability even at low porosities. This indicates that the available clay particles have occupied the maximum inter-granular pore space and a further reduction in pore space is insignificant for hydraulic conductivity. Again, the Kozeny-Carman$_1$ model is modified by adding a constant to account for the lower limit of permeability,

$$\kappa = B[\phi^3\}d^2/(1-\phi)^2 + C], \quad (3)$$

where C = constant. This model is referred to as the Kozeny-Carman$_3$ model, where C = 0.0375. This modification is equivalent to adding a second-order term to the numerator of equation (1) that depends on rock matrix content. The maximum contribution of C is at the lowest porosities. Figure 17b (solid line) shows the improved fit of this model.

Electrical Properties Analysis

Electrical property measurements were used to provide estimates of pore water content and to provide constraints on velocity and attenuation for depth migration and GPR modeling. The properties were measured in the laboratory on the same 33 plug samples used in the petrographic analysis. Disc samples, 1/4 inch in thickness, were cut and polished from the plug samples (see Figure 14). Measurements consisted of the frequency dependent real and imaginary parts of the complex dielectric permittivity and the data covered a frequency range of 5 Hz to 1 GHz.

The behavior of electromagnetic energy is described by Maxwell's relationships and the wave equation in the frequency domain is,

$$\nabla^2 = -\{\omega^2\mu\varepsilon - i\omega\mu\sigma\}E, \quad (4)$$

where, ω is angular frequency, μ is magnetic permeability, σ is conductivity and ε is dielectric permittivity. Magnetic permeability is insignificant for most earth materials whereas conductivity and permittivity are the primary rock properties controlling electromagnetic wave propagation. These two quantities are in general complex and are frequency dependent.

A description of the laboratory measurement procedures for conductivity and dielectric permittivity is given by Klein and Santamarina (1997). The complex dielectric permittivity consists of a real part, due to the polarization of the material, and an imaginary part, due to polarization losses in the material (see Santamarina and Fam, 1997),

$$K^*_{eff} = K'_{eff} - iK''_{eff}, \quad (5)$$

with,

$$K'_{eff} = \sigma' + \sigma''/\omega\varepsilon_0,$$

and,

$$K''_{eff} = K'' - \sigma'/\omega\varepsilon_0,$$

where K^*_{eff} is the effective complex relative dielectric permittivity, K'_{eff} is the effective real part of permittivity and accounts for the material polarizability, K''_{eff} is the effective imaginary part of permittivity and accounts for polarization losses in the material, σ' is the real part of conductivity and accounts for DC conductivity, σ'' is the imaginary part of conductivity and accounts for out-of-phase conduction (insignificant), K'' is polarization and ε_0 is the dielectric permittivity in a vacuum.

High-frequency measurements recorded the real and imaginary parts of permittivity directly. Polarization losses were negligible and the imaginary part was a function of DC conductivity. Low-frequency measurements use a lossy RC equivalent circuit, where resistance (R) and reactance (X) are measured directly (Fig. 18). Complex impedance is expressed as $Z^* = R - iX$, where R is resistance and $X = 1/\omega C$ is reactance, C is capacitance. Admittance, $Y^* = i\omega C^*$, $C^* = K^*\varepsilon_0 A/L$, where A and L are the surface area and separation of the electrodes respectively. The real and imaginary parts of the admittance give the real and imaginary parts of the permittivity respectively,

$$K' = Imag(Y^*)L/A\,\omega\varepsilon_0, \quad (6a)$$

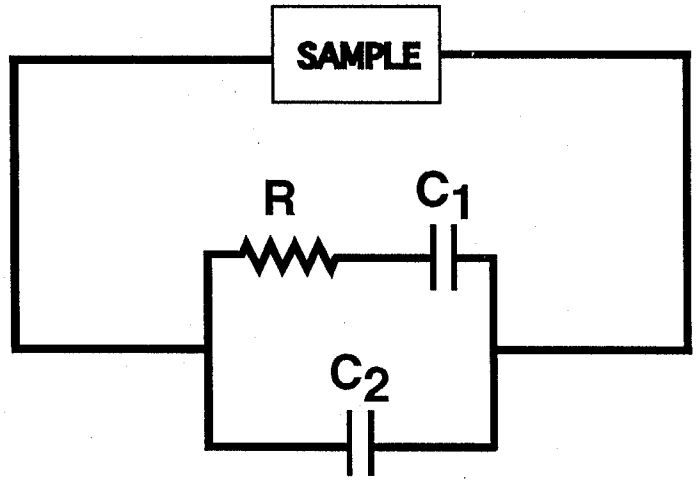

Figure 18. Lossy equivalent RC circuit. R is resistance of sample, C1 is capacitance of the primary circuit and C2 is capacitance due to electrode polarization.

and

$$K' = Real(Y^*)L/A\omega\varepsilon_0. \quad (6b)$$

Dielectric permittivity measurements required two network analyzers, one for the low-frequency range and one for the high-frequency range. The low-frequency measurements (5 MHz - 10 MHz) were made with an HP 4192A network analyzer (Fig. 19a) and a single measurement was made for each frequency for each disc sample using a parallel plate electrode configuration to measure capacitance (Fig. 19b). Conductive paint was used on both faces of the sample to compensate for surface irregularities when making contact with the electrodes. The high-frequency measurements (10 MHz - 1 GHz) were made with an HP 8752A network analyzer (Fig. 20a). Five measurements were made for each frequency on each side of the sample with an HP 8750A high-frequency, open-ended coaxial probe (Fig. 20b). Multiple measurements were necessary since the sampling area of the probe is 4 mm and averaging the measurements provided a bulk measurement for each sample. An analog to this device is a cylindrical capacitor with the axis of the cylinder normal to the axis of the disc sample. The electric field was polarized in the plane parallel to bedding for low-frequency measurements and is polarized in the plane normal to bedding for high-frequency measurements.

Permittivity measurements were conducted at three water saturation levels; oven-dried, where samples were dried for 24 hours at 100°C to remove pore-space water; air-dried, where samples were allowed to equilibrate to ambient atmospheric saturation conditions; and fully-saturated, where samples were fully saturated under vacuum. The fully saturated samples used deionized water (3.9×10^{-4} S/m), and were chosen from each major lithology zone. Computation of saturation levels were based on weight; samples were weighed before and after saturation. Table 6 summarizes the saturation data. The largest ambient saturations occurred for the siltstone samples, averaging 25.5%, whereas saturations for the sandstone samples average 4.6%. Saturations for fully saturated samples were > 90%. The sample D1795 had a computed saturation > 100% due to errors introduced from incomplete desaturation during the oven drying procedure. The ambient (air-dry) saturation levels in the siltstone samples are probably high due the low permeability values. Knoll and Knight (1994) and Knoll et al. (1995) have developed relationships between porosity, permeability, clay content and dielectric constant for an unconsolidated mixture of sand and clay. The applicability of these relationships to consolidated clastic rocks are presently being investigated.

Sources of error for low-frequency measurements are polarization losses including electrode polarization at frequencies below 100 KHz and cable inductance for highly conductive materials at frequencies above 1 MHz. It is difficult to obtain accurate conductivity

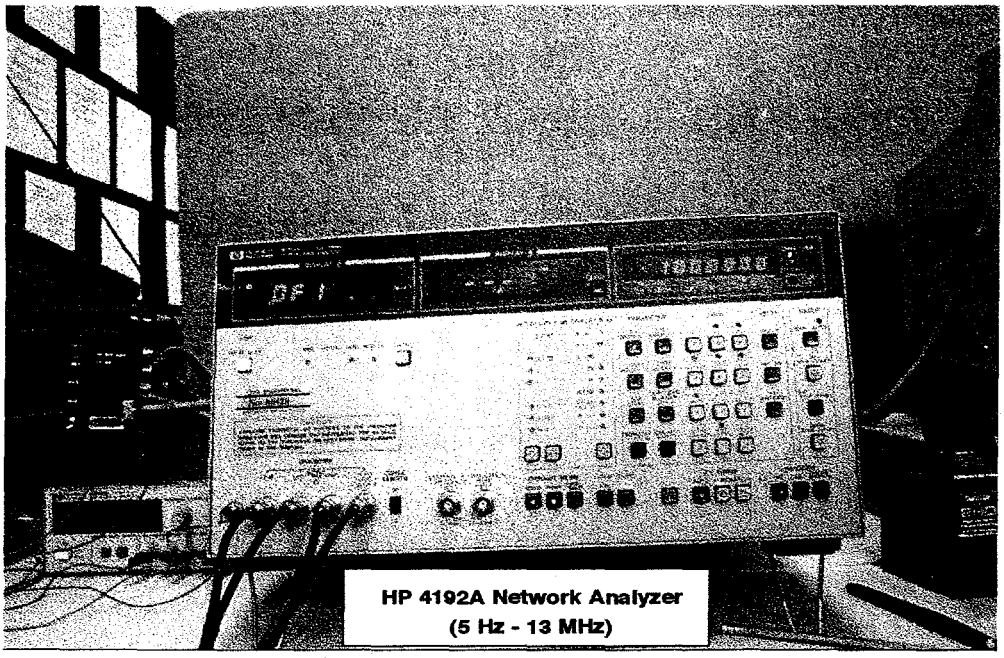

a)

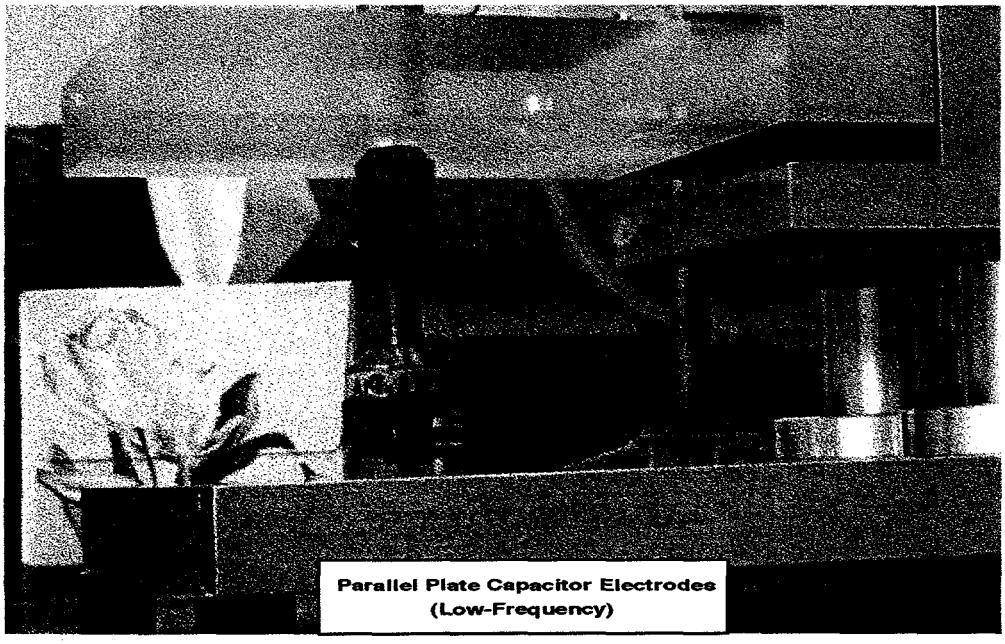

b)

Figure 19. Low-frequency dielectric permittivity measurement. a) HP 4192A network analyzer and b) parallel plate capacitor electrodes.

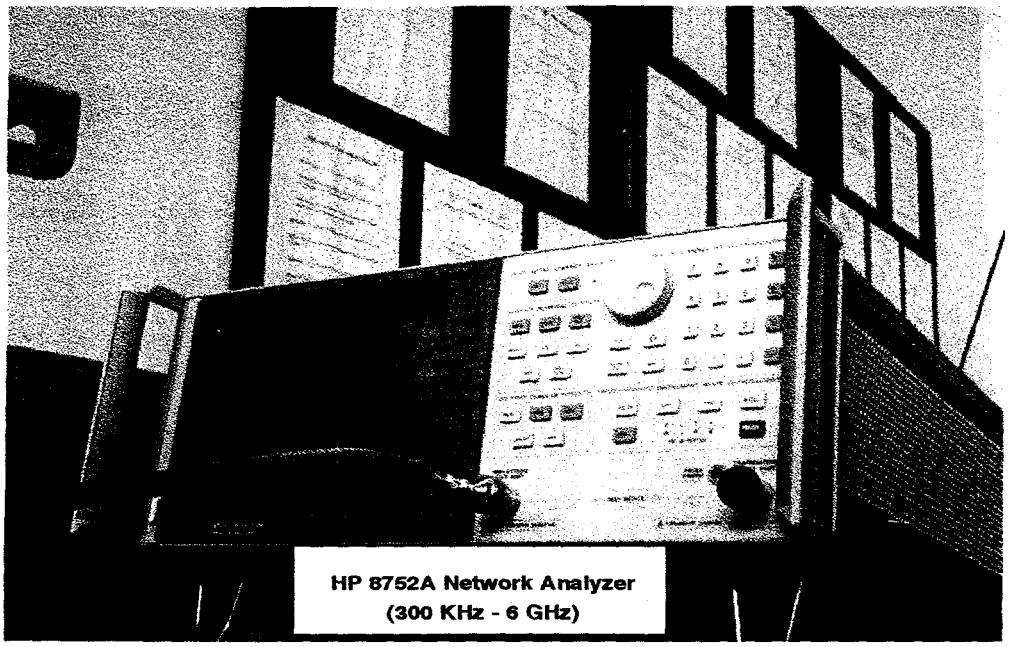

a)

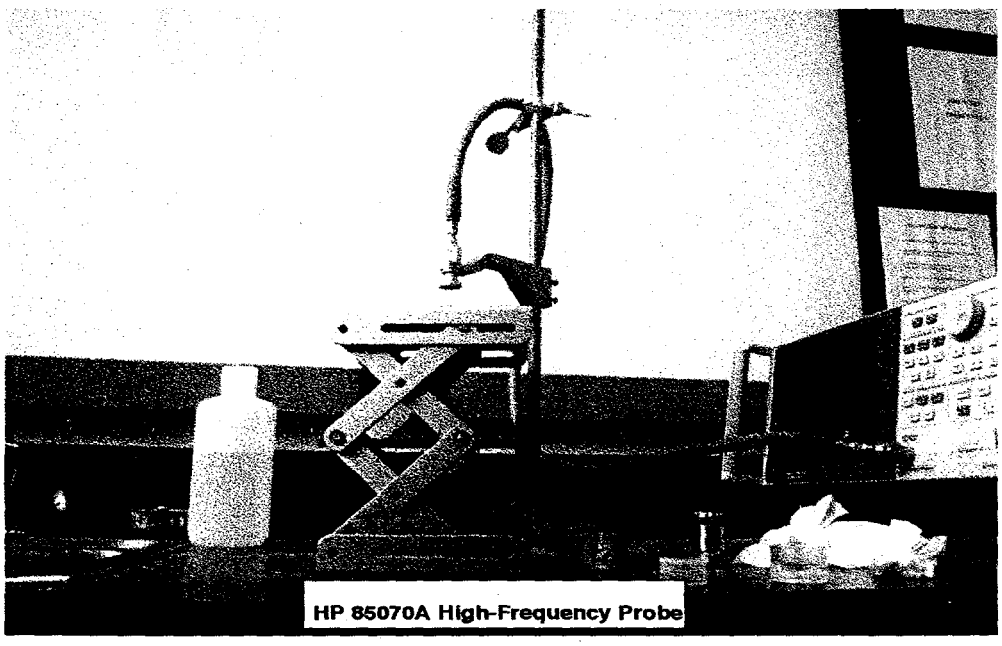

b)

Figure 20. High-frequency dielectric permittivity measurement. a) HP 8752A network analyzer and b) HP 8750A high-frequency probe.

Table 6. Disc sample saturation data: Fully saturated samples (*).

	Sample	WT_oven(gm)	WT_air(gm)	WT_sat(gm)	Por(%)	Den(gr)	Sw_air(%)	Sw_sat(%)
*	A1870	6.969	6.993	7.488	17.00	2.67	4.5	97.1
	A1907	7.662	7.679		10.00	2.67	5.3	
	A1940	7.088	7.130		16.00	2.67	8.3	
	A2022	5.010	5.083		13.00	2.67	26.0	
	A2047	6.775	6.798		19.00	2.66	3.8	
*	A2072	6.666	6.685		20.00	2.65	3.0	
	A2090	6.078	6.096	6.566	19.00	2.66	3.4	91.0
	A2140	6.176	6.188		18.00	2.65	2.3	
	B0890	6.707	6.724		19.00	2.63	2.8	
	B1067	6.644	6.660		19.00	2.62	2.7	
	B1450	6.763	6.782		20.00	2.65	3.0	
*	C0855	6.689	6.706	7.275	19.00	2.63	2.8	98.2
	C1050	6.677	6.698		18.00	2.62	3.8	
	D0920	6.653	6.667		19.00	2.62	2.4	
	D1012	3.418	3.436		24.00	2.65	4.4	
	D1047	6.898	6.919		16.00	2.63	4.2	
	D1410	6.673	6.700		20.00	2.64	4.3	
	D1700	6.559	6.617		19.00	2.62	9.9	
*	D1795	7.180	7.264	7.573	10.00	2.63	27.7	129.6
	D1822	6.922	6.956		18.00	2.64	5.9	
	D2030	6.430	6.473		23.00	2.65	5.9	
	D2112	7.198	7.234		14.00	2.64	8.1	
*	D2227	7.134	7.168	7.556	14.00	2.63	7.7	95.6
	D2962	6.373	6.404		23.00	2.65	4.3	
	D3017	6.821	6.900		13.00	2.61	20.2	
	D3047	5.520	5.560		24.00	2.64	6.1	
	D3092	8.046	8.152		11.00	2.62	27.9	
	D3215	6.680	6.701		19.00	2.64	3.5	
	D3290	6.488	6.525		21.00	2.65	5.7	
	D3415	7.010	7.032		16.00	2.64	4.3	
	D3427	7.071	7.098		15.00	2.61	5.6	
*	D3552	6.720	6.748	7.301	19.00	2.64	4.7	97.3
	D3810	6.657	6.670		21.00	2.70	2.0	

estimates in these frequency ranges. The high-frequency measurements are sensitive to coaxial cable motion and measurements are calibrated measuring air, deionized water and plexiglas.

At this time, only the high-frequency data have been utilized since the GPR field experiment at Coyote Basin is in the high-frequency range (50-200 MHz). The real part of the permittivity is related to propagation velocity by, $V = V_0/\sqrt{K'}$, where V_0 is velocity in a vacuum and the imaginary part of permittivity is related to conductivity by, $\sigma' = K''\omega\varepsilon_0$. Attenuation is $\alpha = 8.696\ (1/2\varepsilon_0 V_0)(\sigma'/\sqrt{K'})dB/m$. Using average values for K' in both sandstone and siltstone gives attenuation equations of,

$$\alpha_{sand} = 1896\sigma'/\sqrt{K'}, \tag{7a}$$

$$\alpha_{siltstone} = 1455\sigma'/\sqrt{K'}, \tag{7b}$$

Table 7 summarizes the real and imaginary part of permittivity for frequencies of 50 MHz, 100 MHz and 200 MHz.

Samples A1870 (sandstone) and D1795 (siltstone) (Fig. 21) compare extreme permittivity values for lithologies analyzed from Coyote Basin. Figures 22a and 22b show the real and imaginary part respectively for oven-dried samples A1870 (heavy line) and D1795 (solid line). There is virtually no dispersion since the conductivity term is insignificant and K' should measure pure grain permittivity. Figures 23a and 23b show the real and imaginary part respectively for the air-dried samples A1870 (the heavy line) and D1795 (solid line). Dispersion decreases with frequency and K' is 25% higher for D1795 than for A1870 whereas K'' is 100% higher for D1795 than for A1870 at 100 MHz. Figures 24a and 24b show the real and imaginary part, respectively, for the fully saturated samples A1870 (heavy line) and D1795 (solid line). Dispersion decreases rapidly with frequency and K' is approximately 30% higher for D1795 than for A1870 whereas K'' is approximately 200% higher for D1795 than for A1870 at 100 MHz. In addition, there is a crossover of dielectric constant at 200 MHz probably due to ion mobility.

Numerical Synthesis of GPR Data

Based on the petrophysical lab measurements, including permittivity, permeability, porosity, and compositional data (e.g., clay content) from which electromagnetic wave velocities and attenuations are estimated, and in-situ velocity measurements, preliminary models of the distributions of electrical properties were constructed. These were then input to

Table 7. Plug sample dielectric permittivity as a function of frequency.

Sample	50 MHz Kreal	50 MHz Kimag	100 MHz Kreal	100 MHz Kimag	200 MHz Kreal	200 MHz Kimag
a1870	4.504	0.590	4.349	0.484	4.246	0.337
a1907	5.502	0.826	5.107	0.500	4.934	0.375
a1940	5.462	1.229	4.948	0.819	4.698	0.581
a2022	7.582	2.777	6.714	2.016	6.057	1.432
a2047	4.694	0.828	4.273	0.569	4.107	0.412
a2072	4.235	0.673	3.886	0.429	3.723	0.327
a2090	4.662	0.719	4.266	0.453	4.142	0.323
a2140	4.359	0.625	4.047	0.430	3.938	0.305
b0890	3.803	0.360	3.755	0.213	3.670	0.171
b1067	3.825	0.422	3.597	0.243	3.524	0.180
b1450	4.012	0.522	3.905	0.357	3.812	0.220
c0855	4.165	0.648	4.017	0.444	3.923	0.284
c1050	4.123	0.426	3.999	0.290	3.902	0.177
d0920	3.824	0.383	3.763	0.266	3.664	0.159
d1012	3.288	0.398	3.228	0.308	3.132	0.231
d1047	4.175	0.424	4.116	0.315	4.025	0.164
d1410	4.403	0.716	4.170	0.505	4.026	0.323
d1700	4.049	0.807	3.876	0.505	3.683	0.368
d1795	5.963	1.710	5.435	1.178	5.021	0.848
d1822	4.687	0.806	4.539	0.498	4.347	0.334
td2030	3.902	0.684	3.775	0.410	3.585	0.296
d2112	5.192	1.008	4.915	0.738	4.663	0.537
d2227	5.398	1.160	5.011	0.846	4.788	0.594
d2962	3.548	0.537	3.534	0.281	3.389	0.219
d3017	5.958	1.543	5.409	1.244	4.992	0.939
d3047	4.304	0.938	4.044	0.779	3.819	0.539
td3092	6.398	1.276	5.935	1.121	5.571	0.848
d3215	4.373	0.750	4.254	0.578	4.111	0.389
d3290	4.125	0.728	3.950	0.600	3.802	0.406
d3415	4.472	0.619	4.361	0.516	4.262	0.342
d3427	4.532	0.558	4.427	0.479	4.308	0.315
d3552	4.346	0.704	4.200	0.568	4.076	0.385
d3810	3.815	0.351	3.782	0.299	3.715	0.192

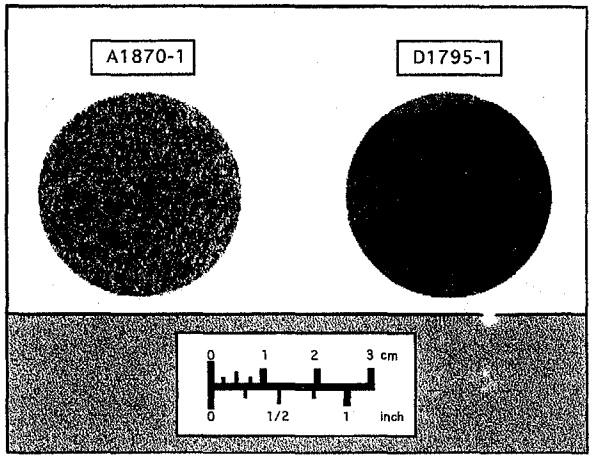

Figure 21. Plug samples A1870 and D1795.

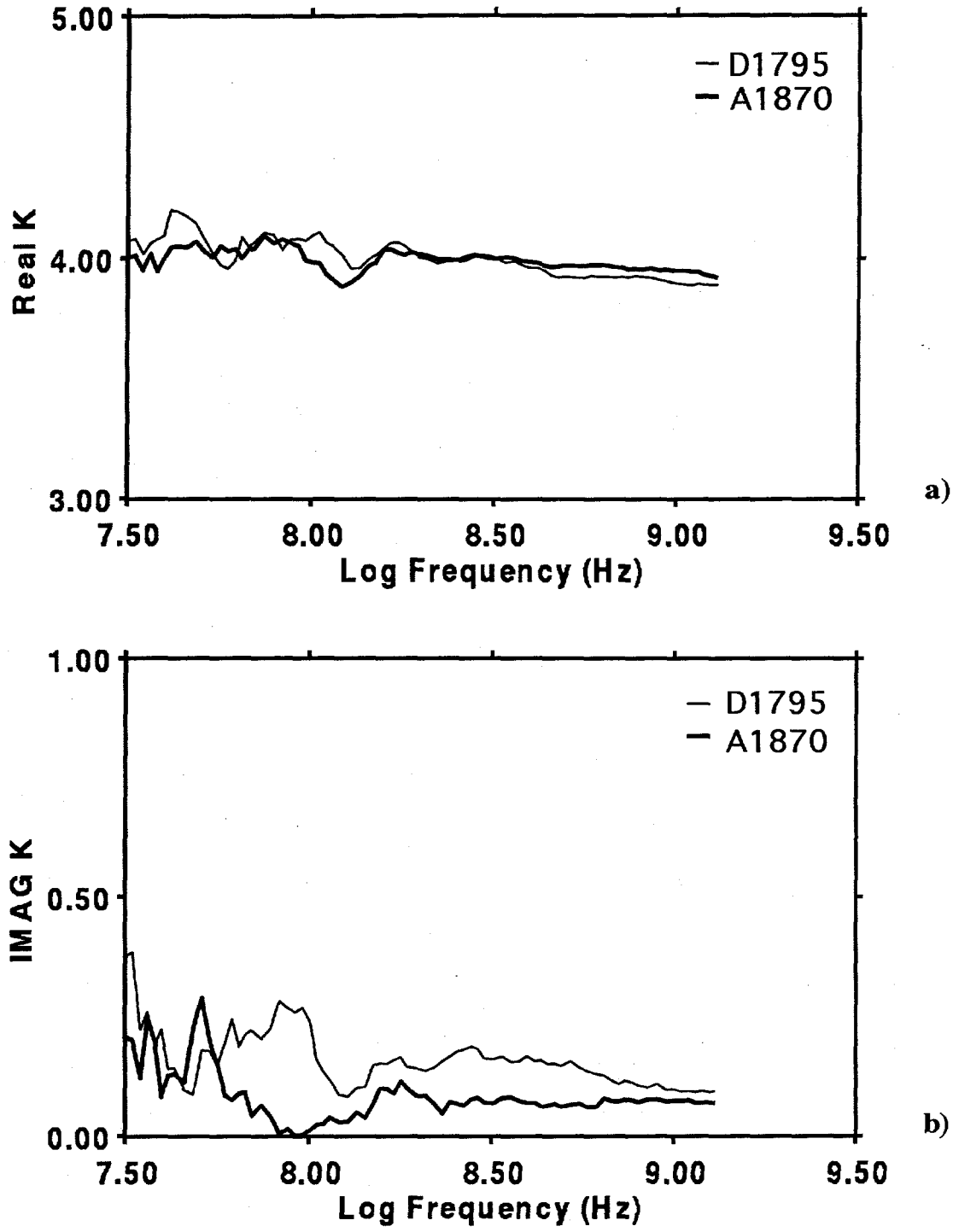

Figure 22. Oven-dry high-frequency dielectric permittivity data. a) real part of permittivity and b) imaginary part of permittivity.

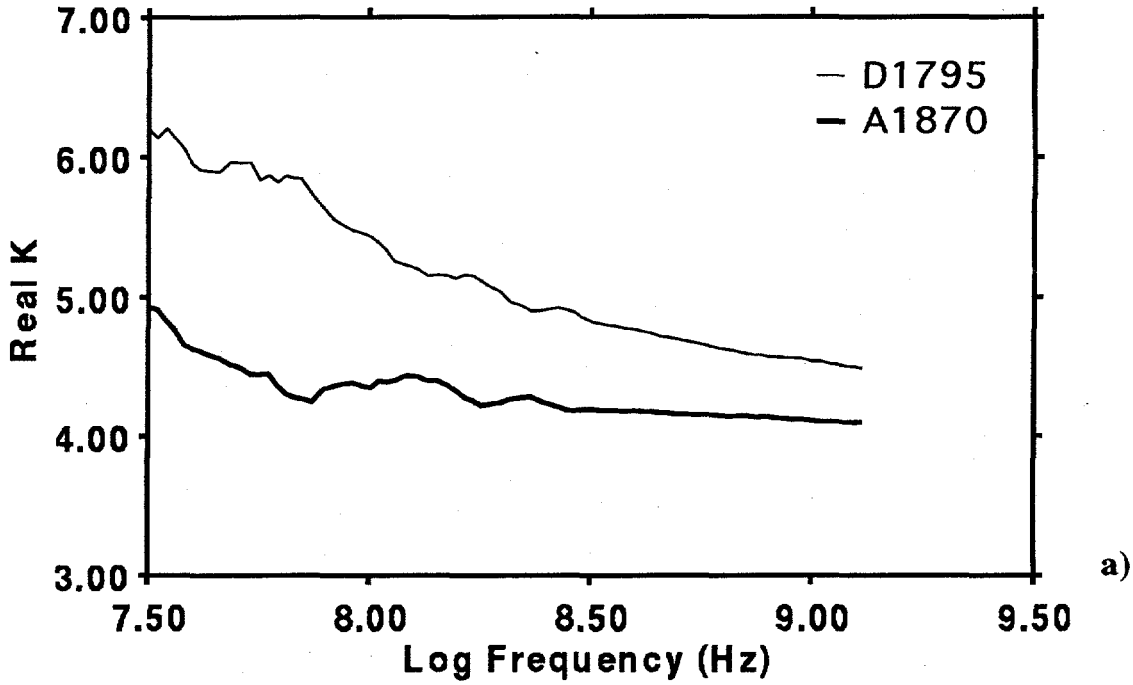

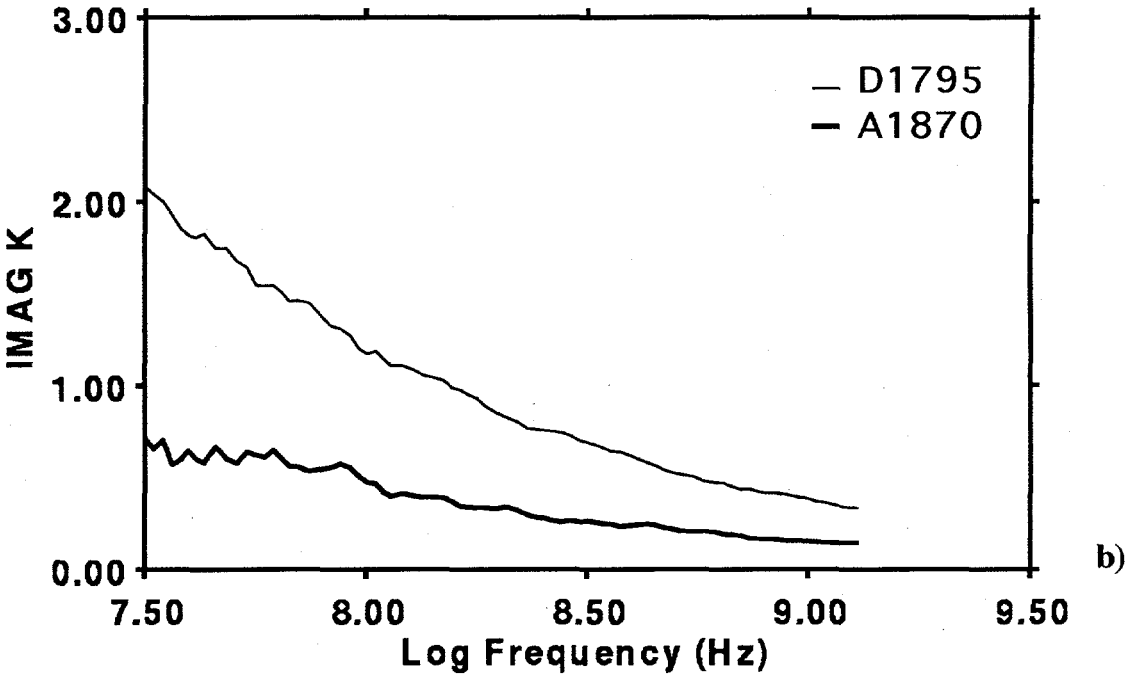

Figure 23. Air-dry high-frequency dielectric permittivity data. a) real part of permittivity and b) imaginary part of permittivity.

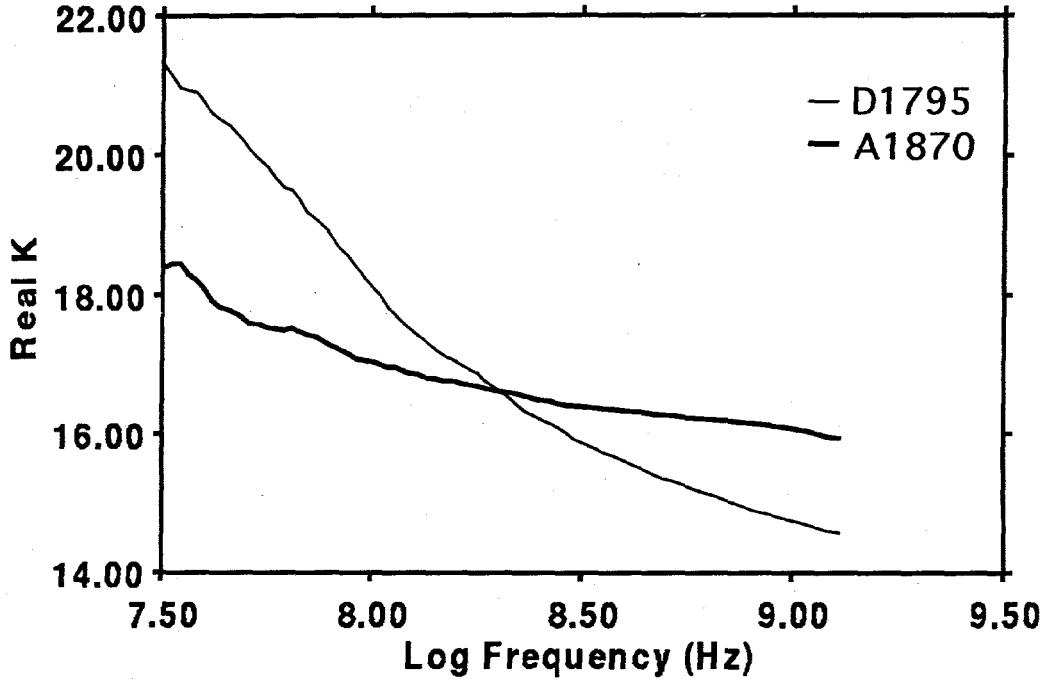

a)

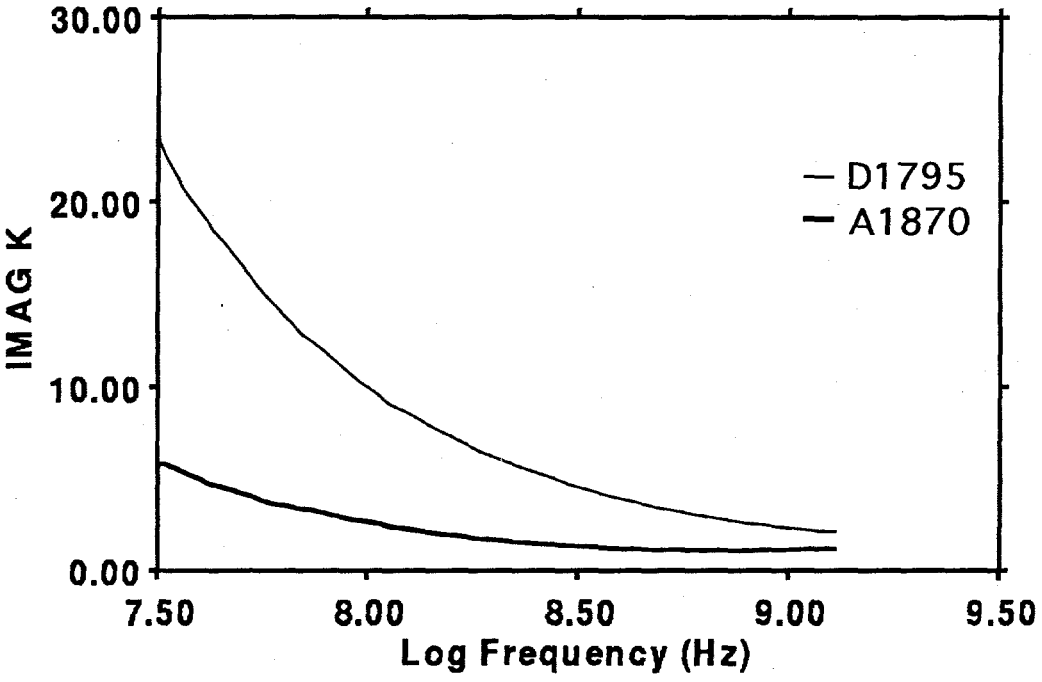

b)

Figure 24. Saturated high-frequency dielectric permittivity data. a) real part of permittivity and b) imaginary part of permittivity.

simulations, for various GPR survey geometries, using the 2.5-D solution of Maxwell's equations developed by Xu and McMechan (1997).

Figure 25 shows snapshots of the solution for a vertical electric dipole source located at 3 m depth in a borehole in a simple layer-over-a-halfspace model. Figure 26 shows the corresponding GPR traces recorded both on the free surface and in a second borehole. Concurrent analysis of both snapshots and traces facilitates identification of each arrival in the data, and gives feedback on what changes need to be made to the model to produce better fits of the synthetics to the real observations. This is therefore, an iterative process. The figures below show some of our current results; these will be improved in subsequent iterations.

Representative Field Data Examples

Figure 27 shows a preliminary model for a vertical slice containing boreholes A and D (see Fig. 6). This model is able to predict most of the main features seen in the GPR data recorded both on the surface and between the boreholes (Figs. 28, 29 and 31). Further adjustments (especially of the conductivity values, which control the attenuation) will improve the fit.

Figure 28 contains a comparison of real and synthetic 100 MHz data for a constant-offset (3 m) 2-D survey line from borehole A to borehole D. All the main arrivals, and even some of the details of the interference patterns are predicted. Figure 29 contains comparisons of field and synthetic data for two borehole recording configurations for the same model. Figures 29a and 29b are constant-depth cross-hole profiles, in which each trace is recorded with the transmitter and receiver antennas at the same depth (one in each hole). The depth increment between traces is 0.25 m. Figures 29c and 29d are for a vertical profile, for which the transmitter is fixed at the top of a hole, and each trace is recorded with the receiver at a different depth (with 0.25 m spacing) in the same hole. The velocity estimates from the constant-depth and vertical profiles are shown in Figure 30; the velocities from the former (with horizontal propagation and vertical polarization) are consistently smaller than those for the latter (with vertical propagation and horizontal polarization). Thus we have evidence for significant (15-20%) velocity anisotropy. Figure 31 contains real and synthetic data for a representative tomographic scan produced by fixing one antenna in hole A and moving the other antenna across the surface between the holes, and down hole D.

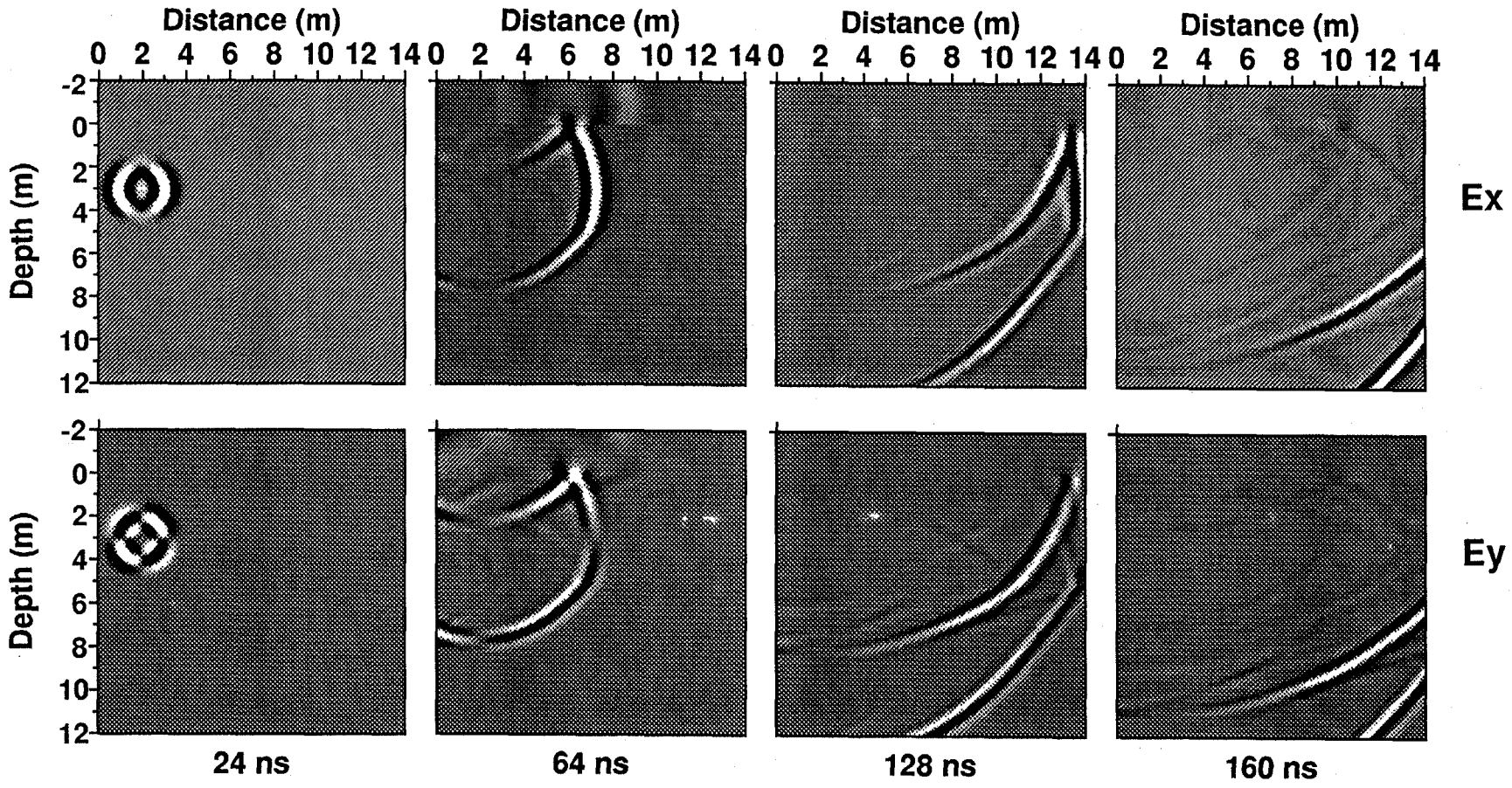

Figure 25: Snapshots of vertical (Ex) and transverse horizontal (Ey) polarizations of propagating electrical waves. The source dipole is at 3 m depth. The free surface is at 0 m depth. A single flat reflector is at 5 m depth. Corresponding GPR traces for surface and borehole recording arrays are shown in Fig. 26.

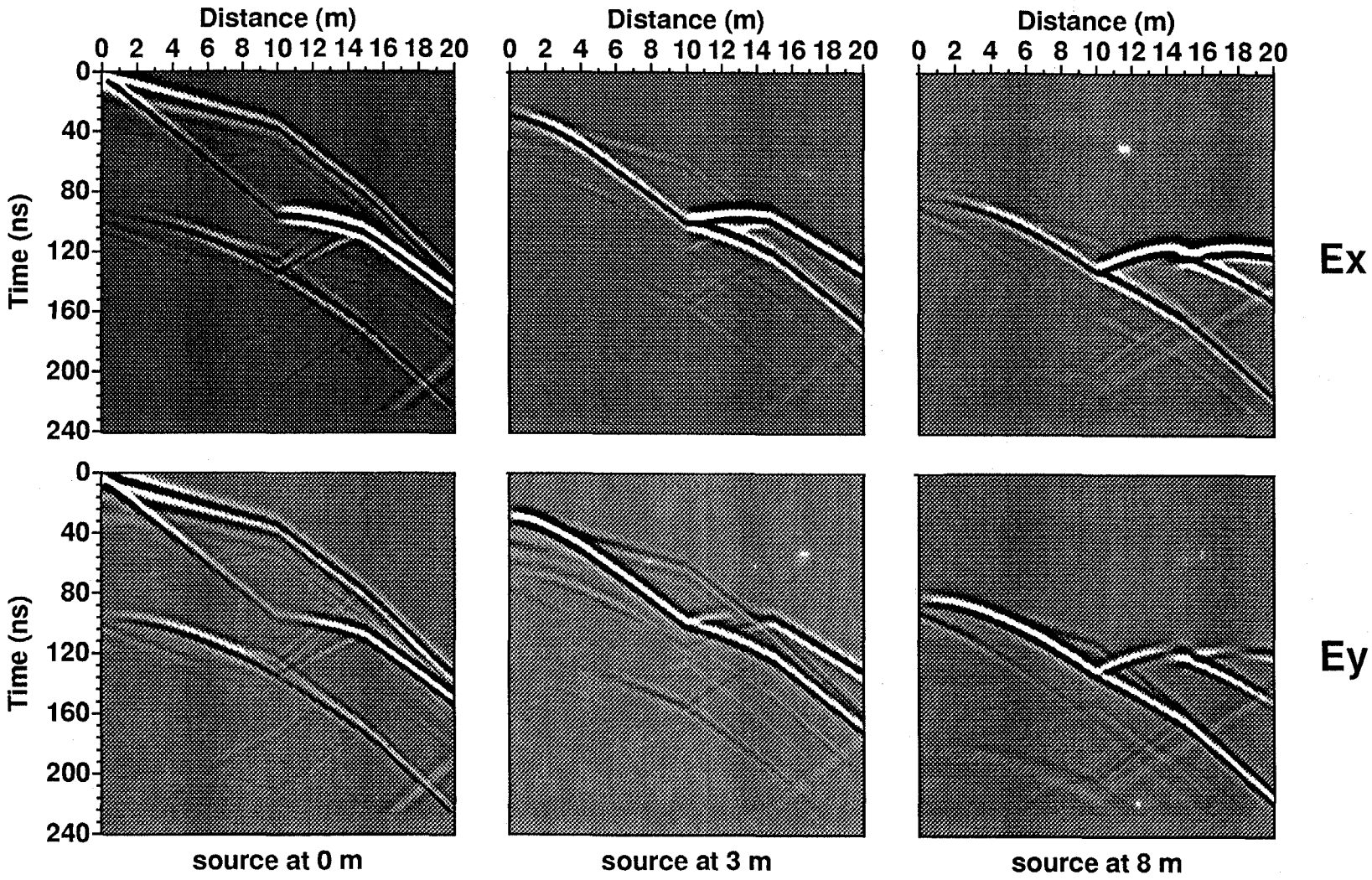

Figure 26: Synthetic GPR data for dipoles at three depths in a borehole. In each, the traces plotted between distances of 0 and 10 meters are recorded on the free surface, and those between 10 and 20 meters are recorded from 0 to 10 meters depth in a second borehole.

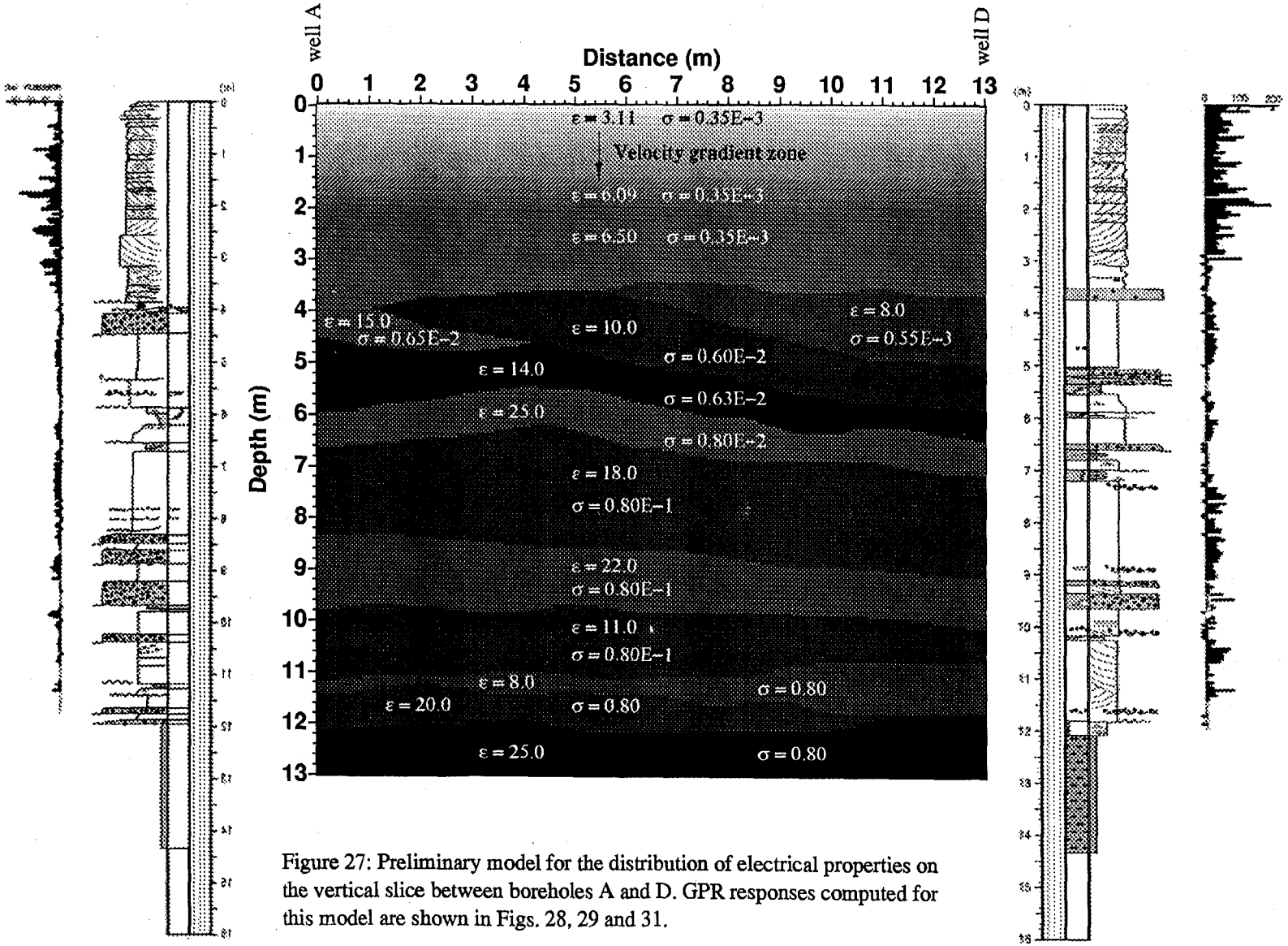

Figure 27: Preliminary model for the distribution of electrical properties on the vertical slice between boreholes A and D. GPR responses computed for this model are shown in Figs. 28, 29 and 31.

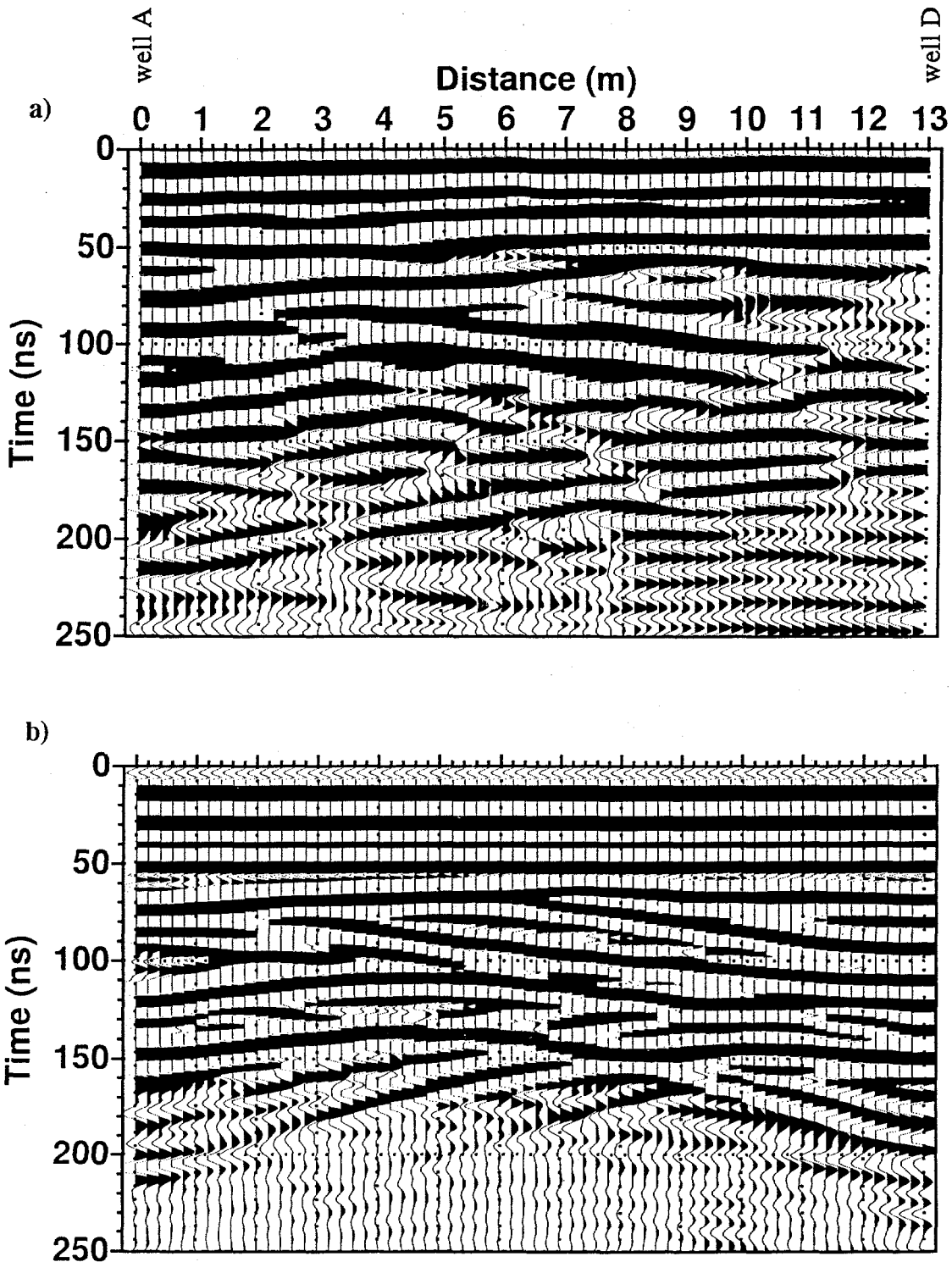

Figure 28: Real (a) and synthetic (b) data for the 2-D line between boreholes A and D. (b) is computed for the model in Fig. 27. Both are for a dominant frequency of 100 MHz and antenna separation of 3 m.

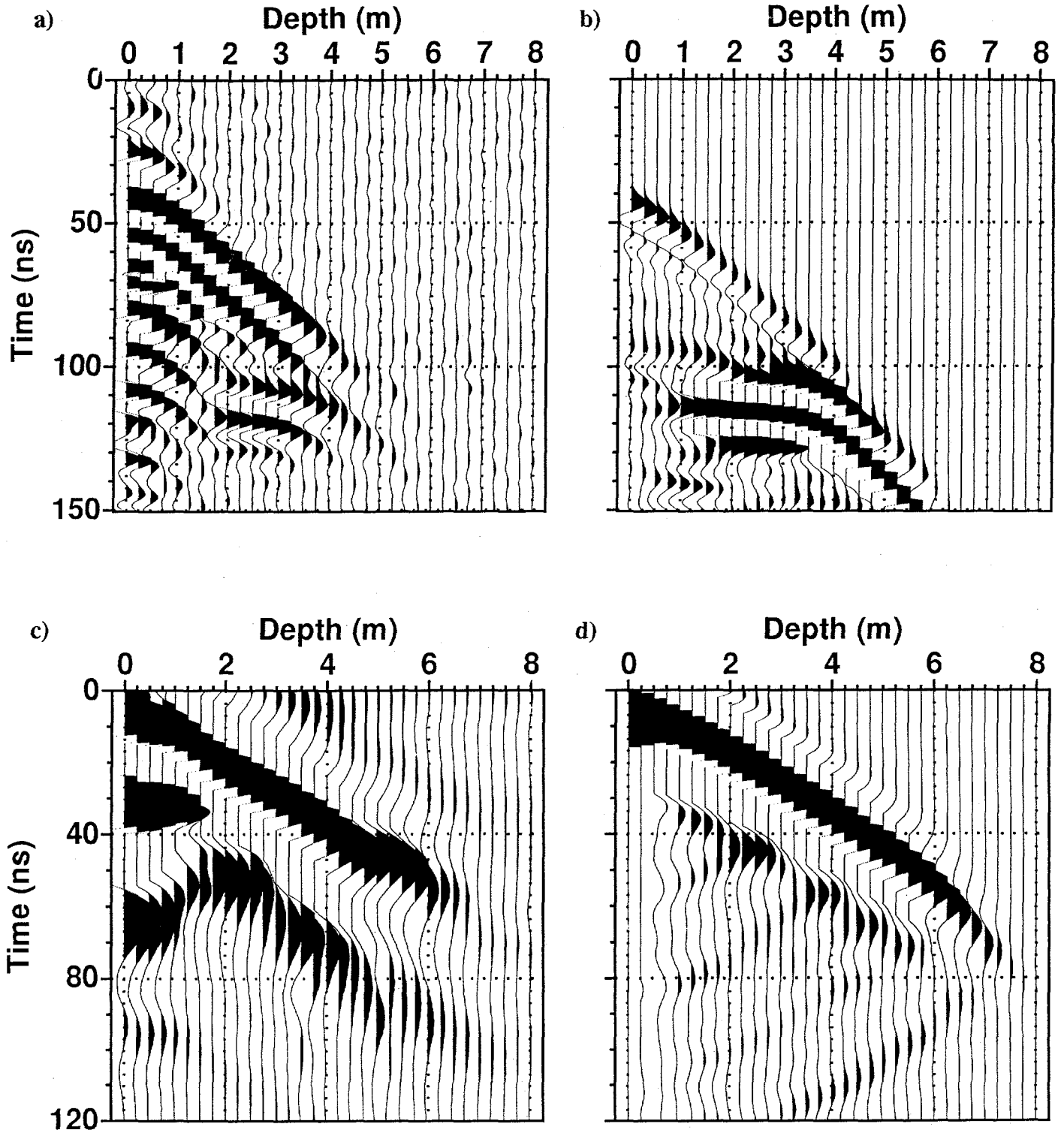

Figure 29: (a) and (b) are the real and synthetic data for a constant-depth cross-hole profile between boreholes A and D. (c) and (d) are the real and synthetic data for a vertical profile in borehole D. Both profiles are at 100 Mhz.

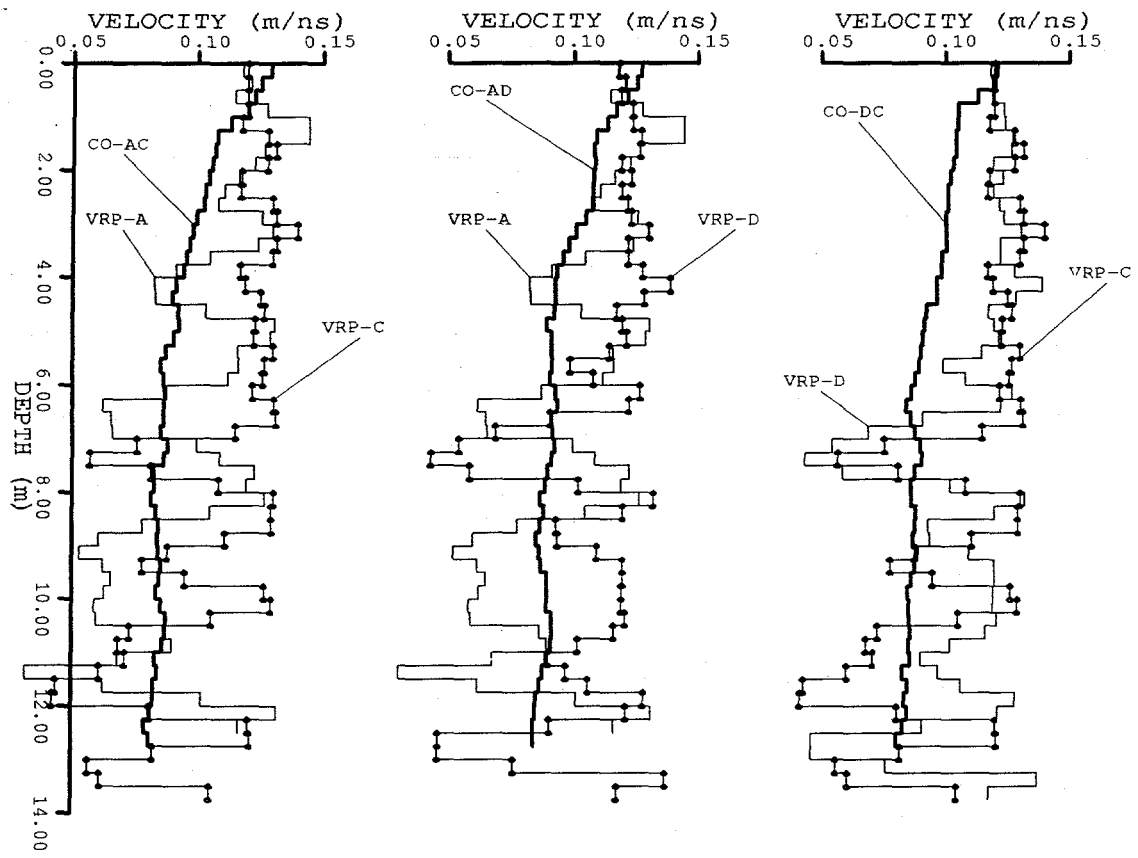

Figure 30: Velocity estimations from borehole GPR data. The left panel is from boreholes A and C; the center, from A and D; and the right, from D and C. In each, the heavy line (labelled CO) is the velocity profile from the constant-depth measurements between two holes, and the light lines (labelled VRP) are velocity profiles from vertical radar measurements in each of the two holes. A general decrease of velocity is seen with depth, as well as anisotropy between the vertical and horizontal polarizations.

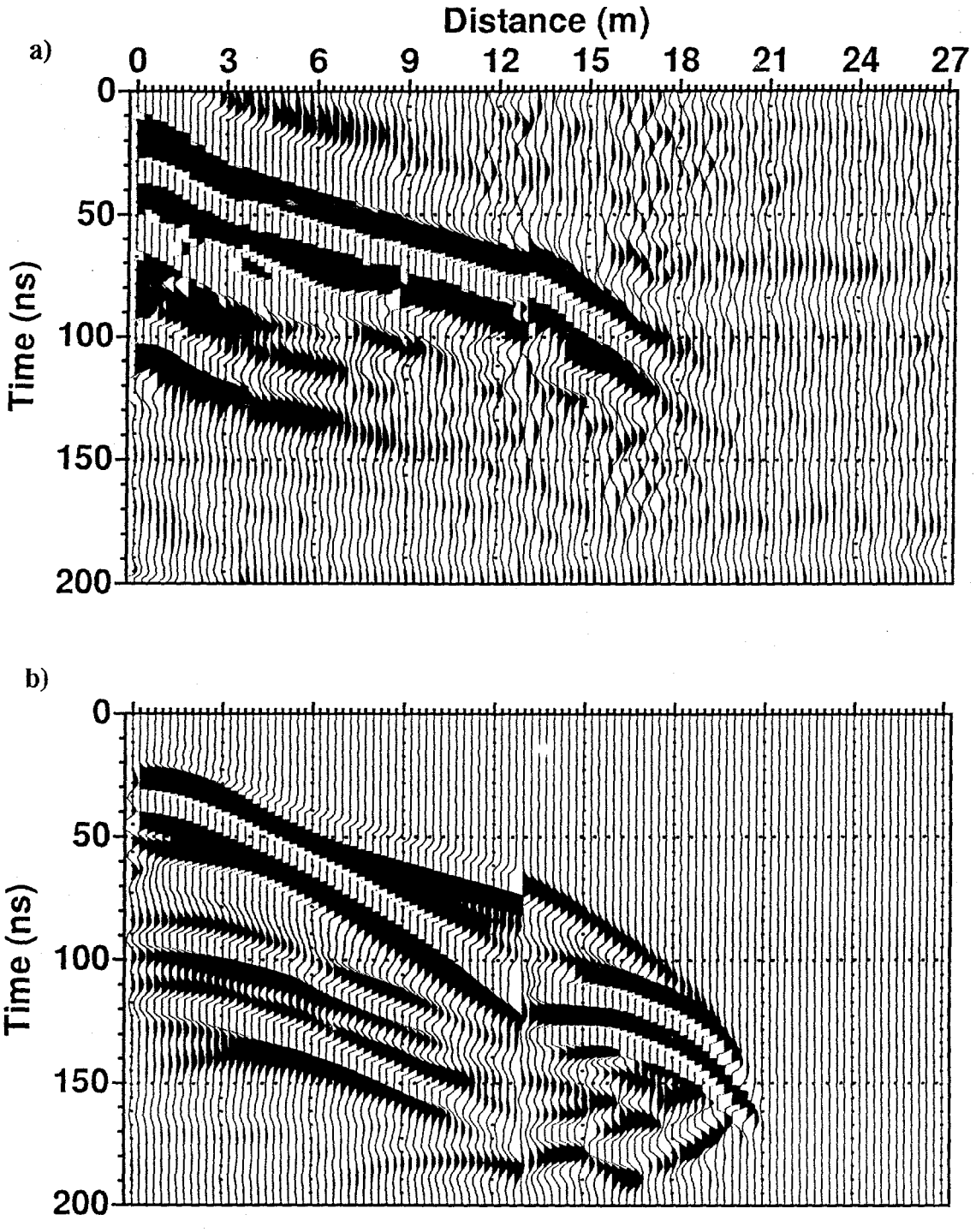

Figure 31: Real (a) and synthetic (b) 100 MHz GPR data for a tomographic scan. (b) is computed for the model in Fig. 27. The transmitter is at 3.5 m depth in borehole A; the receiver is moved from the top of this hole along the surface to borehole D (0.0 - 12.8 m) and then down the hole D (12.8 - 27.0 m).

RESERVOIR CHARACTERIZATION

Rucsandra Corbeanu, Kristian Soegaard and John B. Thurmond

The 3-D GPR data provide continuous information about rock properties throughout the survey volume. Since reservoir properties are related directly to primary sedimentary features it is imperative that the GPR data are interpreted in the context of the sedimentary geology at Coyote Basin. The full spectrum of sedimentary data outlined in the site description are used as a guide for the geophysical interpretation.

Sedimentology and Stratigraphy of Coyote Basin GPR Site

The facies map in Figure 7 concentrates exclusively on the fluvial sandstone complex in the upper 12 meters of the survey volume. The sandstone is composed of several architectural elements referred to as Units 1 through 5 in ascending stratigraphic order (Fig. 7). These architectural elements, or units, are separated by higher-order bounding surfaces labelled A through E in ascending order (Fig. 7). Units 1 through 4 are separated by surfaces B, C and D. In the lower ~7 m of the channel complex, the four units consist of fine-grained lenticular sandstone bodies which pinch out over distances of several 10's of meters parallel to the cliff face in the direction of the channel axis. Internally, these architectural elements consist of low-angle, parallel-laminated sandstone which scour into underlying similar parallel-laminated sandstone. The base of Units 1 through 4 are erosional and commonly have mudstone intraclast conglomerate along the basal scour (Fig. 8 and Appendix A). The upper part of Units 1 through 4 are capped by a 5 to 10 cm thick mudstone layer which is laterally discontinuous due to truncation by the overlying unit. Units 1 through 4 are interpreted as scour and fill elements deposited during flood events within a fluvial channel.

Unit 5 in the uppermost 4.5 to 5.5 meters of the channel sandstone consists exclusively of medium- to large-scale, trough-cross bedded, medium-grained sandstone. This trough cross-bedded unit is lenticular in geometry with a relatively flat, although erosional base, and an upward-convex upper surface (Fig. 9). This lower surface is bounding surface E in Figure 7. Unit 5 is traced more than 640 m to the south in a down-current direction before pinching out. The upcurrent, northward extent of the trough cross-bedded unit 5 has not been determined north of the survey site. Trough cross beds in the up-current position at Coyote Basin are clearly climbing with coset surfaces truncating against the lower surface E upcurrent and the upper surface in a down-current direction (Figs. 7 and 9). In the down-current portion of unit 5 south of the survey area, trough cross-bed coset surfaces truncate against the lower surface in a down-current direction (Fig. 9).

In the lower half of unit 5 trough cross beds are thicker, with a greater proportion of the cross beds being preserved (between 10 to 30 cm in thickness). Trough cross beds tend to be less than 10 cm thick in the upper part of unit 5 due to scouring by overlying cross beds (Fig. 32). On the upper surface of the survey site, trough cross beds are about 0.5 to 1.5 meters wide and extend in a down-current direction for a distance of 1 to 7 meters (Fig. 6). Along the cliff face, similar lateral extent of several meters are seen for the cross beds (Fig. 32).

Unit 5 is interpreted to be a channel bar-form in which cosets of trough cross beds outline the geometry of the upper surface of the barform. The survey site at Coyote Basin is in the up-current portion of the barform on the northwestern western side of the channel bar (Fig. 9). The upward climb of cross-bed cosets in the upcurrent portion of the barform implies that sedimentation rates were high and that bar accretion occurred both in an up-current and down-current direction. More commonly, barforms tend to experience erosion up-current with bar growth in a down-current direction (Bridge, 1986; Miall and Turner-Peterson, 1989). In these instances cross bed cosets truncate the upper surface of barforms in an up-current direction.

GPR Interpretation of Coyote Basin Site

Integration of the 3-D GPR data set with sedimentological and stratigraphic data at Coyote Basin has provided information regarding lateral development of the architectural elements in the third dimension inside the fluvial deposits.

The Environment of GPR Interpretation

Two different types of GPR data are available for mapping the major surfaces inside survey volume at Coyote Basin. These data include the three 2-D GPR profiles between wells A and C, A and D, and C and D, and the three 3-D GPR volumes acquired at 50, 100, and 200 MHz. Both types of GPR data are depth migrated. Figure 33 illustrates the relation between GPR reflectors and the lithologic columns and permeability curves of each well for the 2-D profile between wells A and C.

The 3-D GPR volumes each consist of thirty-four 2-D lines running from south to north with a half meter spacing. These survey lines are in the long dimension of the grid and parallel to the cliff face (Fig. 34).

Since ground-penetrating radar data in many respects are similar to data produced by seismic reflection techniques used in the oil and gas industry, the display and interpretation methods employed in seismic exploration can be applied directly to the GPR data with little modification. Modern interactive workstations used for seismic interpretation provided a rapid, flexible means for interpreting 3-D GPR data sets. The automatic horizon tracking facilities on

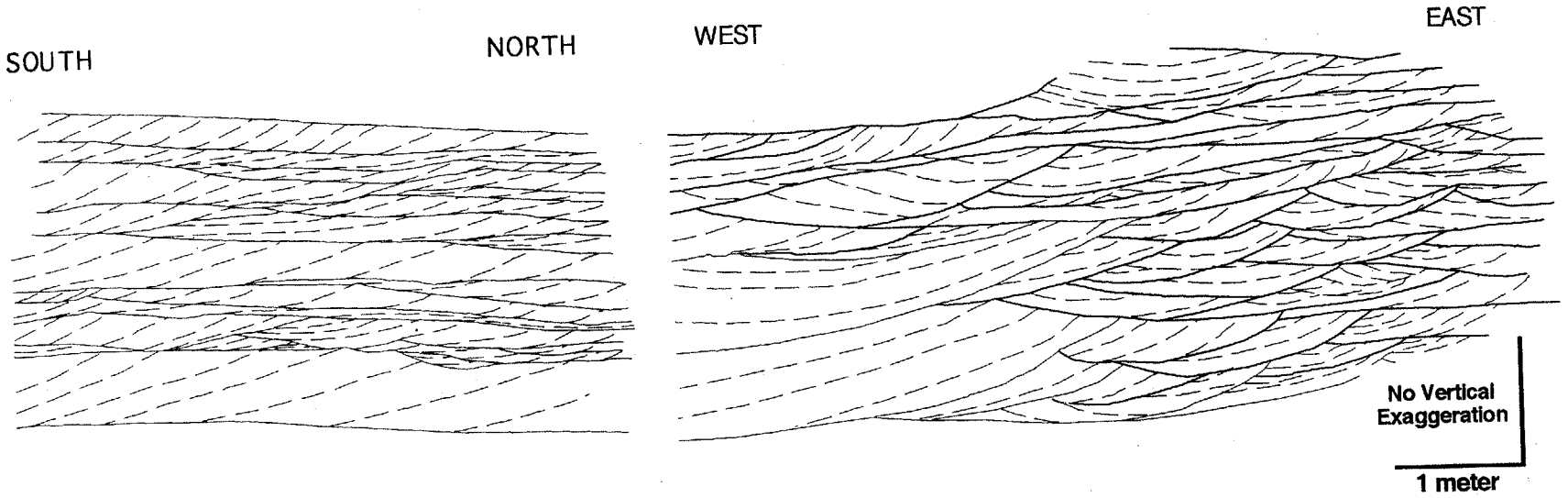

Figure 32: Detailed outcrop map of trough cross beds in unit 5 immediately southeast of the GPR survey area (Fig. 6). North-South panel shows geometry of trough cross beds parallel to flow direction whereas East-West panel is perpendicular to flow. Note that cross bed sets become thinner upwards.

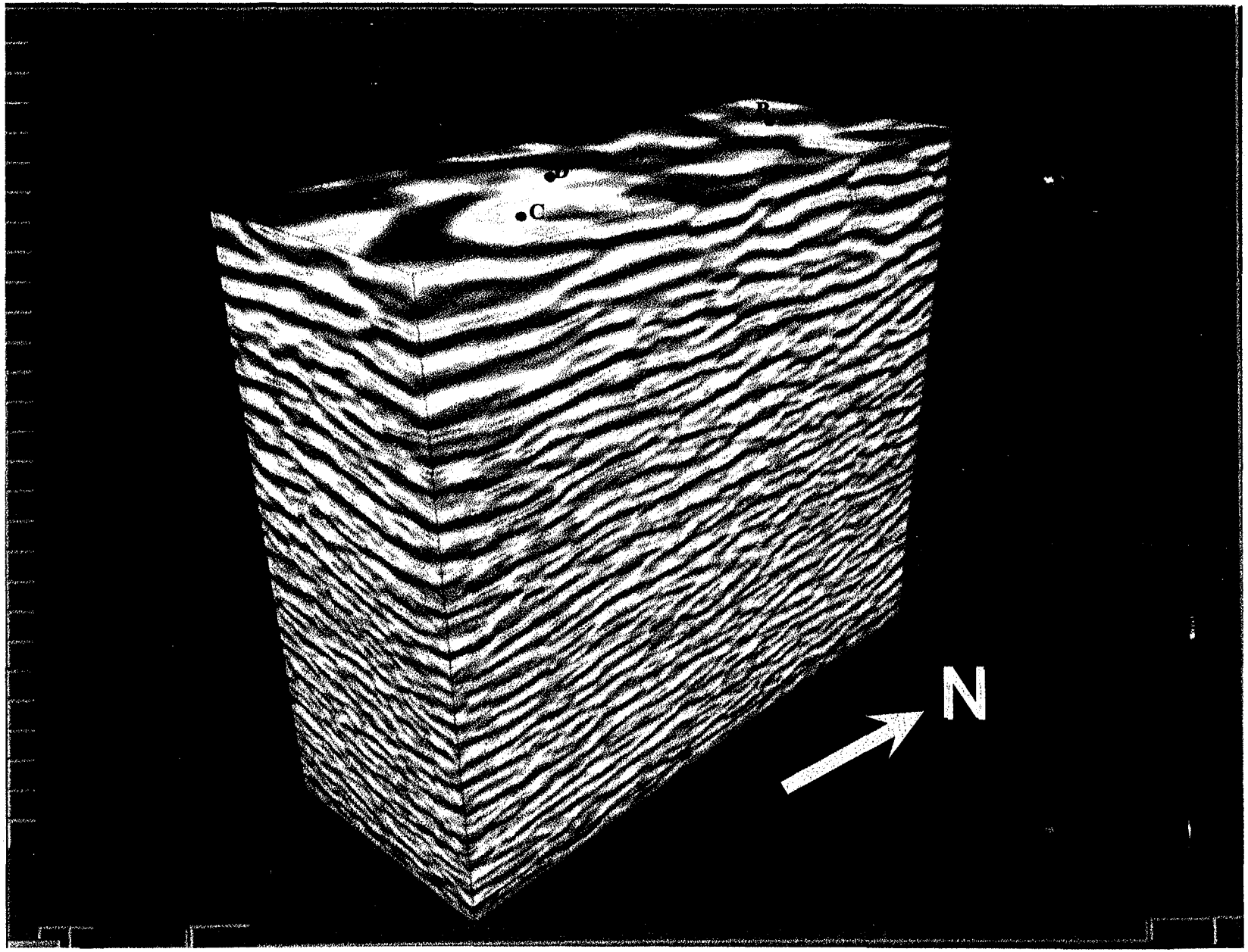

Figure 34: 3-D GPR volume consisting of thirty-four 2-D lines running from south to north; in Figure 6 the 3-D grid is defined with red crosses. Well C is close to the line nearest the cliff face. The data cube is displayed on a GeoQuest workstation at ARCO Oil and Gas Company where all GPR interpretation has been performed.

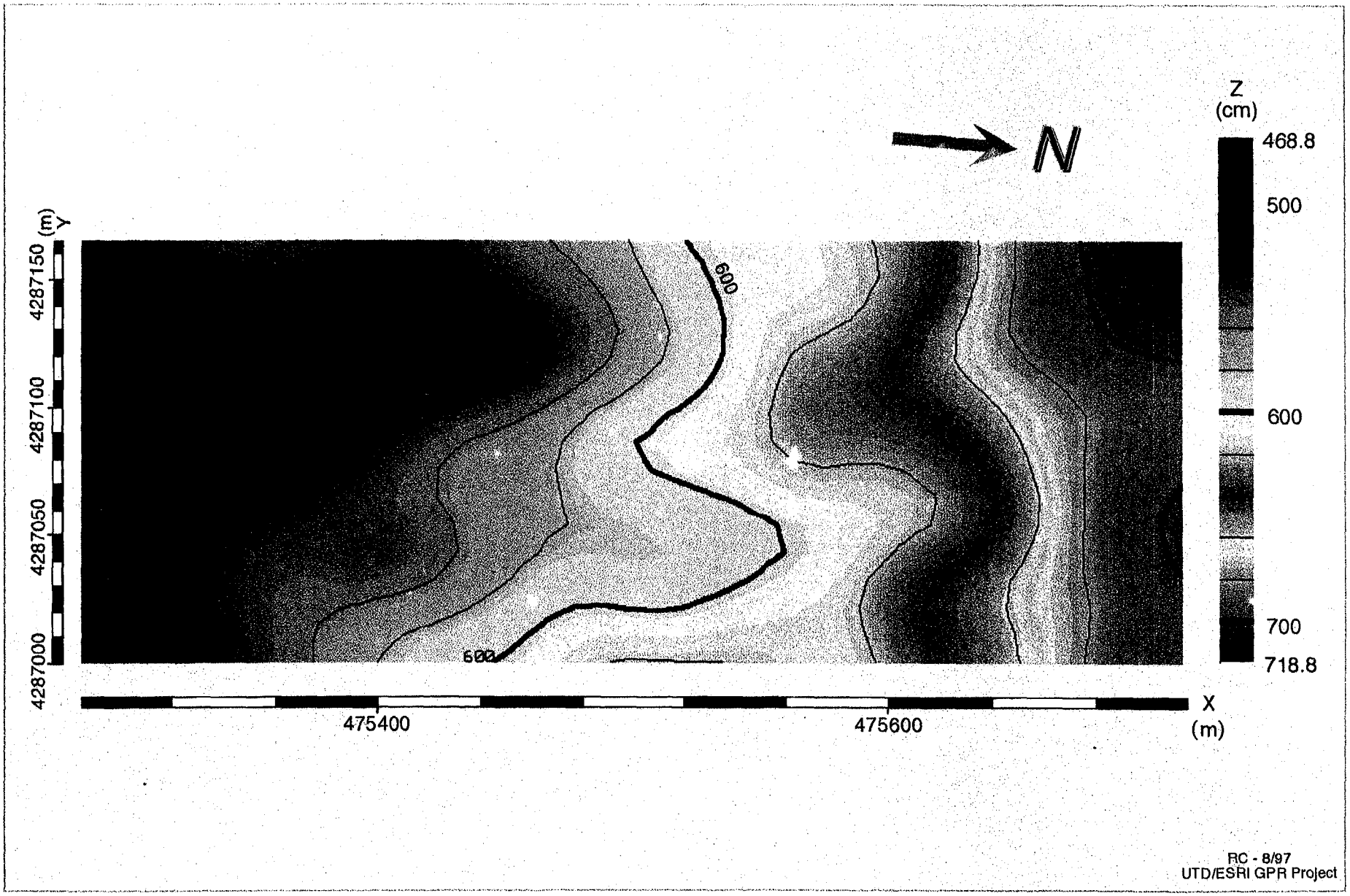

Figure 35: Contour map of the base of the cross-bedded sandstone unit. The map is generated from the 3-D GPR data set using GeoQuest workstation. The depth scale is in cm.

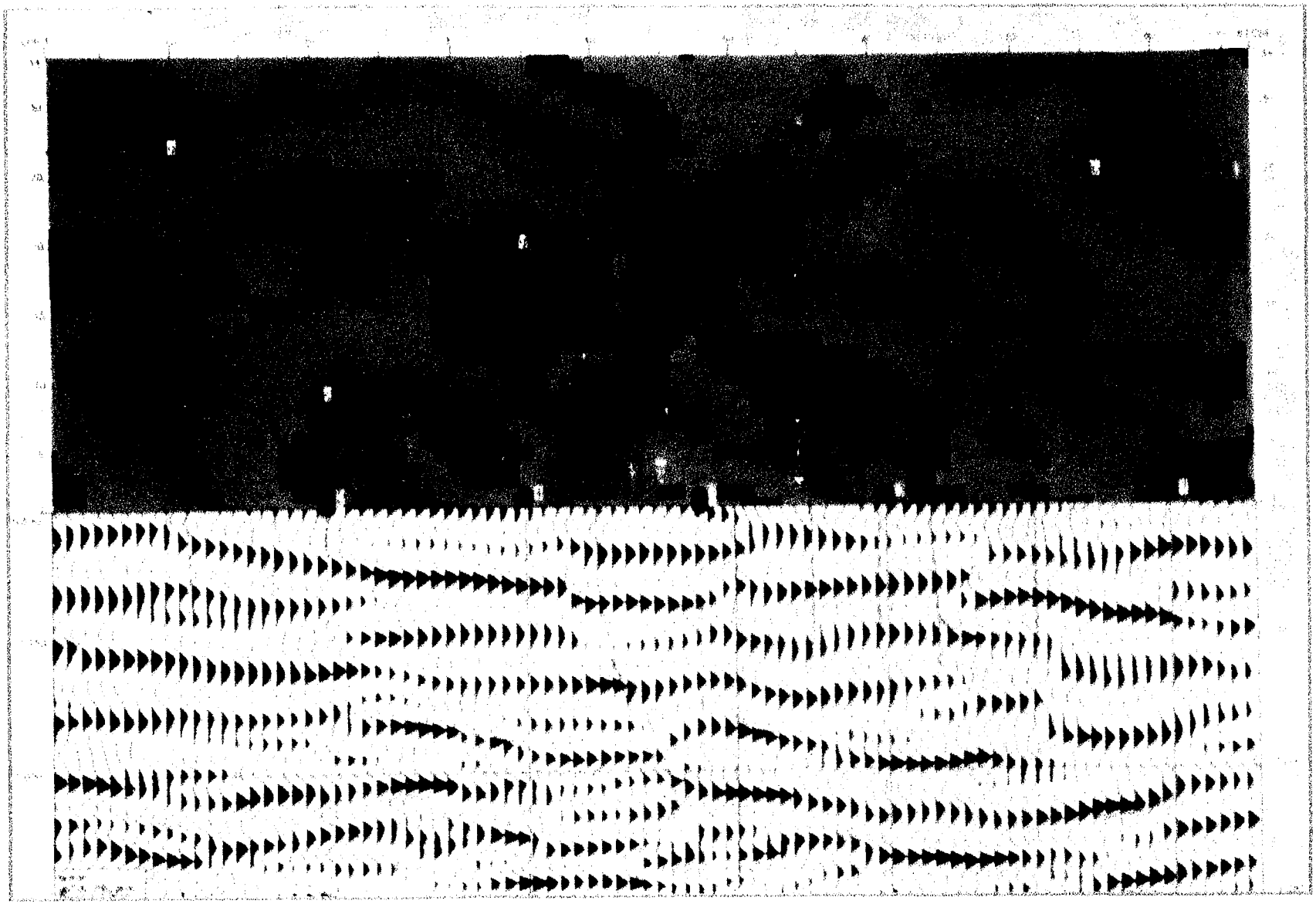

Figure 36: A horizontal slice 60 cm thick, cut at 5 m depth showing the general trend of a GPR trough event corresponding with surface E. The map portrays the continuity of a given event, in this case a trough event, corresponding to the base of the trough cross-bedded sandstone unit. The black areas within the horizontal slice map portray regions in which GPR reflectors are discontinuous and cannot be correlated with certainty. Truncation of GPR reflectors appear to be related to fracture sets mapped at the surface in Figure 6 and shown in the map above as red dots.

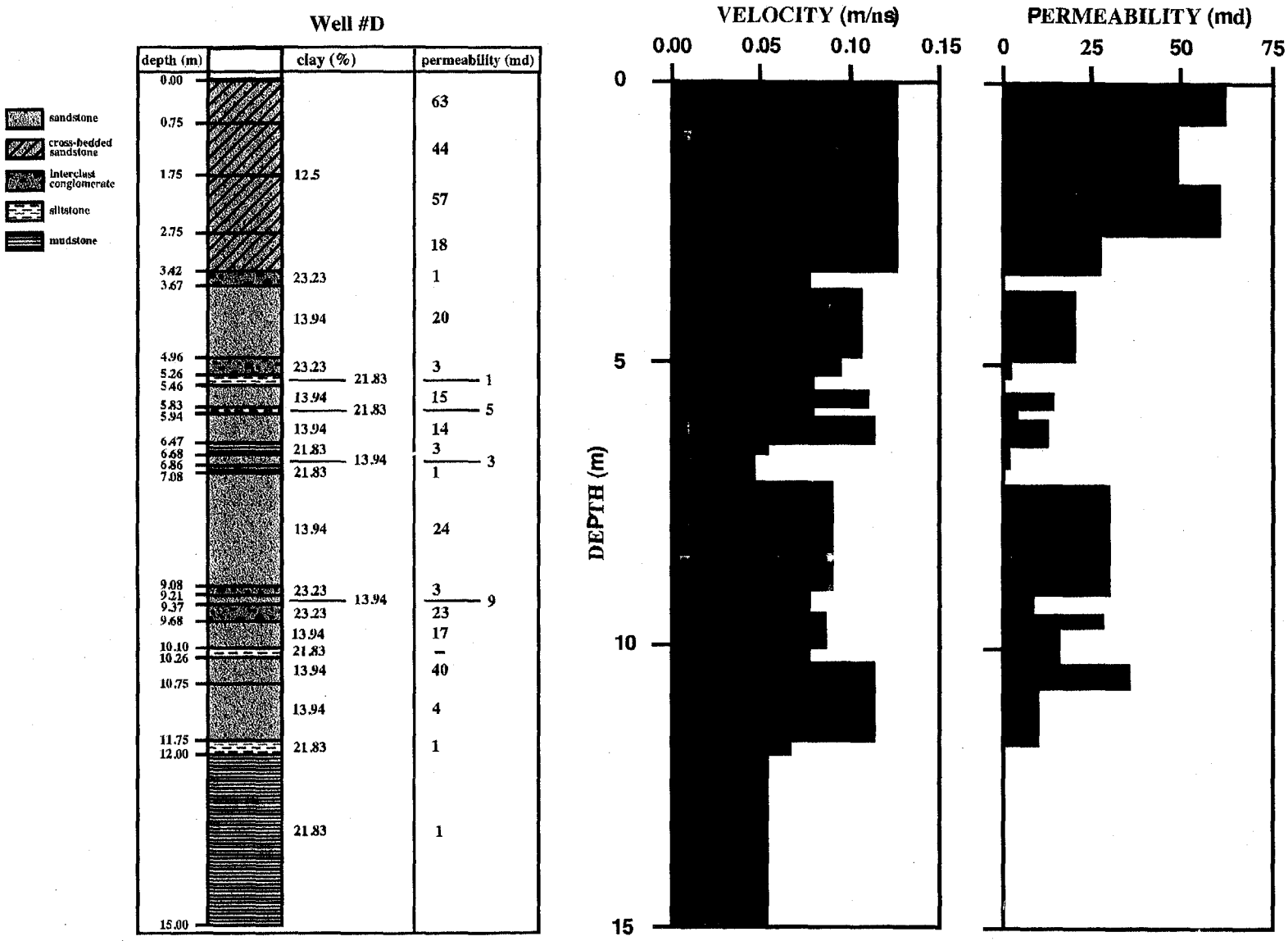

Figure 37: Model parameterization used in constructing the synthetic radargram in Figure 38. The synthetic radargram is based upon a) Lithology, clay/sand, and permeability, b) interval GPR velocity, c) interval permeability.

Permeability data were obtained from a minipermeameter log of the core with a sampling interval of 5 cm. Permeability for each unit was computed by averaging values within the corresponding depth interval. The same procedure was used for computing the clay content in each unit. The percentage of clay was measured from petrographic microscope counts in thin sections selected from samples in the core (performed by Laura Crossey and Karen Roche at the University of New Mexico). Occasionally, the clay content was not representative of a complete interval since there may be only a few samples measured in that interval.

Electrical property parameterization of the model was derived from measurements of the dielectric permittivity of samples in the core. These values are a function of lithology, permeability and water content. Initial estimates of the GPR velocity were obtained from effective medium mixing models. A 2.5-D finite-difference algorithm was used to simulate GPR data from the model. Final velocities at the well were obtained by iterative adjustment of the GPR model. A synthetic radargram at the well has satisfactorily matched reflection polarity, frequency content, and primary and multiple events of the 3-D data (Fig. 38). The synthetic radargram allows identification of meaningful boundaries in the lithologic column with its corresponding GPR reflection.

GPR Interpretation at Varying Frequencies

Two important aspects are expected from a GPR survey: adequate vertical resolution and depth of penetration. Both depend mainly on electrical properties of the subsurface material and on the recording parameters of the equipment.

The 3-D GPR data sets were collected at three different frequencies of 50 MHz, 100 MHz, and 200 MHz. The relationship between frequency and depth of penetration and resolution in a GPR survey can be seen by comparing Figures 39, 40 and 41. Figures 39A and B show inline 9 through well C from the 3-D 100 MHz data set, both uninterpreted and interpreted. Interpretation of the 3-D sets was carried out mainly on 100 MHz data where vertical resolution is about a half meter and depth of penetration is about 15 meters. The interpretation shows the general trend of major surfaces defined at the outcrop in Figure 7. The lithologic column and permeability profile for Well C are superimposed on the GPR data to illustrate the relationship between the GPR reflectors and the thickness of strata resolved by the GPR.

For a comparison of vertical resolution, Figures 40 and 41 show the same line from the 50 MHz and 200 MHz data sets, respectively. The 50 MHz profile cannot resolve details of the complex architecture of the deposits; for example, thin conglomerate beds at 10 m depth are not resolved (Fig. 40).

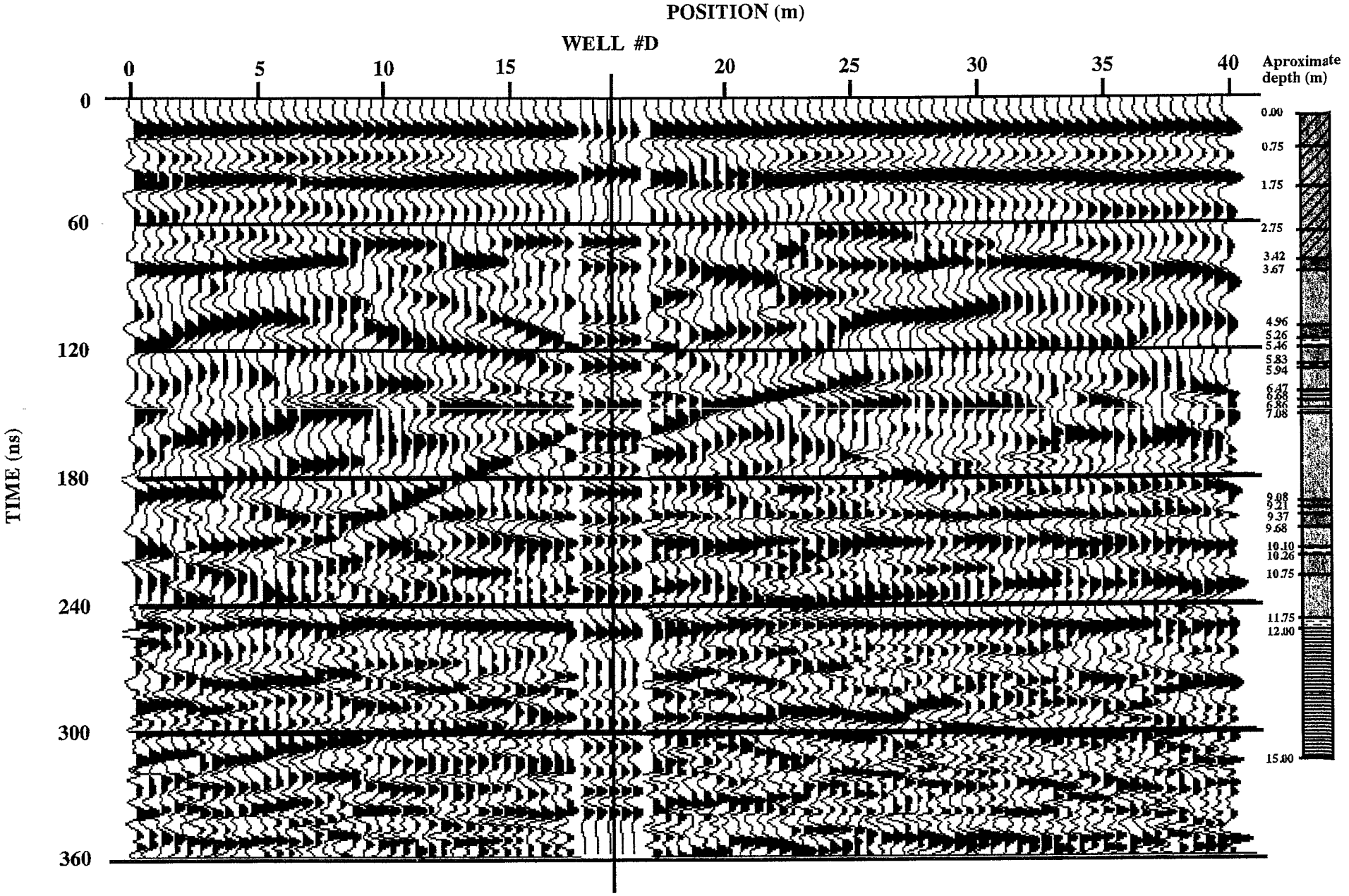

Figure 38: 3-D GPR time section with simulated GPR data at borehole #D. The five radar traces at Well D are identical and are based on the velocity model in Figure 37. The GPR line is in-line 20 which extends north-south through Well D. Energy below 12 m depth are internal multiples. Lithology is the same as in Figure 37.

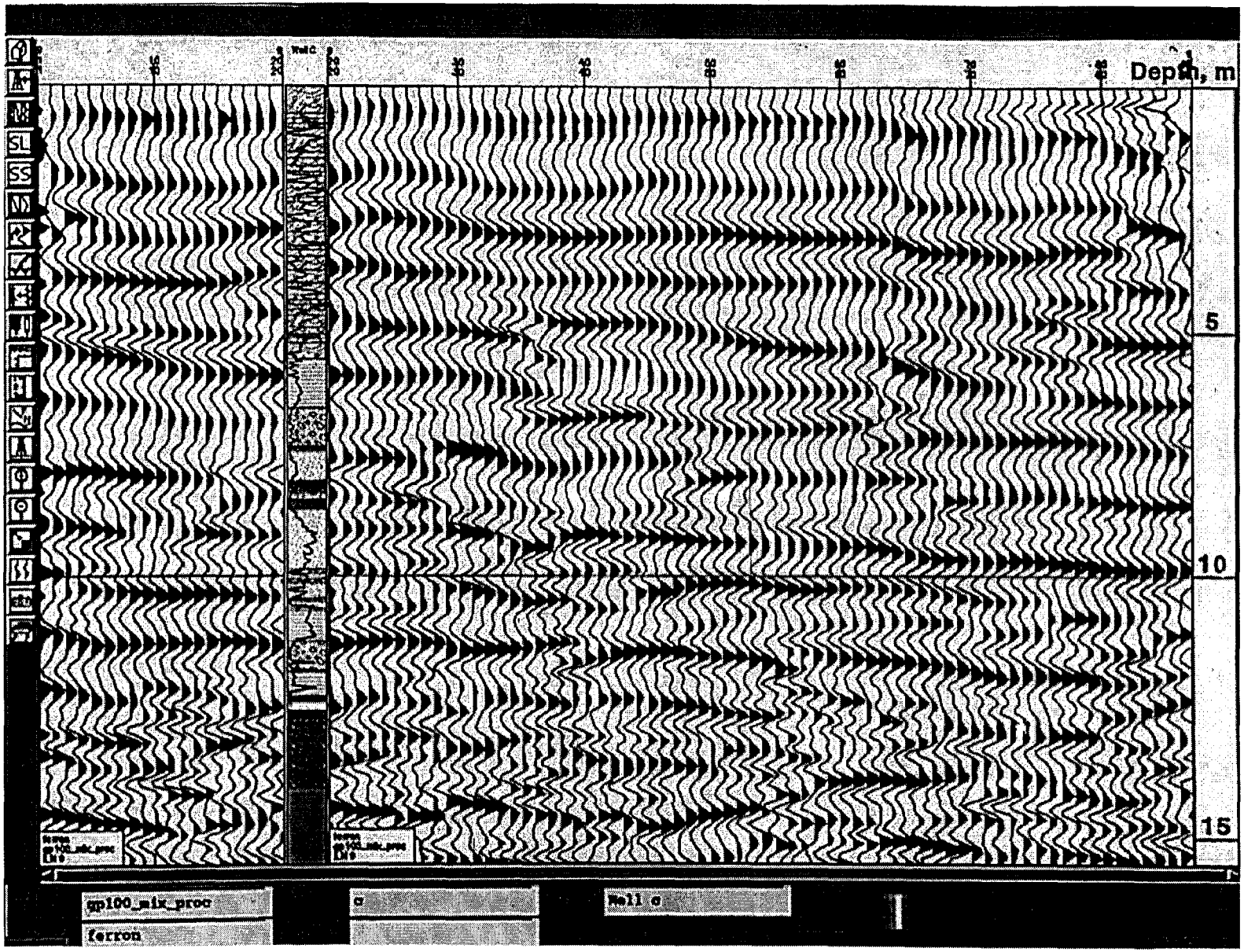

Figure 39A: Uninterpreted in-line GPR profile from the 100 MHz data set through Well C. The lithologic column and permeability curve for Well C are shown for correlation with GPR reflectors. See Figure 39B for interpretation of profile.

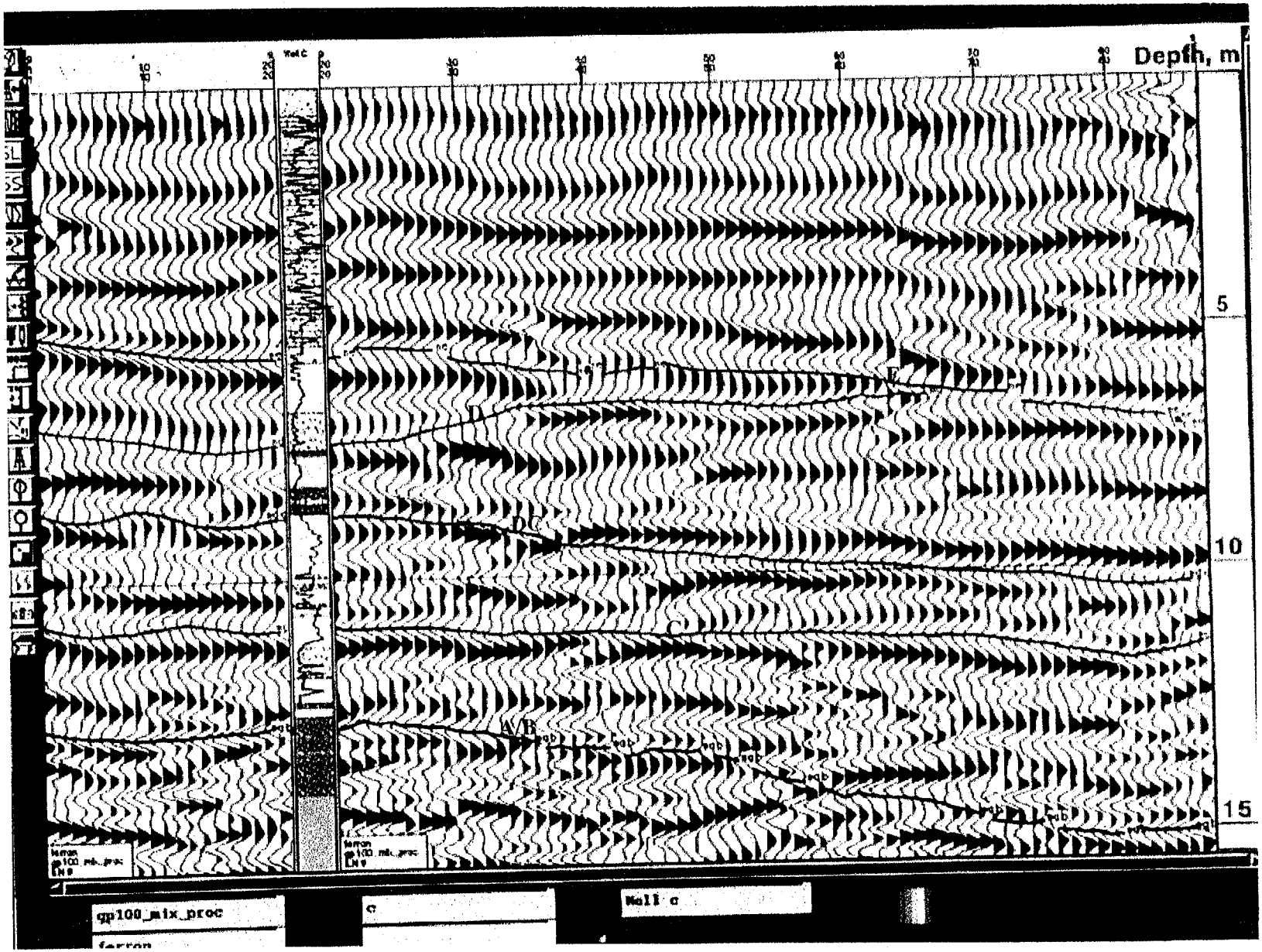

Figure 39B: Interpreted 100 MHz in-line GPR profile illustrated in Figure 39A.

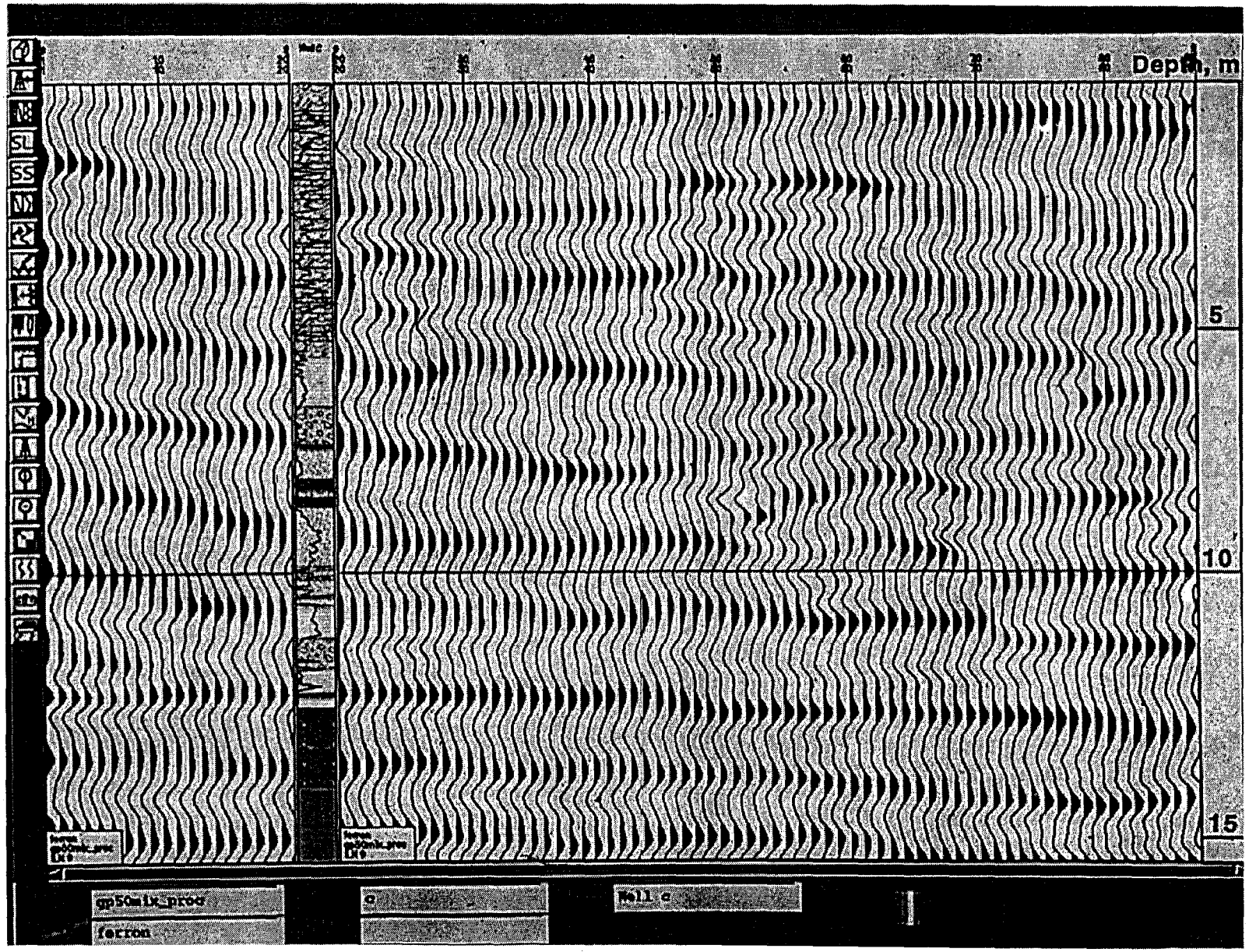

Figure 40: Uninterpreted in-line GPR profile from the 50 MHz data set through Well C. See Figure 39A for comparison. The 50 MHz data set only yields a vertical resolution of about one meter but has depth of penetration of approximately 25m.

In Figure 41, the same profile of inline 9 through Well C from the 200 MHz data set shows greater vertical resolution (about a quarter of a meter) and more detail. The thin intraclast conglomerate and shale beds at 10 meters depth are resolved by the GPR at this higher frequency. The direct relationship between lithology, permeability and the reflectors on the 200 MHz lines has not yet been determined at this time. However, these details make the 200 MHz data set more difficult to interpret than the lower frequency data away from the well constraints.

Preliminary GPR Interpretation of Major Bounding Surfaces

Preliminary interpretation of 3-D GPR data sets is based on geologic constraints at the outcrop and in the wells (Fig. 42). Figure 42A shows the uninterpreted GPR line nearest to the outcrop and the lithology columns of five "pseudo-wells" measured on the outcrop together with permeability curves for the sections. Although topographic effects have been removed from the data, reflectors in the upper 2.5 m consistently follow surface topography and are interpreted as a weathering effect. The GPR events show the major bounding surfaces picked in the outcrop. Surface E, at the base of the trough cross-bedded medium grained sandstone in Unit 5 at the outcrop in Figure 7, is identified as a continuous reflector in the interpreted line (Fig. 42B). Above surface E, the GPR reflectors show the climbing nature of trough cross-bed cosets similar to that seen at the outcrop. Surface D in Figure 42B is truncated to the right by surface E and again is similar to relationships seen at the outcrop (Fig. 7). Some reflectors below this surface are likewise truncated. In the lower part of the channel complex at Unit 2, poor exposure of the cliff face does not allow identification of some surfaces which, on the GPR, are continuous reflectors (for example reflector at 11 m depth in Figure 42B). Generally, units 4 and 5 are easier to map than the deeper-buried units 2 and 3, even at greater distances from the outcrop.

Another set of data used in constraining interpretation of the GPR data are the four wells within the survey area (Fig. 6). Figures 43A and B show the uninterpreted and interpreted traverse connecting the four wells extracted from the 100 MHz 3-D GPR volume. The lithologies and permeabilities are shown for each well to illustrate their relationship with the GPR reflectors. The same major surfaces identified at the outcrop can be followed through the four wells. Surface E is dipping toward north and the climbing cross-bed cosets are revealed by the reflectors above the E surface. Similarly, surface D pinches out against surface E near well B and truncates the reflectors below.

The sandstone-mudstone contact A/B at the base of the channel complex has a clear response in the GPR data with a continuous reflector at a depth of 12 meters. It should be

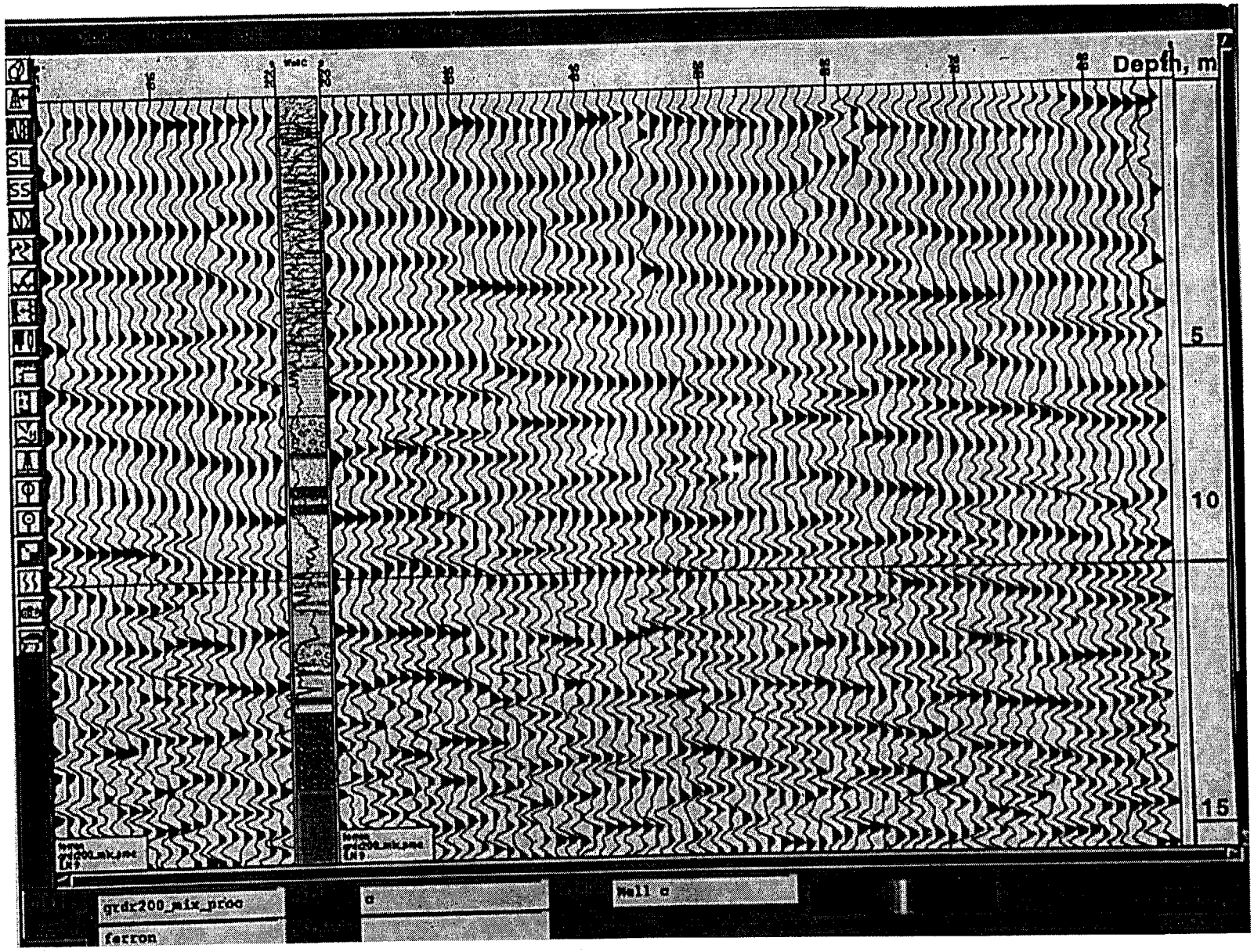

Figure 41: Uninterpreted in-line GPR profile from the 200 MHz data set through Well C. See Figures 39A and 40 for comparison. The 200 MHz data set yields higher resolution (vertical resolution of about 0.25m).

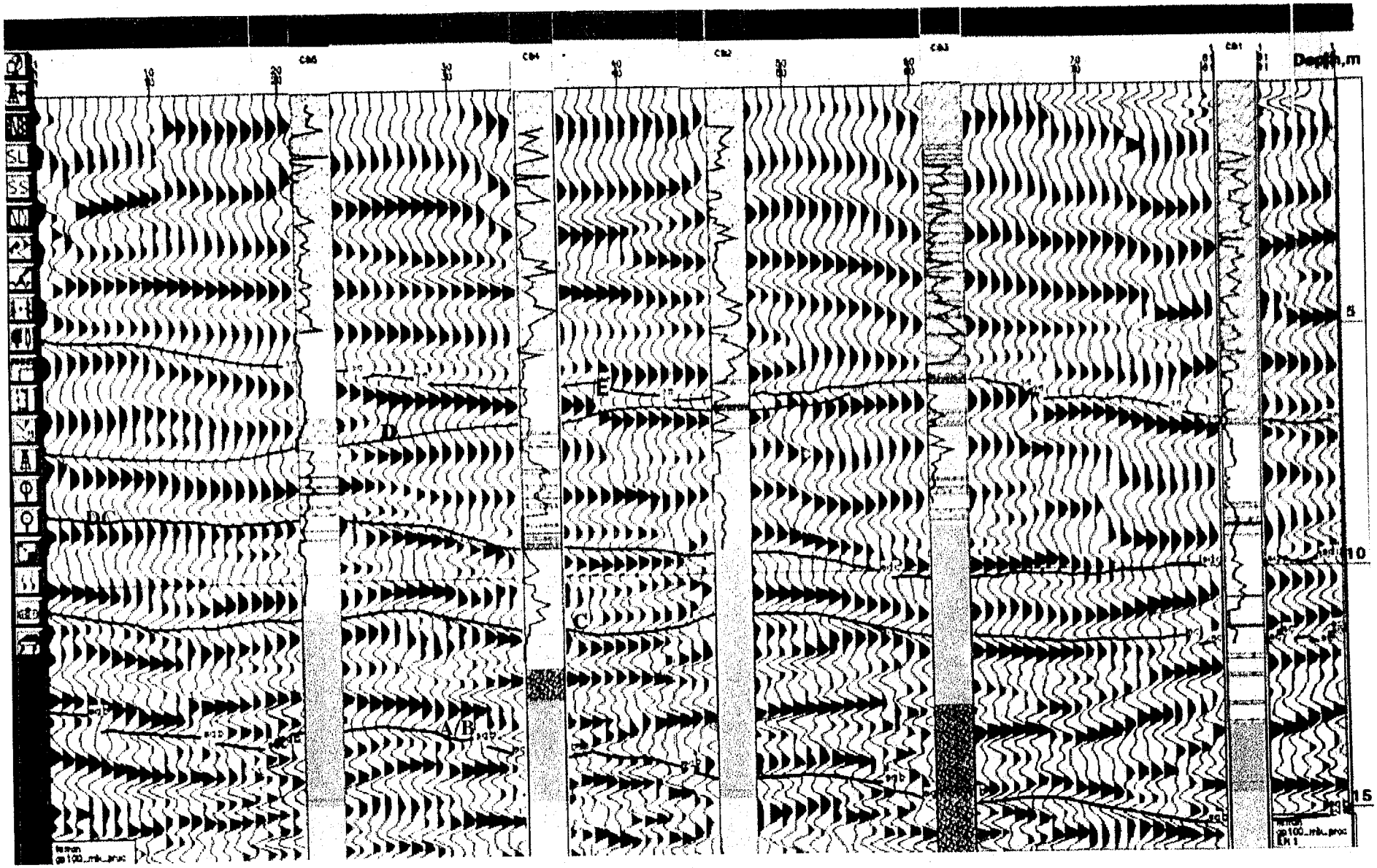

Figure 42B: Preliminary interpretation of the in-line GPR profile illustrated in Figure 42A.

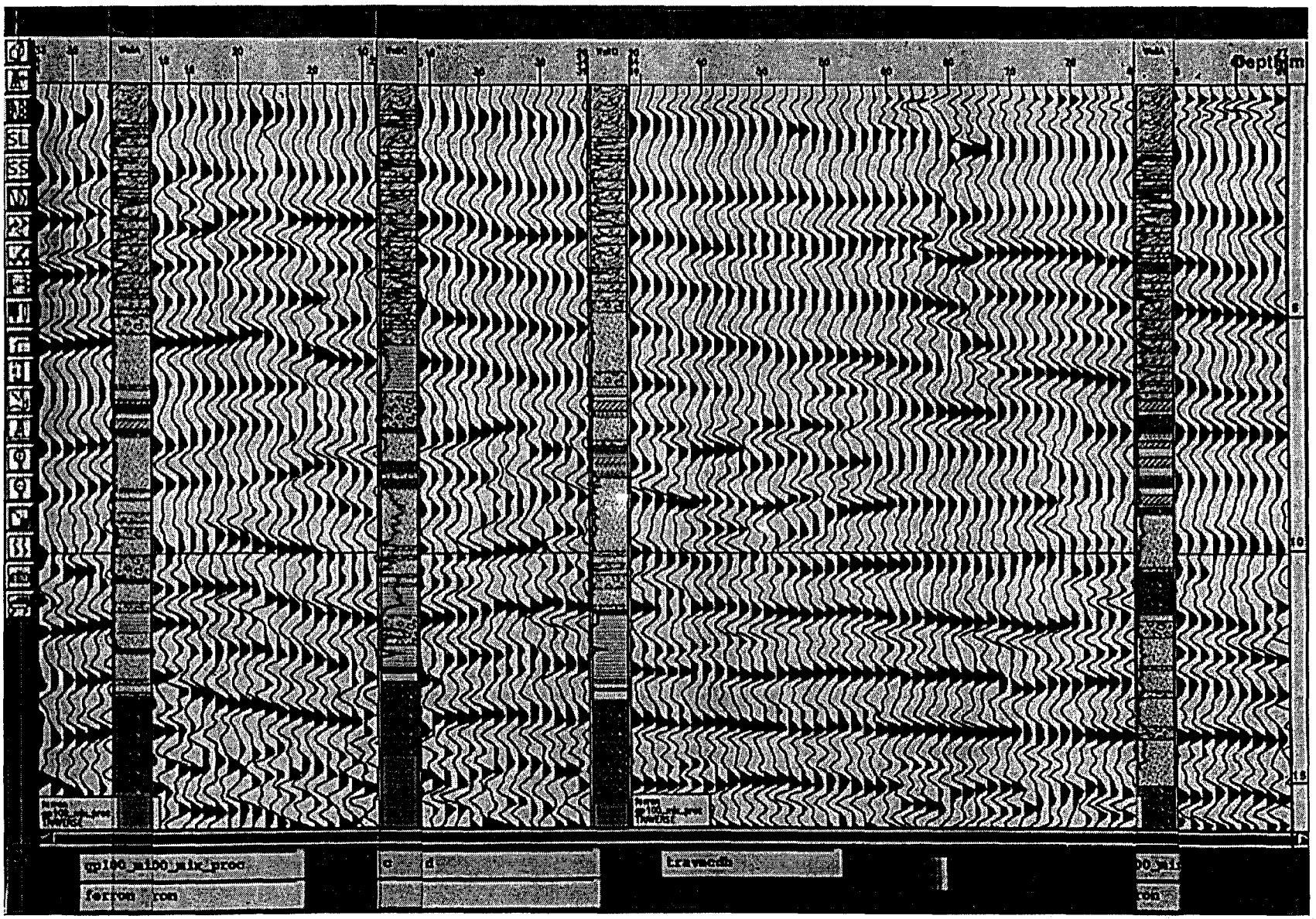

Figure 43A: Uninterpreted GPR profile traverse through Wells A, C, D, and B. See Figure 6 for location of profile location. Superimposed on the GPR profile are lithologic columns and permeability curves from the four wells. See Figure 43B for interpretation of profile.

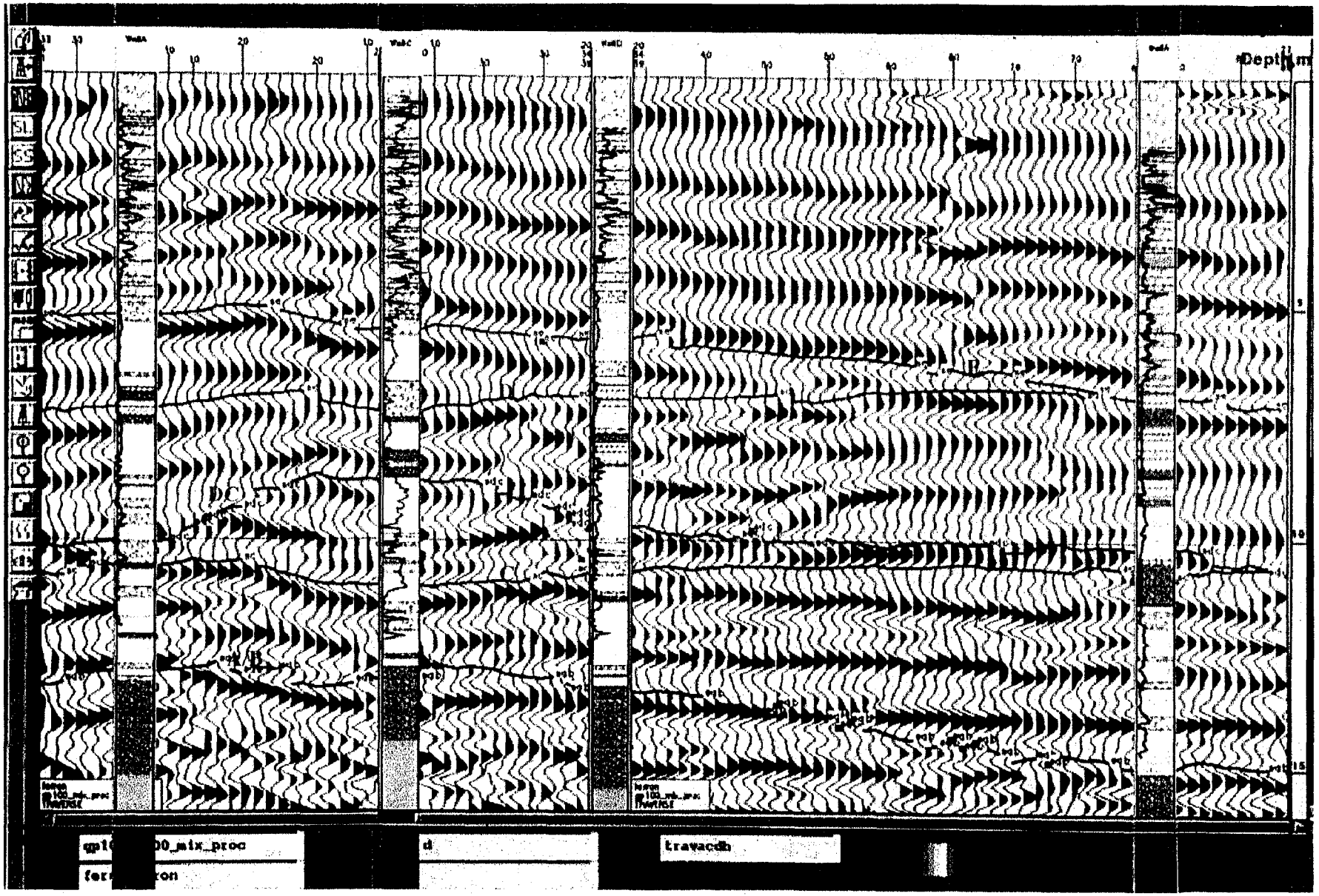

Figure 43B: Preliminary interpretion of the GPR profile illustrated in Figure 43A.

noted that the reflector corresponding with the base of the sandstone complex shows an obvious mistie in well B. This mistie is due to a poor velocity model for the depth migration in the northern part of the GPR survey volume. A new analysis of the velocity, plus 2-D GPR modeling, is now in progress to correct the misties.

Contour maps for all five surfaces outlining the five principal architectural elements in the fluvial sandstone at Coyote Basin are presented in Figure 44. These contour maps are generated from the 3-D GPR data sets on the GeoQuest workstation.

GPR Interpretation of Flow Barriers

Detailed mapping of the intraclast conglomerate and mudstone flow barriers have not yet been extended through the entire volume. Figures 45A and B contain uninterpreted and interpreted GPR profiles from the 3-D dataset for traverses through Wells A and C. Lithologic columns and permeability curves are shown as constraints for the interpretation. In general, variations in permeability corellate with changes in lithology. However, in certain instances, changes in permeabilities occur within lithofacies, and correspond with an observed GPR reflection. For example, the reflector in the GPR profile at 9 meters depth, near well C, is associated with an upward decrease in permeability within a massive fine-grained sandstone (Fig. 45B).

Intraclast conglomerate and mudstone layers tend to be discontinuous and are impossible to correlate even between closely spaced wells without the GPR data. This distribution of low permeability flow barriers is essential for flow modeling in fluvial reservoirs. Near the wells, these intraclast conglomerate and mudstone beds can be followed with a high level of certainty. However, away from the wells the interpretation is carried out with some degree of uncertainty. With improved depth migration and modeling of clay layers within the stratigraphic section in conjunction with a more complete petrographic and diagenetic data base, mapping of even thin layers of mudstone flow barriers will be possible throughout the GPR volume.

GPR Interpretation of Trough Cross Beds

Small to medium scale trough cross beds are also mapped successfully in the 200MHz GPR dataset in the lower parts of unit 5 above surface E (see Figs. 7 and 32 for reference). In Figures 46A, B and C upward-concave discontinuous reflectors truncate against adjacent or overlying reflectors, thus mimicing the geometries seen in the nested trough cross beds in the facies map perpendicular to flow in Figure 32. Reflectors of thinner trough cross beds probably outline cosets of several cross beds rather than individual troughs. Horizontal slices

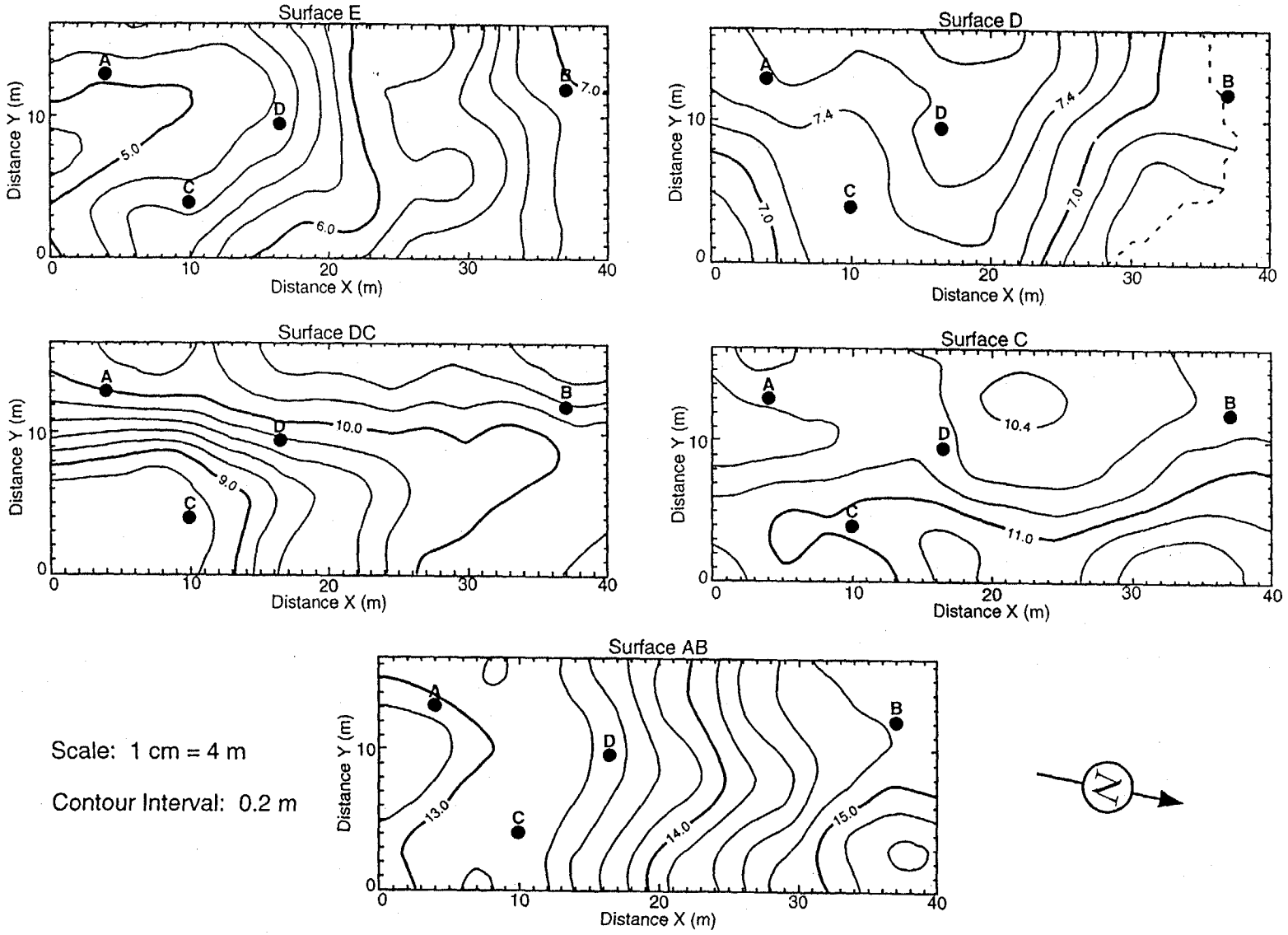

Figure 44: Contour maps for all five surfaces surrounding the major architectural elements in the fluvial sandstone at Coyote Basin. These contour maps are generated from the 3-D GPR data sets on the GeoQuest workstation.

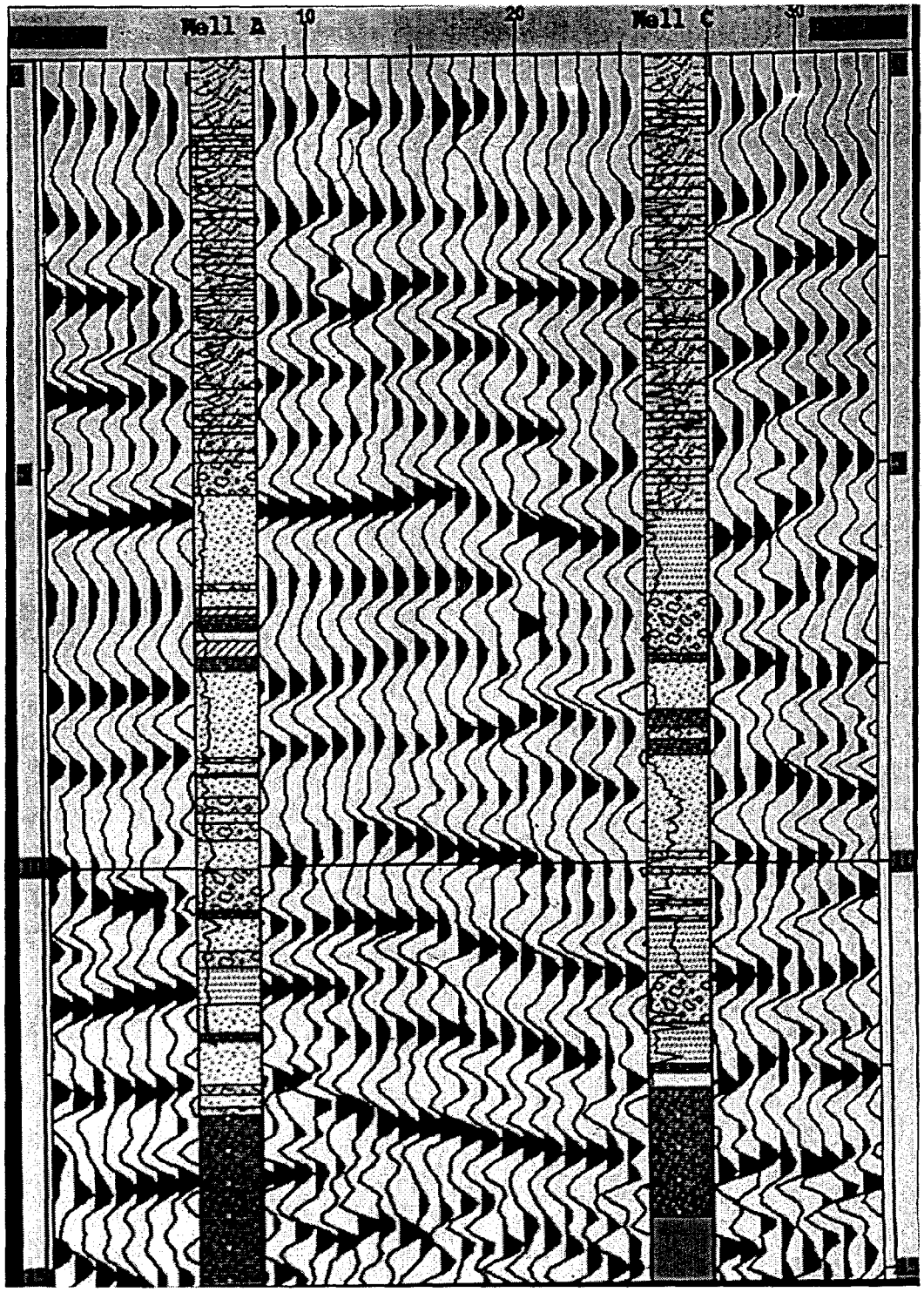

Figure 45A: Uninterpreted GPR profile through Wells A and C from the 100 MHz 3-D dataset. The lithologic columns and permeability curves are shown for correlation with GPR reflectors. The distance between the wells is 0.8 m and the depth of the GPR profile is from 0 to 15 m.

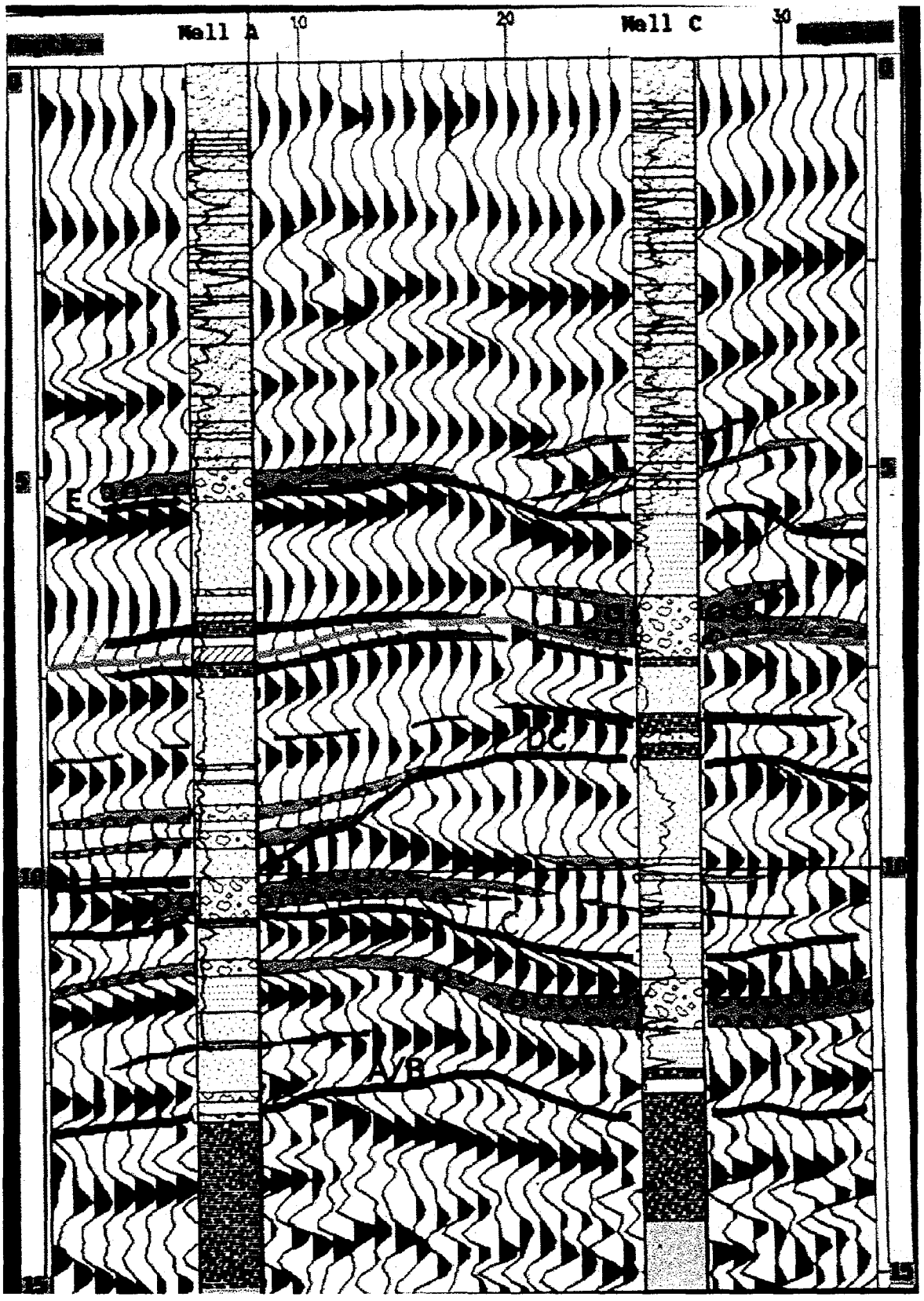

Figure 45B: Interpreted GPR profile through Wells A and C from the 100 MHz 3-D dataset illustrated in Figure 45A. This profile exemplifies how distribution of lithofacies, and therefore flow barriers, may be mapped in 3-D within the GPR volume.

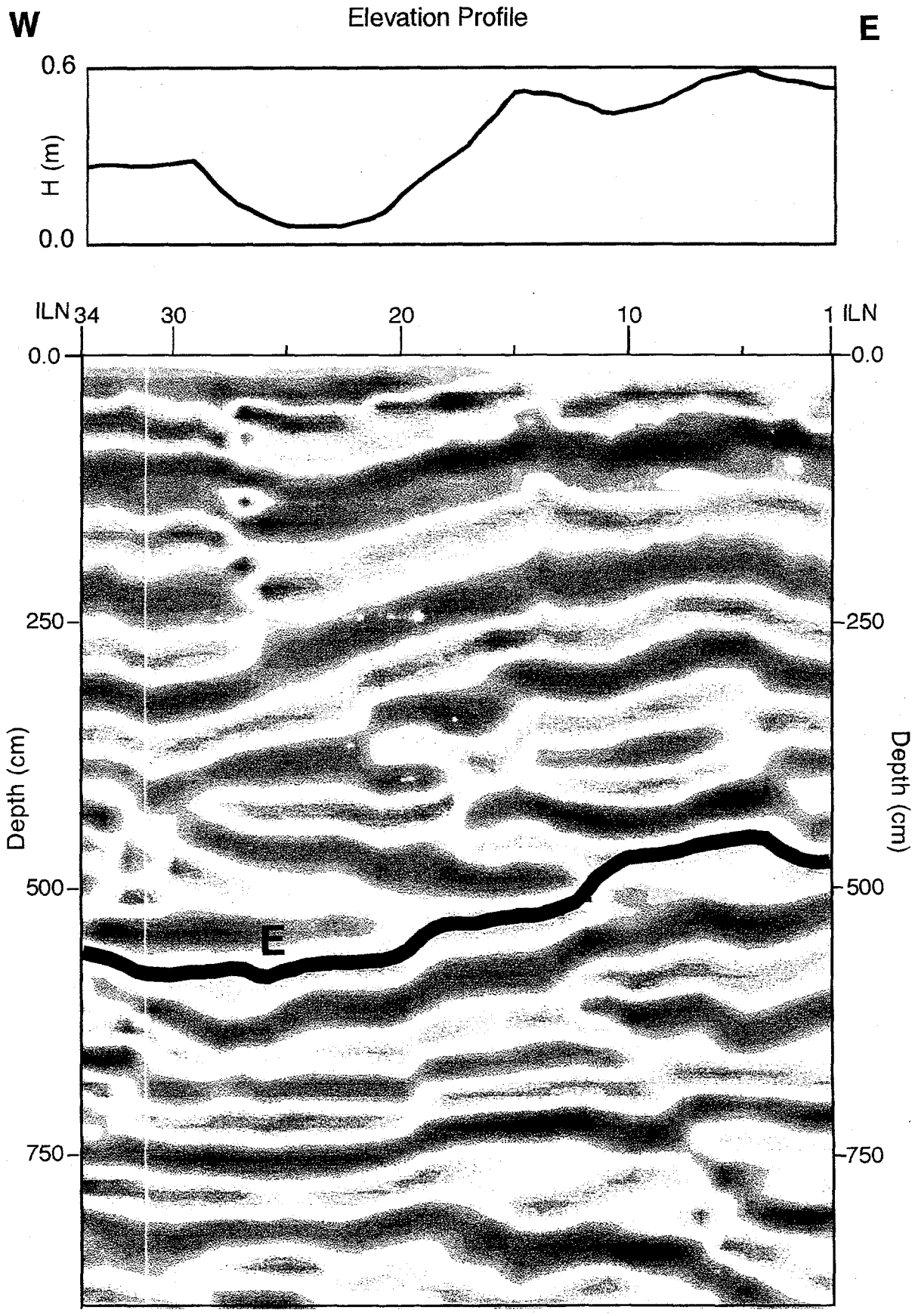

Figure 46A: Uninterpreted GPR crossline number 64 from the upper 8m of the 200 MHz dataset. Surface E at the base of the trough cross-bedded sandstone in unit 5 is shown. Above surface E reflectors are discontinuous and upward concave. In the upper 2.5m of the profile GPR reflectors mimic topography, and is a weathering effect. Width of the profile is 17m and the vertical exaggeration is 2.5X.

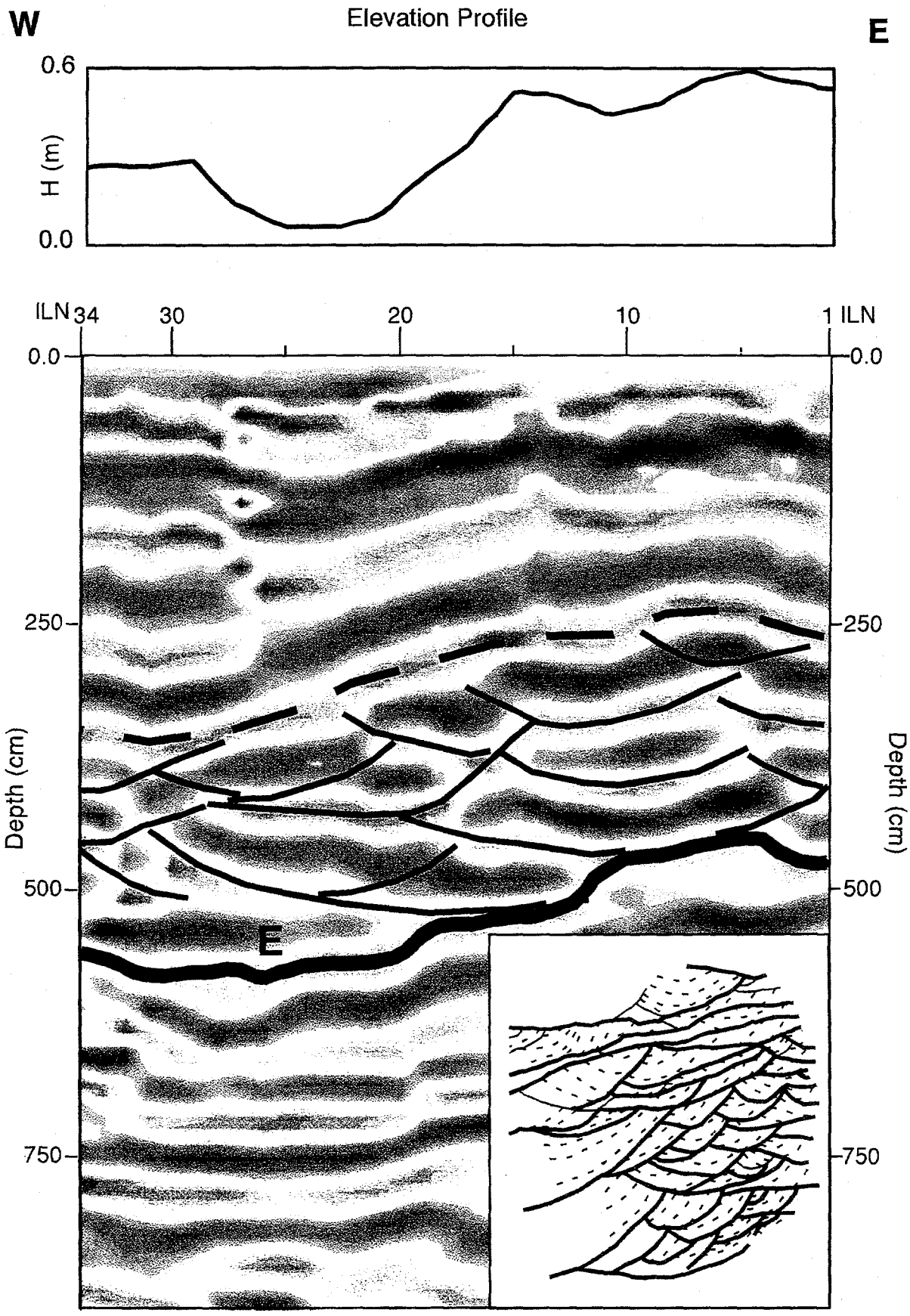

Figure 46B: Interpreted GPR crossline number 64 illustrated in Figure 46A. Cross bed sets and cosets are clearly seen on the GPR profile. Inset of cliff face map of trough cross beds perpendicular to flow in Figure 32 from lower part of unit 5 is shown for comparison. Scale of cross bed map and GPR profile are identical with 2.5X vertical exaggeration. The upper 2.5m of the profile GPR reflectors mimic topography, and is a weathering effect.

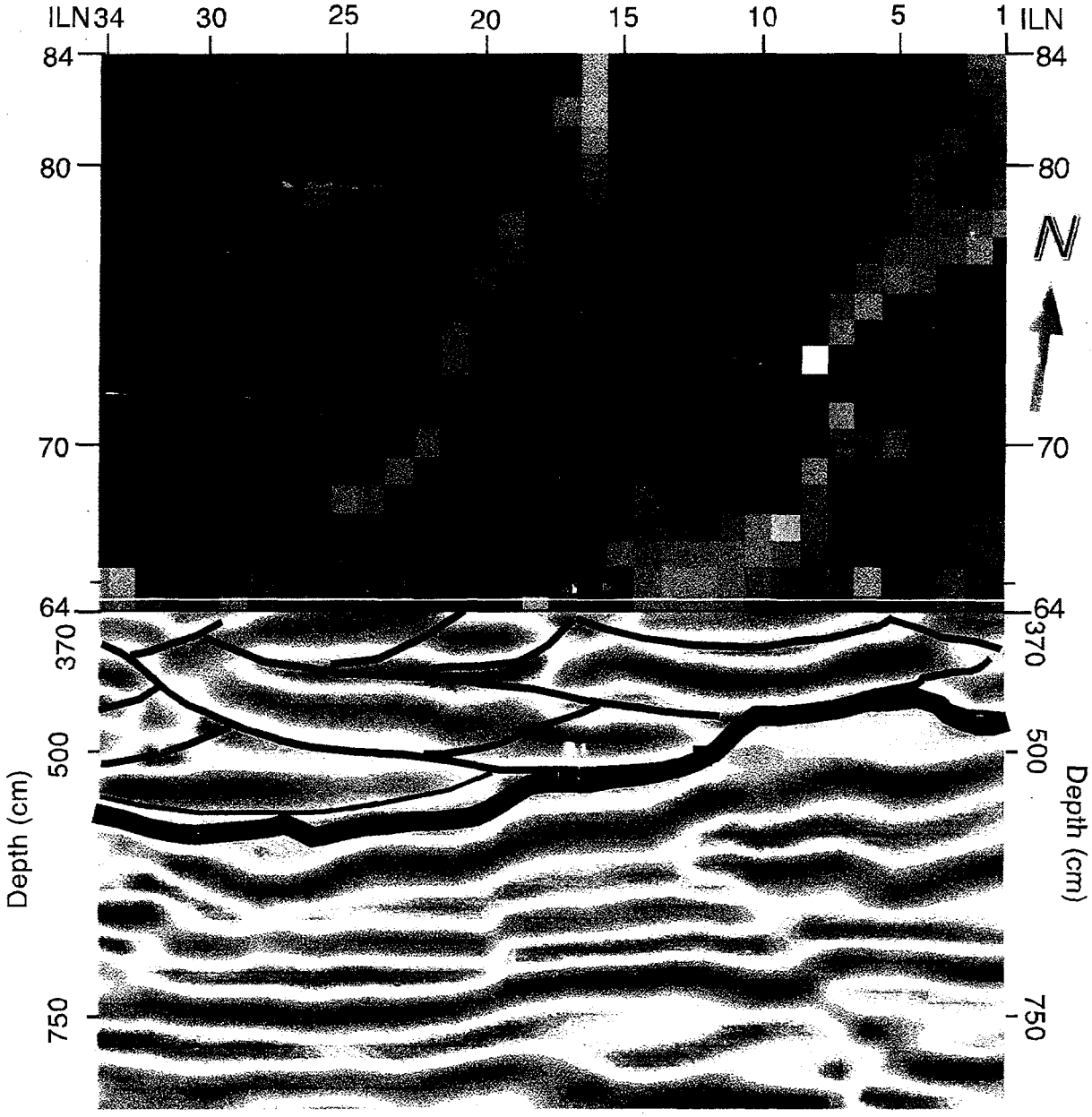

Figure 46C: Horizontal slice and GPR profile through crossline 64 of 200 MHz dataset in which geometry of trough cross beds is illustrated in the third dimension. Elongation of troughs is in the north-south direction and is consistent with the surface map in Figure 6.

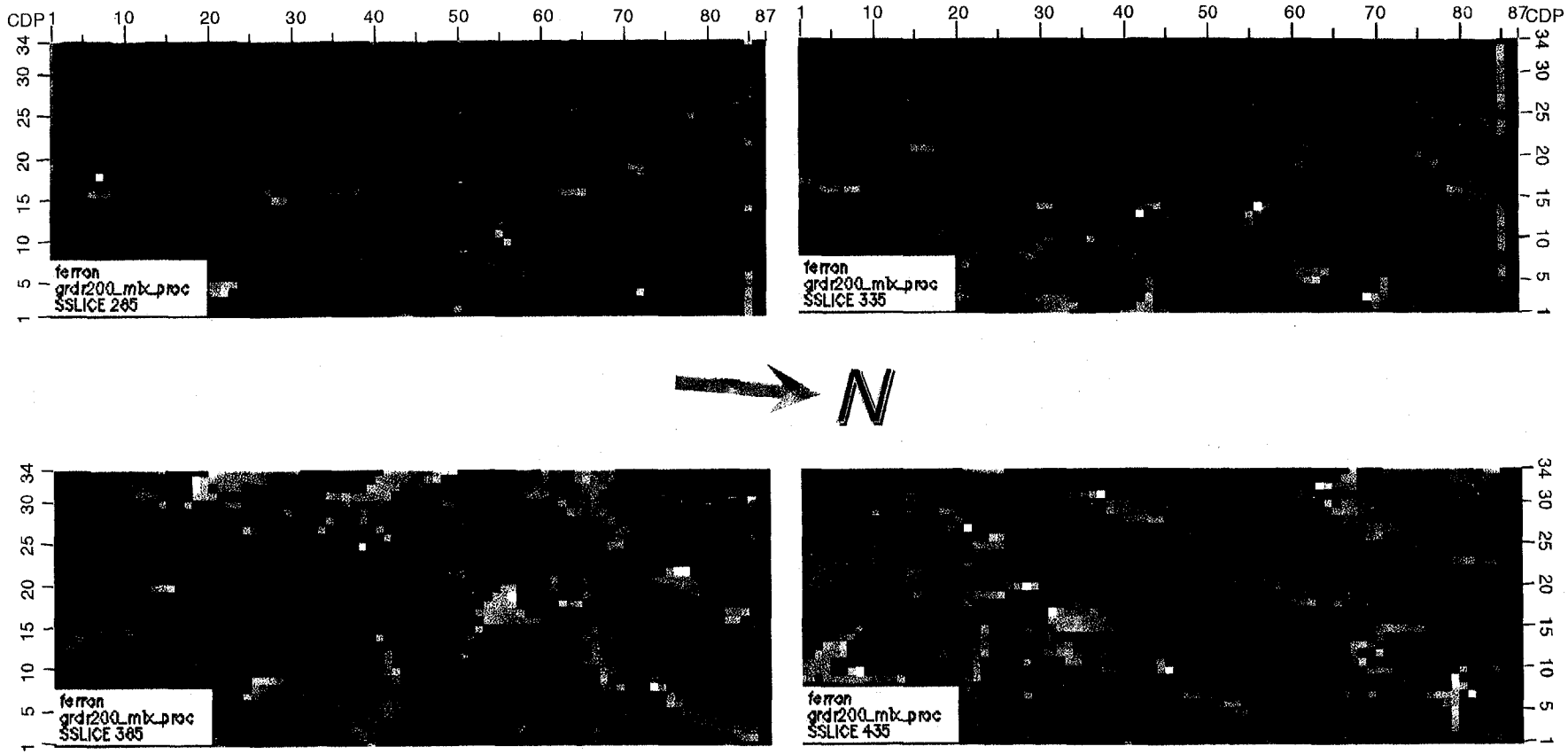

Figure 47: Successive horizontal slices through the 200 MHz data cube at depths of 2.85m, 3.35m, 3.85m and 4.35m within the trough cross-bedded sandstone unit 5. Note trend of elongation direction of GPR reflectors is approximately north-south, parallel to southerly flow seen in geology map in Figure 6.

through the 200 MHz data cube in Figures 46C and 47 reveal a distinct north-south trend in the GPR reflectors, parallel to the flow direction of the trough cross beds in the surface geology map in Figure 7. These GPR surface maps and profiles of trough cross beds from unit 5 are another example of the high resolution obtained from the 200 MHz dataset.

SUMMARY AND CONCLUSION

Ground-penetrating radar data have been used in concert with sedimentologic and stratigraphic data to characterize the three-dimensional architecture of near-surface fluvial reservoir analogs in the SC3 unit of the mid-Cretaceous Ferron Sandstone at Coyote Basin along the southwestern flank of the San Rafael uplift. In order to successfully merge GPR data with the geological information *all* GPR data required processing, including depth migration. Various techniques were used in obtaining a suitable velocity model for the depth migration. These techniques included downhole GPR from which depth-time pairs were recorded, crosshole tomography, and lab measurements from subsurface samples from which electrical and petrographical data were obtained.

All interpretation of GPR data were performed on a GeoQuest workstation at ARCO Oil and Gas Company. Geological outcrop and well data were used as constraints in the interpretation. All higher-order bounding surfaces seen at the outcrop were readily mapped throughout the 3-D GPR volume on the 100 MHz dataset and may now be input directly as an empirical dataset into a 3-D flow simulation model. Thus, the 3-D aspect of architectural elements are clearly described within the GPR volume. Low-permeability barriers such as mudstone and mudstone intraclast conglomerate layers are tentatively mapped between several wells within the survey volume.

We believe that GPR has the potential for describing depositional environments and characterizing near-surface reservoir analogs in the same way that seismic data has been used for analyzing stratigraphic architecture in sequence stratigraphy. Finally, it is concluded that the use of 3-D GPR datasets provide a far more robust means of both processing and interpreting the GPR data.

REFERENCES CITED

Alexander, J., Bridge, J.S., Leeder, M.R., Collier, R.E.L. and Gawthorpe, R.L., 1994, Holocene meander-belt evolution in an active extensional basin, southwestern Montana: Journal of Sedimentary Research, v. B64, p. 542-559.

Baker, P.L., 1991, Fluid, lithology, geometry, and permeability information from ground-penetrating radar for some petroleum industry applications: Societo of Petroleum Engineers, paper SPE 22976, p. 277-286.

Barton, M.D., 1994, Outcrop characterization of architecture and permeability structure in fluvial-deltaic sandstones, Cretaceous Ferron sandstone, Utah [Dissertation]: City, University of Texas at Austin, Austin Texas, 260 p.

Beres, M., Green, A., Huggenberger, P. and Horstmeyer, H., 1995, Mapping the architecture of glaciofluvial sediments with three-dimensional georadar: Geology, v. 23, p. 1087-1090.

Bridge, J.S., 1986, Paleochannel pattern inferred from alluvial deposits; a critical review: Journal of Sedimentary Petrology, v. 55, p. 579-589.

Bridge, J.S. and Leeder, M.R., 1979, A simulation model of alluvial stratigraphy: Sedimentology, v. 26, p. 617-644.

Bridge, J.S., Alexander, J., Collier, R.E.Ll., Gawthorpe, R.L. and Jarvis, J., 1995, Ground-penetrating radar and coring used to study the large-scale structure of point-bar deposits in three dimensions: Sedimentology, v. 42, p. 839-852.

Bristow, C.S., 1995, Internal geometry of ancient tidal bedforms revealed using ground penetrating radar, *in* Flemming, B.W. and Bartholoma, A., (eds.), Tidal Signatures in Modern and Ancient Sediments: International Association of Sedimentologists, Spectal Publication No. 24, p. 313-328.

Carman, P.C., 1937, Fluid flow through a granular bed: Transactions of the Institute for Chemical Engineering of London, v. 15, p. 150-156.

Chidsey, T. C., Jr., 1997, Geological and petrophysical characterization of the Ferron Sandstone for 3-D simulation of a fluvial deltaic reservoir - Annual report for the period of October 1, 1995 to September 30, 1996: U.S. Department of Energy Report DOE/BC/14896-15, 57 p.

Damsleth, E., and L. Holden, 1994, Mixed reservoir characterization methods: Society of Petroleum Engineers, paper SPE 24742, p. 29-31.

Fielding, C.R., and R.C. Crane, 1987, Application of statistical modeling to the prediction of hydrocarbon recovery factors in fluvial reservoir sequences, *in* F.G. Ethridge, R.M. Flores and M.D. Harvey (eds.), Application of Statistical Modeling to the Prediction of Hydrocarbon Recovery Factors in Fluvial Reservoir Sequences: Society of Economic Paleontologists and Mineralogists, Special Publication No. 39, p. 321-327.

Fisher, E., G.A. McMechan, and A.P. Annan, 1992a, Acquisition and processing of wide-aperture ground-penetrating radar data: Geophysics, v. 57, p. 495-504.

Fisher, E., G.A. McMechan, and A.P. Annan, 1992b, Examples of reverse-time migration of single-channel ground penetrating radar profiles: Geophysics, v. 57, p. 577-586.

Flint, S.S. and Bryant, D. (eds.), 1993, The Geological Modelling of Hydrocarbon Reservoirs and Outcrop Analogues: International Association of Sedimentologists, Special Publication Number 15: Boston, Blackwell, Scientific Publication, 269 p.

Gardner, M.H., 1995, Tectonic and eustatic controls on the stratal architecture of mid-Cretaceous stratigraphic sequences, central western interior foreland basin of North America, *in* S.L. Dorobek and G.M. Ross, eds., Stratigraphic Evolution of Foreland Basins: Tulsa, Oklahoma, Society of Economic Paleontologists and Mineralogists Special Publication No. 52, p. 243-281.

Garrison, J.R., Jr., Van den Bergh, T.C.V., Barker, C.E.F., and Tabet, D.E., 1997, Depositional sequence stratigraphy and architecture of the Cretaceous Ferron Sandstone: Implications for coal and coalbed methane resources - A field excursion, *in* P.K. Link and B.J. Kowallis (eds.), Depositional sequence stratigraphy and architecture of the Cretaceous Ferron Sandstone: Implications for coal and coalbed methane resources - A field excursion: Geological Society of America Field Trip Guidebook for 1997 Annual Meeting, Part 2, p. 155-202.

Gawthorpe, R.L., Collier, R.E.L., Alexander, J., Bridge, J.S., Leeder, M.R., 1993, Ground penetrating radar: application to sandbody geometry and heterogeneity studies, *in* C.P. North and D.J. Prosser (eds.), Ground penetrating radar: application to sandbody geometry and heterogeneity studies: Geological Society Special Publication No. 73, p. 421-432.

Henriquez, A., Tyler, K.J. and Hurst, A., 1990, Characterization of fluvial sedimentology for reservoir simulation modeling: Society of Petroleum Engineers Formation Evaluation, p. 211-216.

Klein, K. and Santamarina, J.C., 1997, Methods for broad-band dielectric permittivity measurements(soil-water mixtures, 5 Hz to 1.3 GHz), Geotechnical Testing Journal (GTJODJ), v. 20, p. 168-178.

Knoll, M.D. and Knight, R., 1994, Relationships between dielectric and hydrologic properties of sand-clay mixtures: Proc., Fifth International Conference on GPR, 12-16 June 1994, Kitchener, Ontario, p. 45-61.

Kozeny, J., 1927, Uber kapillare Leitung des Wassers im Boden: Sitzungsber. Akad. Wiss. Wien, v. 136, p. 271-306.

Mackey, S.D. and Bridge, J.S., 1995, Three dimensional model of alluvial stratigraphy: Theory and application: Journal of Sedimentary Research, v. B65, p. 7-31.

Mavko, G. and Nur, A., 1997, The effect of a percolation threshold in the Kozeny-Carman relation: Geophysics, v. 62, p. 1480-1482.

McMechan, G.A., G.C. Gaynor, and R.B. Szerbiak, 1997, Use of ground-penetrating radar for 3-D sedimentological characterization of clastic reservoir analogs: Geophysics, v. 62, p. 786-796.

Miall, A.D. and Turner-Peterson, C.E., 1989, Variations in fluvial style in the Westwater Canyon Member, Morrison Formation (Jurassic), San Juan Basin, Colorado Plateau: Sedimentary Geology, v. 63, p. 21-60.

Ryer, T.A., 1981, Deltaic coals of the Ferron Sandstone Member of the Mancos Shale: predictive model for Cretaceous coal-bearing strata of the western interior: American Association of Petroleum Geologist Bulletin, v. 65, p. 2323-2340.

Santamarina, J.C. and Fam, M., 1997, Dielectric permittivity of soils mixed with organic and inorganic fluids (0.02 GHz to 1.30 GHz): Journal of Environmental and Engineering Geophysics (JEEG), v. 2, p. 37-51.

Thurmond, J.B., McMechan, G., Soegaard, K., Szerbiak, R., Gaynor, G.C., Forster, C.B. and Snelgrove, S.H., 1997, Integration of 3-D ground-penetrating radar, outcrop, and

borehole data applied to reservoir characterization and flow simulation: Abstracts with Programs, American Association of Petroleum Geologists, p. A116.

van den Bergh, T.C.V. and Garrison, J.R., 1996, Channel belt architecture and geometry - a function of depositional parasequence set stacking pattern, Ferron Sandstone, East-central Utah: American Association of Petroleum Geologists, Rocky Mountain Section Meeting, Abstracts with Programs.

Xu, T. and McMechan, G.A., 1997, GPR attenuation and its numerical simulation in 2.5-D: Geophysics, v. 62, p. 403-414.

TECHNOLOGY TRANSFER

There are several arenas in which results from the project have presented or are planned to presented in the near future. These include the national convention for the American Association of Petroleum Geologists in Dallas, Texas (Thurmond et al., 1997) and in Salt Lake City, Utah (Snelgrove et al., 1998).

At present one research article has been published by McMechan et al. (1997). Several additional articles are nearing completion and include Corbeanu et al. (1998), Wang et al. (1998) and Szerbiak et al. (1998 a, b). At least one additional paper describing the lab measurements and preliminary flow modeling done at the University of Utah is also in preparation.

From the inception of the integrated GPR and sedimentology-stratigraphy resevoir characterization studies in the Cretaceous Ferron Sandstone in east-central Utah there has been a close working relationship between The University of Texas at Dallas and petroleum companies. Seed money was initially provided by ARCO and Chevron for several feasibility studies. Subsequently, a broader-based consortium of energy companies was assembled to enhance the applicability of results to the reservoir characterization project at Coyote Basin. This consortium included ARCO, Mobil, Union Pacific and Unocal and was managed in collaboration with Dr. Craig Forester and his collegues at The University of Utah. Several presentations have given to consortium members and a Final Report was presented to members of the consortium in January 1998 (Forster et al., 1998).

Finally, a Web site is maintained and updated at The University of Utah in which the most recent results of the reservoir charaterization project are posted. The Web address for the University of Utah web site is www6.egi.utah.edu

The collaboration between the groups at The University of Texas at Dallas and The University of Utah has recently been expanded via a three year continuation project entitled "Integrated 3-D ground-penetrating radar, outcrop, and borehole data applied to reservoir characterization and flow simulation." This project is funded by the Department of Energy and started in March, 1998. Its objectives include application to a different environment (dominated by lateral accretion sets), collecting a much larger 3-D GPR grid, and inclusion of flow modeling.

References of Technology Transfer

Abstracts:

Snelgrove, S.H., McMechan, G.M., Szerbiak, R., Wang, D., Corbeanu, R., Soegaard, K., Thurmond, J.B., Forster, C.B., Crossey, L. and Roche, K., 1998, Integrated 3-D characterization and flow simulation studies of a fluvial channel, Ferron Sandstone, east-central Utah: Abstracts with Programs, American Association of Petroleum Geologists.

Thurmond, J.B., McMechan, G., Soegaard, K., Szerbiak, R., Gaynor, G.C., Forster, C.B. and Snelgrove, S.H., 1997, Integration of 3-D ground-penetrating radar, outcrop, and borehole data applied to reservoir characterization and flow simulation: Abstracts with Programs, American Association of Petroleum Geologists, p. A116.

Papers:

McMechan, G.A., G.C. Gaynor, and R.B. Szerbiak, 1997, Use of ground-penetrating radar for 3-D sedimentological characterization of clastic reservoir analogs: Geophysics, v. 62, p. 786-796.

Consortium Reports:

Foster, C.B., Snelgrove, S.M., McMechan,G., Soegaard, K., Corbeanu, R., Szerbiak, R., Thurmond, J., Crossey, L., and Roche, K., 1998, Final Report, The Coyote Basin Project: Integrating Shallow 3-D GPR and Petrophysical Data for Fluvial-Deltaic Reservoir Facies with Implications for Infill Drilling and Reservoir Modeling, EGI, University of Utah.

Manuscripts in Preparation:

Corbeanu, R., Soegaard, K., Thurmond, J., McMechan G.M., Szerbiak, R. and Wang, D., 1998, Mapping 3-D distribution of bounding surfaces at various scales within fluvial sandstone complex in the mid-Cretaceous Ferron Sandstone in east-central Utah using integrated GPR and outcrop data: Journal of Sedimentary Research, in preparation.

Szerbiak, R.B., Corbeanu, R., Thurmond, J., Soegaard, K., McMechan, G.A., 1998a, Acquisition and processing of 3-D GPR data in the Ferron Sandstone of Central Utah, in preparation.

Szerbiak, R.B., Crossey, L., Roche, K., Forster, C., Snelgrove, S., McMechan, G.A., 1998b, Correlations between petrographic, petrophysical, and electrical properties of samples from the Ferron Sandstone of Central Utah, in preparation.

Wang, D.M., Szerbiak, R.B., Corbeanu, R., and McMechan, G.A., 1998, Numerical simulation of borehole GPR data with application to fluvial structures in Ferron Sandstone of Central Utah, in preparation.

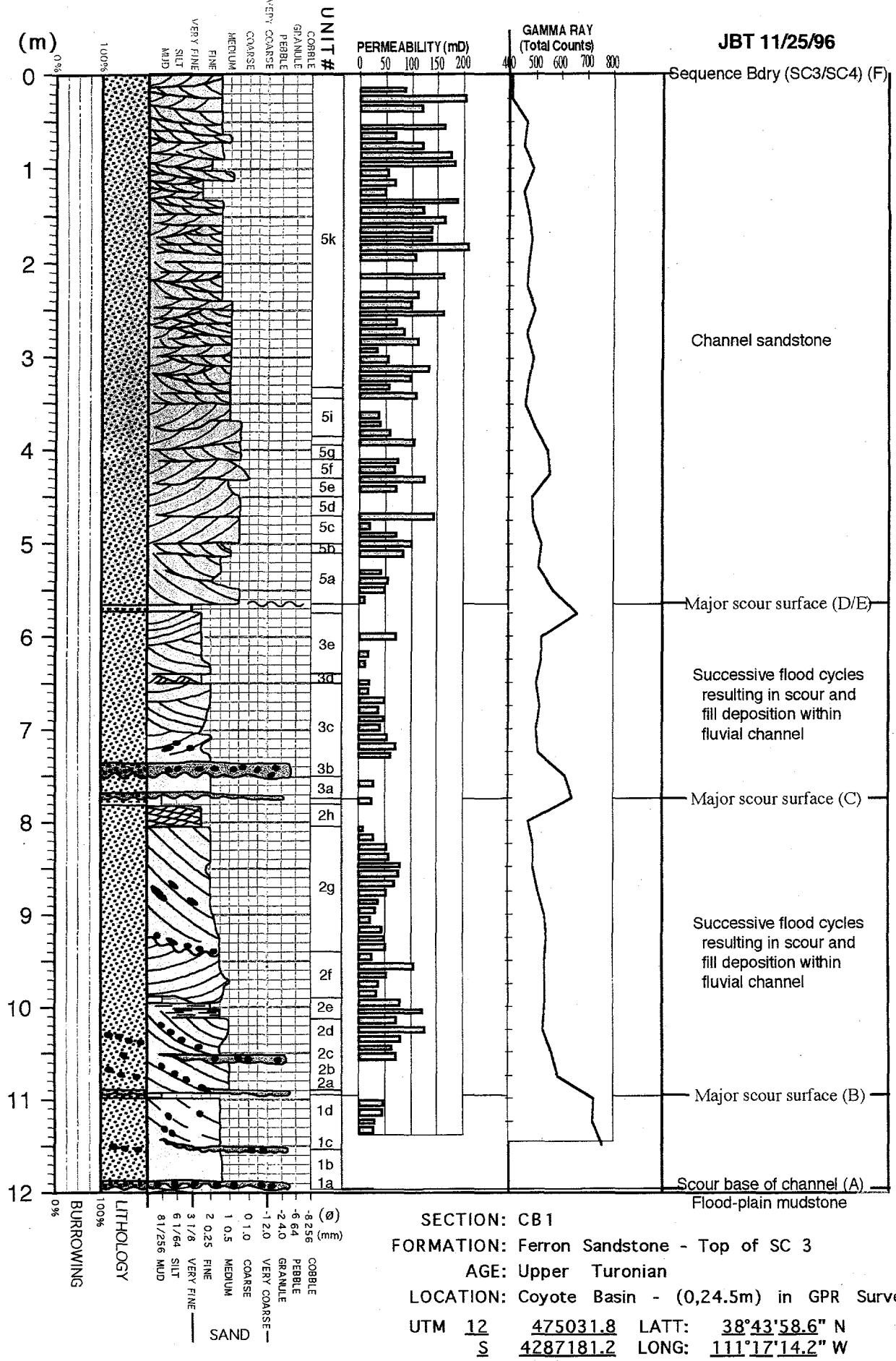

SECTION: CB1
FORMATION: Ferron Sandstone - Top of SC 3
AGE: Upper Turonian
LOCATION: Coyote Basin - (0,24.5m) in GPR Survey
UTM 12 S 475031.8 4287181.2 LATT: 38°43'58.6" N LONG: 111°17'14.2" W

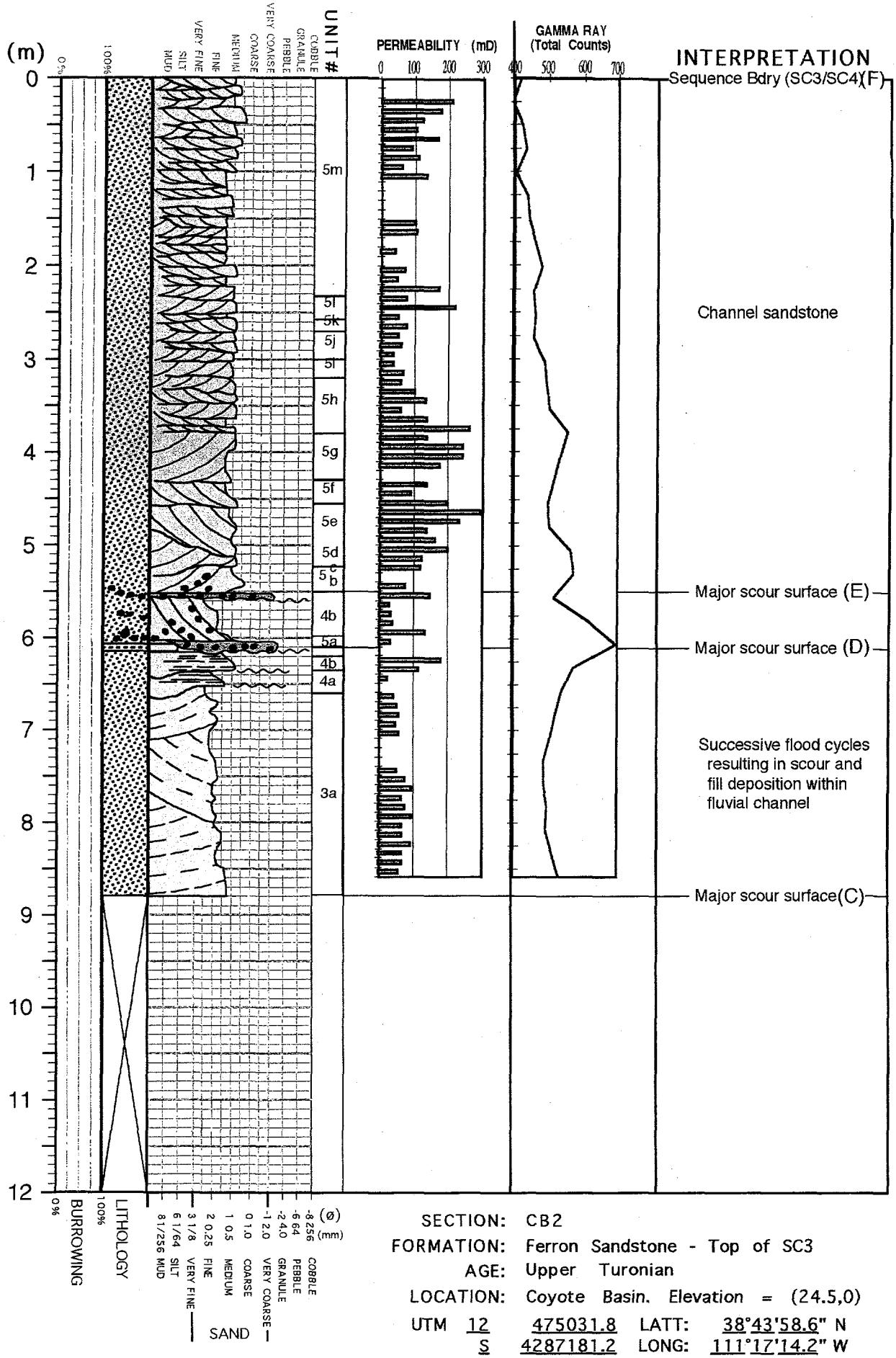
(m)
UNIT #
PERMEABILITY (mD)
GAMMA RAY (Total Counts)
INTERPRETATION
Sequence Bdry (SC3/SC4)(F)
Channel sandstone
Major scour surface (E)
Major scour surface (D)
Successive flood cycles resulting in scour and fill deposition within fluvial channel
Major scour surface(C)
BURROWING
LITHOLOGY
SAND
SECTION: CB2
FORMATION: Ferron Sandstone - Top of SC3
AGE: Upper Turonian
LOCATION: Coyote Basin. Elevation = (24.5,0)
UTM 12 475031.8 LATT: 38°43'58.6" N
S 4287181.2 LONG: 111°17'14.2" W

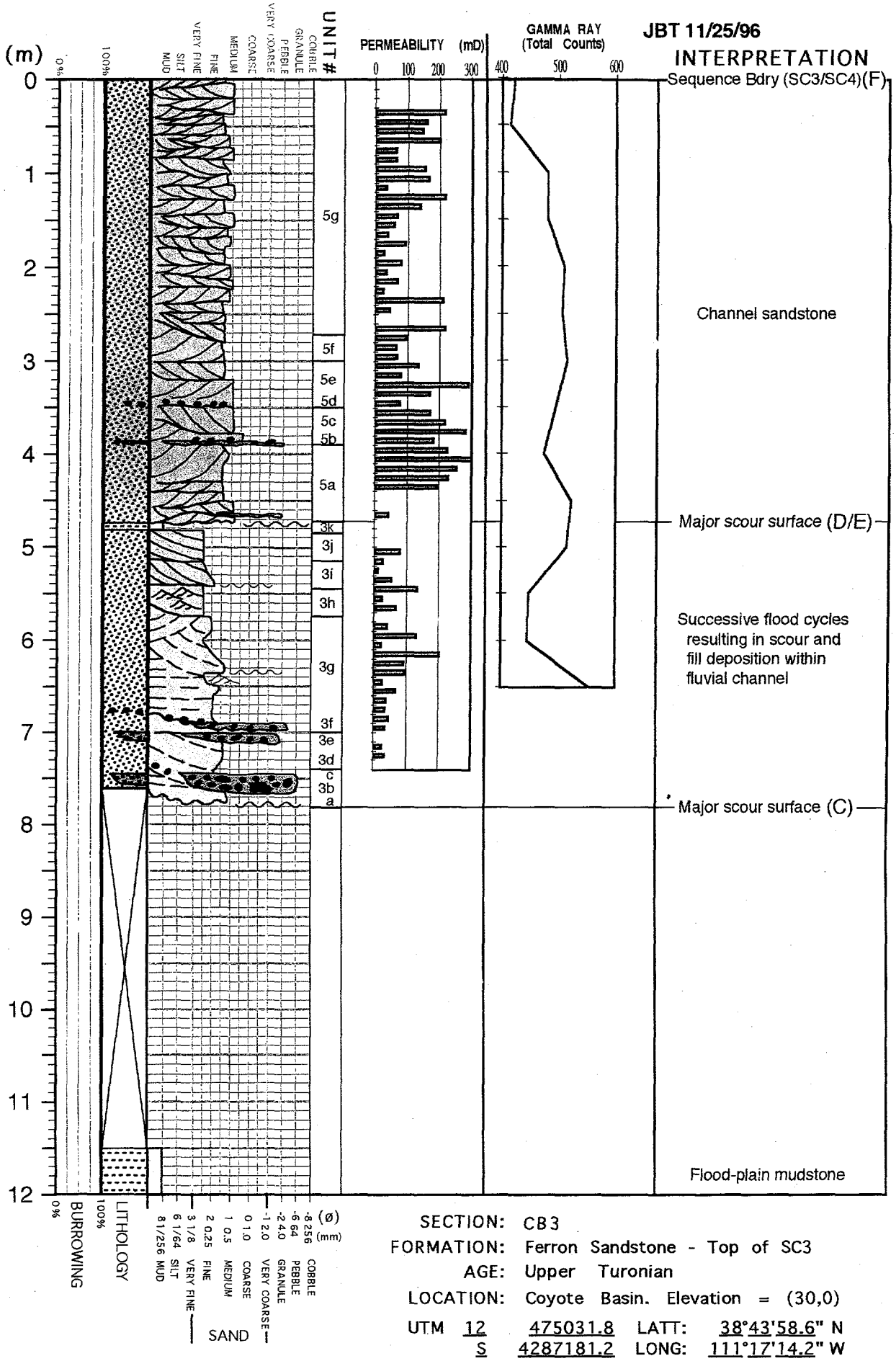

SECTION: CB3
FORMATION: Ferron Sandstone - Top of SC3
AGE: Upper Turonian
LOCATION: Coyote Basin. Elevation = (30,0)
UTM 12 475031.8 LATT: 38°43'58.6" N
S 4287181.2 LONG: 111°17'14.2" W

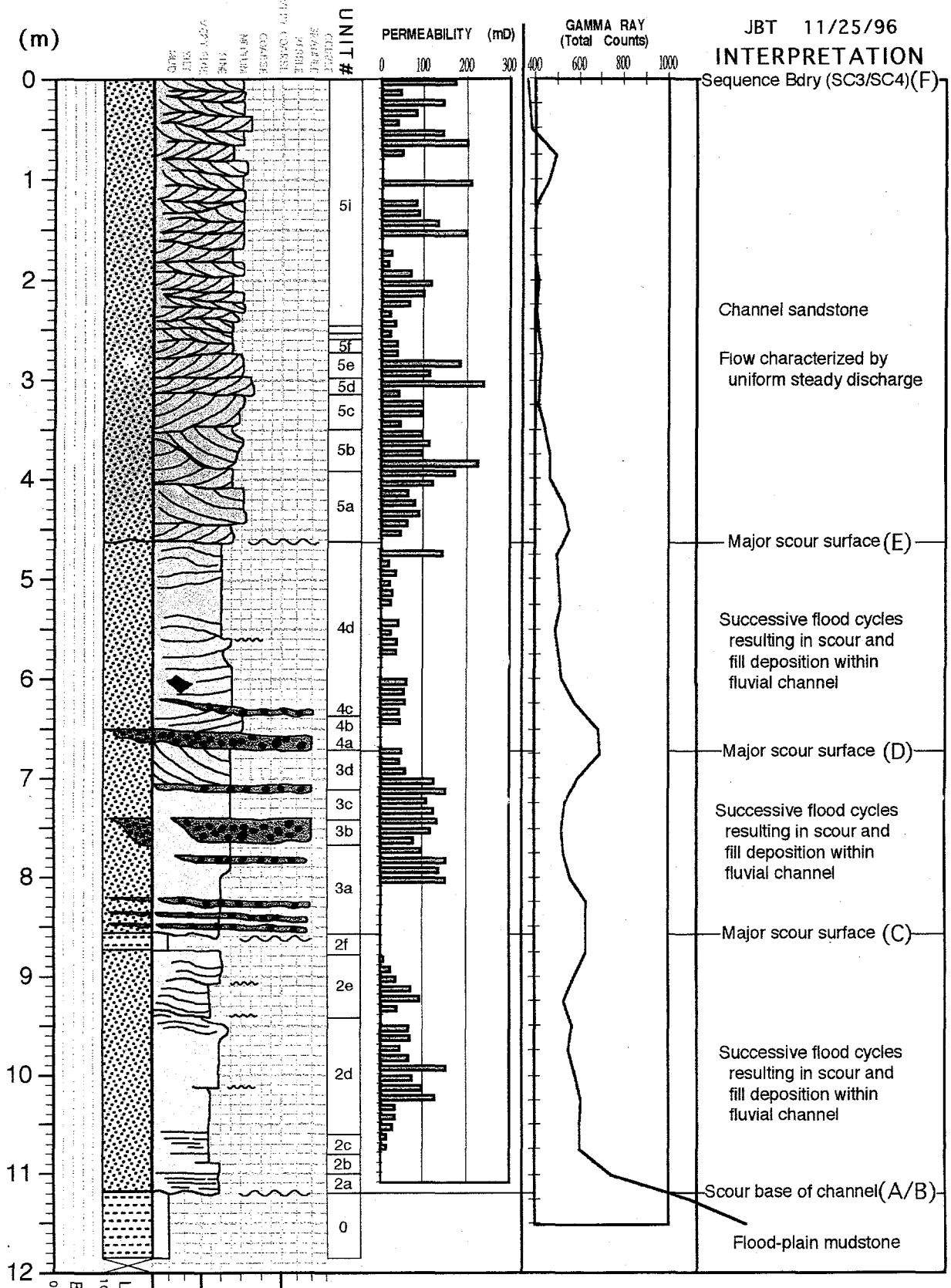

SECTION: CB4
FORMATION: Ferron Sandstone - Top of SC3
AGE: Upper Turonian
LOCATION: Coyote Basin. Elevation = (20,0)
UTM 12 S 475031.8 4287181.2 LATT: 38°43'58.6" N LONG: 111°17'14.2" W

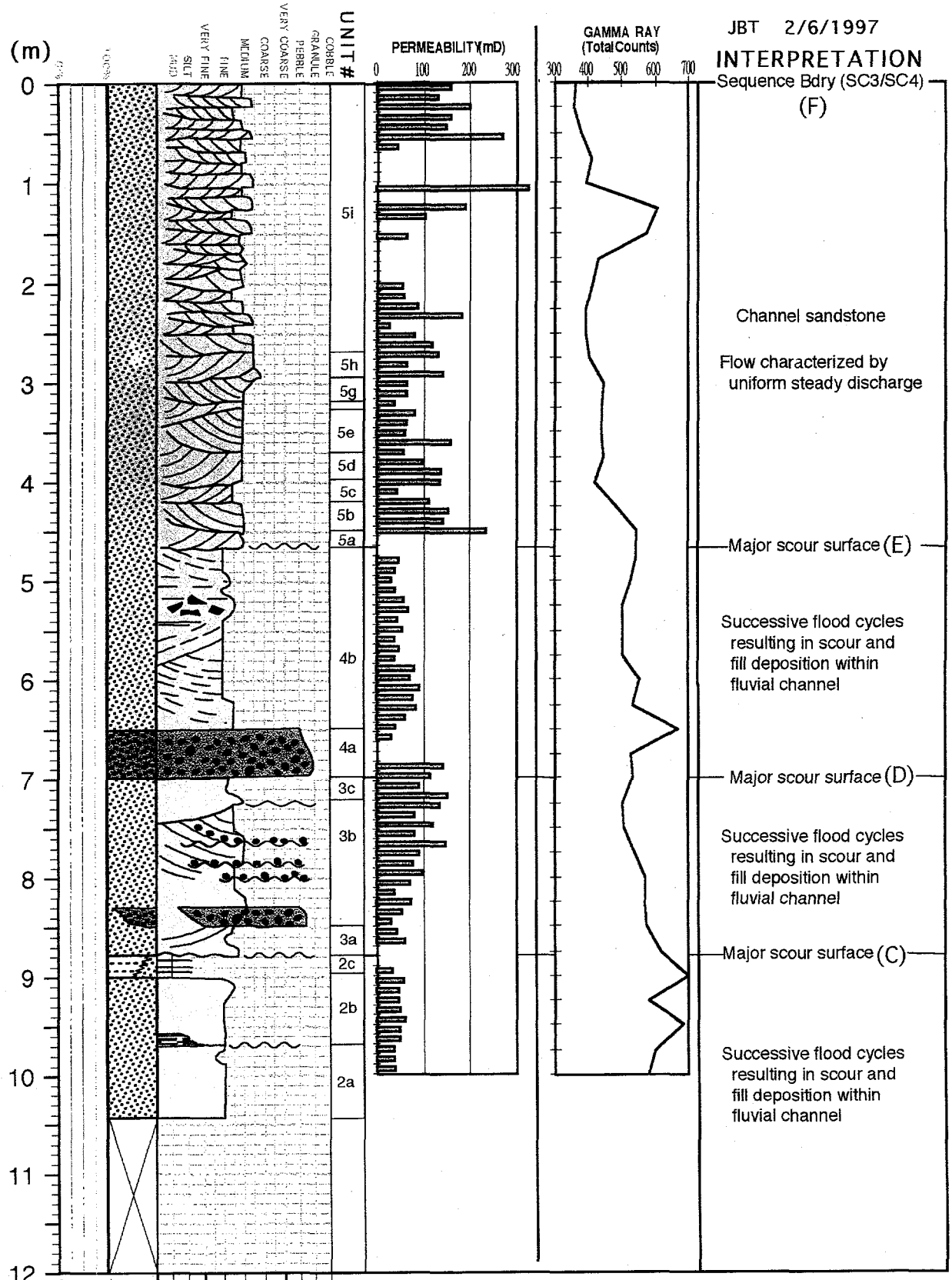

SECTION: CB5
FORMATION: Ferron Sandstone - Top of SC3
AGE: Upper Turonian
LOCATION: Coyote Basin. Elevation = (10,-9.6)
UTM 12 S 475031.8 4287181.2 LATT: 38°43'58.6" N LONG: 111°17'14.2" W

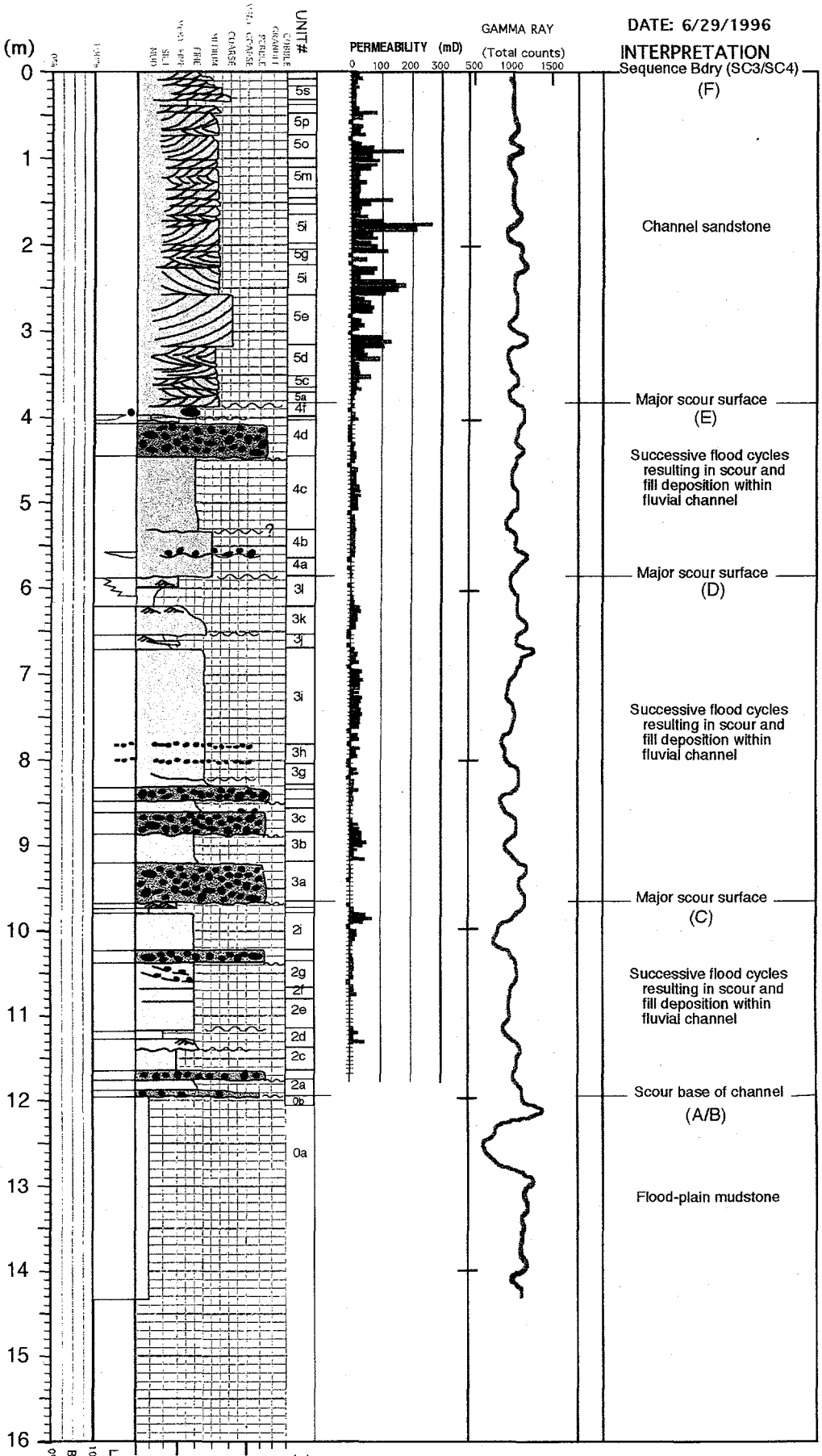

SECTION: Well A
FORMATION: Ferron Sandstone - Top of SC3
AGE: Upper Turonian
LOCATION: Coyote Basin - GPR Grid Point (4, 13)

UTM 12 S 475031.8 4287181.2 LATT: 38°43'58.6" N LONG: 111°17'14.2" W

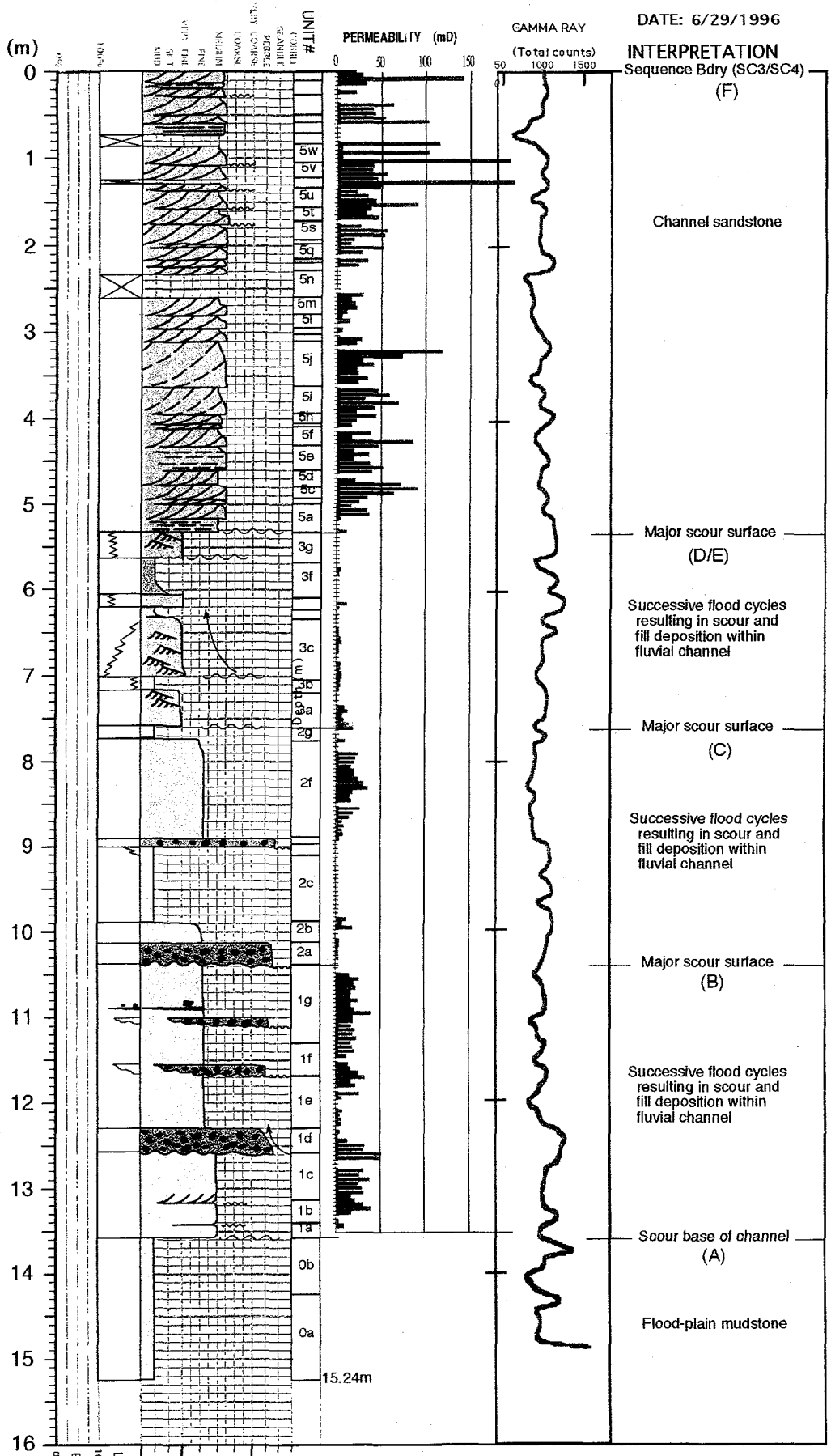

SECTION: Well B
FORMATION: Ferron Sandstone - Top of SC3
AGE: Upper Turonian
LOCATION: Coyote Basin - GPR Grid Point (37, 12)
UTM 12 475031.8 LATT: 38°43'58.6" N
S 4287181.2 LONG: 111°17'14.2" W

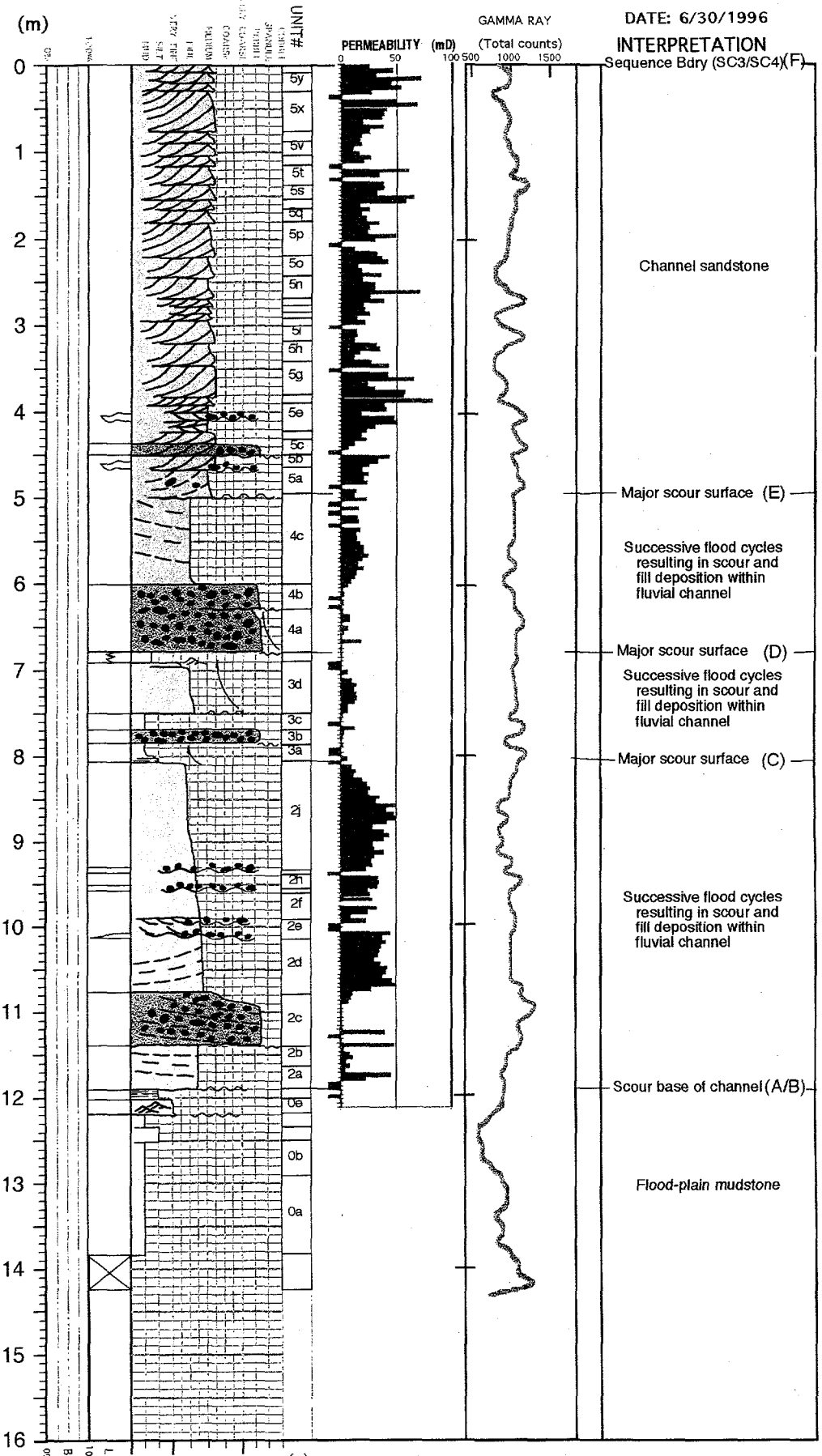

SECTION: Well C
FORMATION: Ferron Sandstone - Top of SC3
AGE: Upper Turonian
LOCATION: Coyote Basin - GPR Grid Point (10, 4)
UTM 12 475031.8 LATT: 38°43'58.6" N
S 4287181.2 LONG: 111°17'14.2" W